

**Electrochemical deposition of Cobalt, Nickel-Cobalt, Nickel-Copper and
Zinc-Nickel nanostructured materials on aluminum by template self-
organization**

Dissertation

zur Erlangung des akademischen Grades
doctor rerum naturalium (Dr. rer. nat.)

vorgelegt der

Naturwissenschaftlichen Fakultät II - Chemie und Physik
der Martin-Luther-Universität Halle-Wittenberg

von Herrn **M. sc. Adolphe FOYET**

geb. am 11. 02. 1977 in Fotouni /Cameroon

Gutachter:

1. Prof. Dr. Wieland Schäfer
2. Prof. Dr. Michael Köhler

Halle (Saale), 24. 09. 2007

urn:nbn:de:gbv:3-000012352

[<http://nbn-resolving.de/urn/resolver.pl?urn=nbn%3Ade%3Agbv%3A3-000012352>]

This thesis is dedicated to my parents
TENKEU Michel and NGAPGOUE Anne

Contents.....	I
1. Introduction.....	1
2. Preparation and characterization of nanoparticles and nanofilms.....	4
2.1. Porous aluminum oxide as template for nanomaterial.....	4
2.2. Surfactant and liquid crystal templates.....	5
2.3. Characterization of mesoporous films.....	8
2.3.1. Scanning Probe techniques.....	8
2.3.2. Electrochemical impedance spectroscopy.....	10
2.3.2.1. Data presentation.....	11
2.3.2.2. Impedance data analysis.....	14
3. Experimental part.....	17
3.1. Reagents.....	17
3.2. Preparation of templates.....	17
3.3. Electrochemical deposition and characterization.....	18
3.3.1. Electrodeposition.....	18
3.3.2. Characterization.....	20
- Atomic force Microscopy and scanning tunneling microscopy.....	20
- Electrochemical impedance spectroscopy.....	20
- Semiconductivity measurements: Mott-schottky plot.....	22
- Electrochemical noise measurement.....	22
- Polarization and corrosion measurements.....	22
4. Template deposition of cobalt nanoparticles.....	23
4.1. Preparation and characterization of porous alumina membrane (AAO).....	23
4.1.1. Preparation of AAO.....	23
4.1.2. Characterization of AAO: AFM and impedance spectroscopy.....	25
4.2. Electrochemical deposition of cobalt from aqueous solution to the pore of AAO.....	31
4.2.1. Influence of the deposition charge on the structure of cobalt nanomaterial.....	31
4.2.2. Influence of the current density on the structure of cobalt nanomaterial.....	36
4.2.3. Electrochemical Impedance characterization of cobalt nanofilm on AAO.....	42
4.2.4. Discussion of the impedance results.....	45
4.2.5. Electrochemical deposition of single nanorod and clusters in the pores of AAO.....	46

4.3 Deposition of cobalt in the AAO membrane using the hexagonal phase of lyotropic liquid crystal: Double template electrodeposition.....	49
4.3.1. Preparation and characterization of liquid crystals mixtures.....	49
4.3.2. Principle of double template deposition.....	51
4.3.3. Double template electrochemical deposition of cobalt.....	52
- Direct current electrochemical deposition.....	52
- Pulse current electrochemical deposition.....	54
4.3.4. Impedance spectra of cobalt film deposited from Brij 76 templating mixture.....	61
4.4. Electrochemical behavior of cobalt nanoparticles in LiClO ₄ aqueous solution.....	64
4.4.1. Anodic linear voltammetry and corrosion measurement.....	64
4.4.2. Electrochemical noise measurement.....	67
4.4.3. Mott-Schottky analysis of cobalt nanofilm in Lithium perchlorate.....	70
4.5. Partial conclusion.....	74
5. Double template deposition and characterization of alloys nanoparticles.....	75
5.1. Preparation and characterization of ZnNi alloy nanoparticles.....	75
5.1.1. Electrochemical deposition.....	75
5.1.2. Polarization behavior of ZnNi alloy nanoparticles.....	78
5.1.3. Electrochemical Impedance measurements.....	80
5.1.4. Corrosion and Mott-Schottky analysis.....	82
5.2. Preparation and characterization of NiCu alloy nanoparticles.....	85
5.2.1. Electrodeposition of NiCu alloy.....	85
5.2.2. Polarization and corrosion of NiCu alloy nanoparticles.....	87
5.2.3. Impedance and Mott-Schottky analysis of NiCu alloy nanoparticles.....	89
5.3. Electrodeposition and characterization of NiCo alloy nanoparticles.....	92
5.3.1. Electrochemical deposition.....	92
5.3.2. Polarization and corrosion measurements.....	94
5.3.3. Impedance and Mott-Schottky analysis of NiCo nanoparticles.....	96
5.4. Discussion.....	98
6. Summary.....	101
7. References.....	104

8. Appendix.....	111
8.1. X-ray diffraction of cobalt nanoparticles.....	111
8.2. Phase diagram of surfactants used in double template deposition.....	112
8.3. Working hypothesis for impedance measurement.....	113
8.4. Fitting of Impedance data and calculation of $Z(j\omega)$ equations.....	114
8.3.1. Impedance of alumina membrane.....	114
8.3.2. Impedance of cobalt film deposited from aqueous solution into AAO.....	117
8.3.3. Impedance of cobalt film deposited from Brij 76 into AAO.....	118
8.3.4. Impedance model of alloys nanoparticles.....	120
8.5. Principle of Atomic force Microscopy (AFM).....	121

Acknowledgements

Conferences and publication

Curriculum Vitae

Abbreviations

AFM	Atomic force microscope
AAO	Anodic aluminum oxide
STM	Scanning tunneling microscope
SEM	Scanning electron microscope
TEM	Transmission electron Microscope
SPM	Scanning probe microscopes
SCE	Saturated calomel electrode
RE	Reference electrode
CE	Counter electrode
WE	Working electrode
Brij 76	Decaethyleneoxide monoctadecyl ether (C ₁₈ EO ₁₀)
Brij 78	Polyoxyethylene(20)stearylether (C ₁₈ EO ₂₀)
CTAB	Hexadecyltrimethyammonium bromide
SAXS	Small angle x-ray scattering
DC	Direct current
AC	Alternative current
RMS	Root mean square roughness
EIS	Electrochemical impedance spectroscopy
ALSV	Anodic linear sweep voltammetry
EN	Electrochemical Noise
PSD	Power spectra density
C _{sc}	Space charge capacitance
C _{dl}	Double layer capacitance
R _p	Polarization resistance
MS	Mott-Schottky
FFT	Fast Fourier Transform

1. Introduction

One of the great scientific and technical successes of this century is the creation of nanomaterials and nanotechnology. At the present time, many scientific and technical international conferences fully or partially devoted to nanomaterials are held, and the number of publications in various fields of this science continues to increase.

The American national nanotechnology initiative (N N I) defines the term “Nanotechnology” as including all the following: (1) research and technology development at the atomic, molecular, or macromolecular levels in the length scale of approximately 1 to 100 nanometer range; (2) creating and using structures, devices and systems that have novel properties and functions because of their small and/or intermediate size; (3) the ability to control or manipulate on the atomic scale [1]. Therefore, the concept of controlling matter at the atomic level is at the heart of nanotechnology. This term (nanotechnology) was created in 1974 by the Japanese researcher Norio Taniguchi to refer to engineering at length scale less than a micrometer [2]. At this period, nanotechnology remained unclear because of the lack of rudimentary tools to observe nanoparticles. This changed in the early 1980s with the invention of scanning tunneling microscopy by IBM. Later the invention of the transmission electron microscope and its variants has given us insight into nanoscale materials. The field of nanostructure science and technology has been growing very rapidly in the past few years [2, 3].

There is a wide range of disciplines contributing to the development of nanostructure science and technology; all use specific terminology to classify nanomaterial. The “aspect ratio” of a solid is defined as its length divided by its width. The term “nanodot” is generally referred to an object with the aspect ratio equal to one. A “nanorod” is an object with an aspect ratio between 1 and 20, with the short dimension on the 10-100 nm scales. A “nanowire” is an object with the aspect ratio greater than 20, with the short dimension on the 10-100 nm scale [4].

Nanomaterials have applications to a variety of area including physics, electronics, optics, Chemistry and biomedical science [5]. As examples, nanocrystalline soft magnetic materials have low energy lose. In RAM (Random Access Memory), a high ratio of magnetoresistance combined with a small coercive switching field is a key to density and speed. Low power magnetic storage elements of about 0.25 μm in size have been demonstrated [6, 7]. Recently, the shape memory effect of single crystalline copper nanowire was reported [8]. Moreover, the plasmonic resonance in metallic nanostructure has potential applications in near field optical lithography, surface-enhanced Raman spectroscopy, nanooptics [9] and plasmonic circuits offer

the possibility to carry optical signals and electric current through the same thin metal circuit [10]. Carbon nanotubes can be used to fabricate materials with better mechanical properties. They are also used as mould to shape quantum wires and as miniature test tubes. External decoration of nanotubes with metal atoms has been demonstrated and is predicted to have application in catalysis [11, 12]. Single-walled carbon nanotubes have been used as building blocks to fabricate room temperature field-effect transistor [13, 14]. In medicine, nanoparticles and nanospheres can be used as drug delivery systems or be injected into the circulatory system [15a].

Important recent developments in the field of creating miniaturized structure include the synthesis of nanoscale devices by template growth in the membrane channels of anodic aluminum oxide or porous polycarbonate. Porous templates were extensively used to produce carbon ultra microelectrode ensemble with radii close to 100 nm [15b], gold nanodisk [15c] and Ni/Cu multilayers in the form of nanowire of diameter ranging from 60 to 80 nm [15d]. Ultra microelectrode ensembles yield electroanalytical detection limits lower than that of the macrosized electrode [15e].

In addition to this broader range of applications, nanotechnology research is by all accounts in its infancy, and its applications are in embryonic stage [3]. Therefore, nanoscience innovation need to be conceptually developed and the methods of preparation of nanoparticles to be optimized.

The main goal of the present work is to deposit metallic and alloy nanoparticles by template self-organization. We focus our attention on paramagnetic metal (Cobalt) and alloy (NiCo, NiCu, ZnNi) because of their applications in data storage memories and electronic devices.

Many transition metals were deposited with anodic aluminum oxide (AAO), but in most works, the alumina was separated from the aluminum foil and a metallic film was evaporated on one side of the membrane for electrical conduction. Particles deposited in this condition are difficult to handle (the membrane is generally about 1-5 μ m thick) and the periodicity between particles is destroyed after dissolution of the template.

A reinvestigation of this method of deposition without separating the alumina from aluminum could be advantageous. Deposition within the pore of alumina with intact barrier layer is not straightforward because of the presence of a barrier layer at the bottom of the pores. In appropriate conditions, the process (deposition with intact barrier layer) may allow the formation of ordered metallic nanoparticles on aluminum surface. This method could offer a new way of modification of aluminum surface; it may also find applications in the electronics industry since aluminum is a good electrical conductor.

Another aim of this study is to control the nanostructure size and size distribution through the principle of double template deposition; that is the combination of alumina membrane with another template such as lyotropic liquid crystal. The hexagonal and cubic phases of lyotropic liquid crystal containing metallic ions were extensively used to synthesize metallic nanomaterial with very fine structure. Size effect plays an important role on chemical, optical and magnetic characteristics of materials. Moreover, it will be very interesting to understand the critical roles that surfaces and interfaces play in nanostructured materials, and to know in details not only the structure but also the local electrochemistry of nanomaterials. Therefore, the investigation of some electrochemical properties (impedance, semiconductivity, corrosion) of the mesoporous materials should be necessary to understand their behavior in aqueous solution.

The dissertation will be divided into six sections. A short introduction and the overview of the template deposition and characterization techniques will be discussed in the first and second section respectively, followed by the experimental details in part three.

The fourth section will deal with the preparation and characterization of the porous alumina membrane, the electrochemical deposition of cobalt nanorods from aqueous solution into the pore of alumina membrane with intact barrier layer, and the principle of double template deposition of cobalt nanomaterial. In this part, the electrochemical properties of cobalt nanofilm (impedance, semiconductivity, polarization behavior and corrosion) will be discussed.

The electrochemical deposition of ZnNi, NiCo and NiCu alloy nanofilms will be studied in section five. The surface topography of each alloy prepared from three different plating mixtures will be compared. The electrochemical properties of each alloy nanomaterial such as impedance, polarization behavior and semiconductivity, or the influence of the size of particles on the corrosion potential will be investigated.

The last section (section 6) will be devoted to the summary of the work.

2. Preparation and characterization of nanoparticles and nanofilms

Many methods have been developed for the preparation of nanomaterials ranging from lithographic techniques [16] to chemical [17, 18] and electrochemical methods. Numerous groups have explored a fabrication method termed “template synthesis” [19-23]; this process involves synthesizing a desired material within the pores of porous membranes. The feature of these methods is that it is extremely general with regard to the type of material that can be prepared. Template methods have been used to prepare nanofibers, nanotubes, semiconductors and other type of nanomaterials [24]. Most work in this area deals with two types of media: the nanoporous aluminum oxide and the liquid crystalline medium. A summary of the template methods of preparation of nanoporous materials will be developed in this part. A short description of some characterization techniques used in the work such as AFM / STM (Atomic Force Microscopy / Scanning Tunneling Microscopy) and electrochemical impedance spectroscopy (EIS) will be described.

2.1 Porous aluminum oxide as template for nanomaterial.

The structure of porous alumina membrane has been known since 1932 [25] and the oxide film on aluminum consists of two regions; an outer region of thick porous type and a thin compact inner region lying adjacent to the metal. This film with disordered structures was used to protect aluminum against corrosion. Recently (in 1995), Masuda and Fukuda [26] established the procedure to produce highly ordered nanohole arrays on aluminum foil and the explosion of work on porous alumina occurred. Porous alumina membranes are prepared by double anodization of aluminum in acidic solution [26-28]. The idealized structure of this film is shown in Fig. 2.1a [27]. The membrane contains cylindrical pores of uniform diameter, arranged in hexagonal arrays. A thin oxide layer exists at the bottom of each pore.

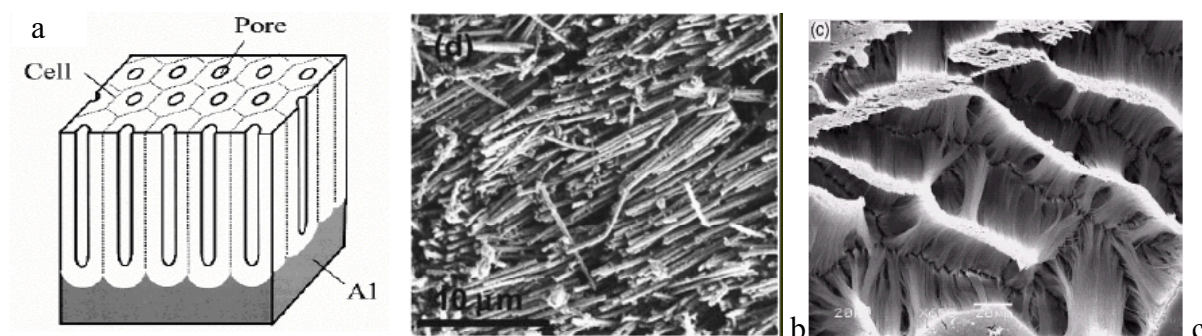


Fig. 2.1. Schematic drawing of the idealized structure of anodic porous alumina (a) [27]; top view of the nanomaterial after dissolution of the AAO membrane (b) [37a] and (c) [37].

Membranes with pore diameters as large as 200 nm and as small as 5 nm have been prepared. The pore parameters depend on the anodization conditions: type of acid, applied voltage, temperature and time. Pore density of about 10^{11} per cm^2 and thickness of 1 mm was achieved. The higher pore density is necessary for nanofabrication since it could allow a greater number of nanostructures to be produced per unit area [24, 27, 29]. Wide variety of transition metals including Ni, Co, Fe [30, 31], Cu [32], Au [29] and semiconductors [22, 33] were prepared using alumina membrane. The porous membrane is generally separated from the aluminum foil and the under barrier layer removed. Electrochemical deposition of metals within the pore is accomplished by coating one side of the membrane with metal film (via sputtering or thermal evaporation) and using this film as cathode [34-36]. The inconvenience of this method is the difficulty to handle the material or to prepare nanoparticles in large scale. The order between particles is destroyed (as show in Fig. 2.1b-c) after dissolution of the alumina. It could be interesting to maintain the porous film on aluminum and optimize the electric parameters to achieve homogeneous filling of the pores by metal particles. Moreover, deposition with intact barrier layer (without separating the oxide from the substrate) could offer the possibility to prepare nanoparticles in large scale or to modify aluminum surface with various metallic nanoparticles.

2.2 Surfactants and liquid crystal templates.

Surfactant molecules have a water-soluble head (hydrophilic group) and the insoluble group which is the hydrophobic part. The polar nature of the hydrophilic head is responsible for its solubility in water, whereas the hydrophobic group is non polar and insoluble in water. The surfactant molecules have characteristics of both hydrophilic and hydrophobic molecules; they are known as amphiphiles. Amphiphiles compounds have the unique ability to form structures that combine long-range periodicity in one, two or three dimensions [38, 39].

Self-organization of molecular species is fundamental to the generation of nanoscale architectures that have specific structure and function [40]. If a small amount of surfactant is mixed with water, it would be completely soluble. When the concentration of the amphiphilic material increases, molecules begin to form aggregates; the polar group on one side and the non-polar tail goes into the center of the sphere. This spherical structure formed by self-organization of surfactants in water is called a micelle. The micelles are stable when the surfactant is above a certain concentration called the critical micelle concentration generally

less than 1 wt% of surfactant. When the concentration of the surfactant in water continues to rise, the micelles come together and form micellar cubic phase, hexagonal phase, cubic Ia3d and lamellar phase, respectively [38, 41-42].

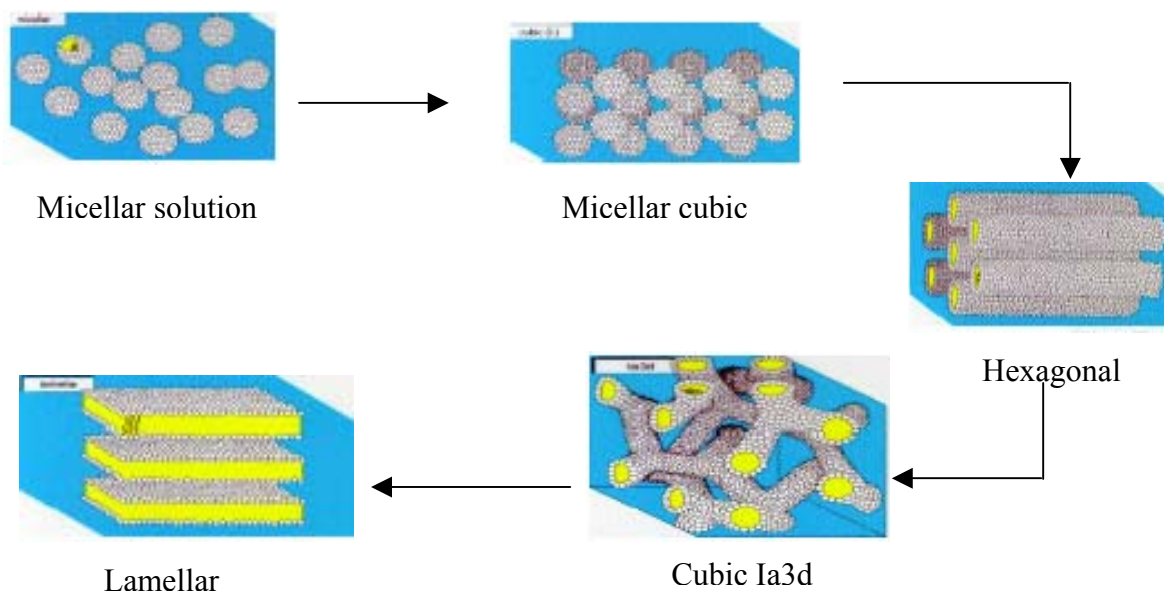


Fig.2.2. Schematic of liquid crystal phase structure with increasing surfactant concentration [43].

The structures formed beyond the critical micelle concentrations are said to be liquid crystalline. That is a class of organic mixture with unusually low melting temperature. In liquid crystal mixtures, large numbers of molecules are oriented along some preferred direction, producing fluid but structurally anisotropic phases. The molecules in liquid crystals don't have the disorder arrangement associated with the liquid state of material. The mixture formed by mixing large amount of surfactant with water is called lyotropic liquid crystal. The phase behavior (micellar, cubic, hexagonal and lamellar) in lyotropic systems is a function of composition, temperature and molecular structure of the amphiphilic compound [44-49].

The most important surfactants widely used as emulsifying agent [50] and as templates to produce nanomaterials [23, 51, 52] are the *n*-alkylpolyethylene glycol ethers known as polyoxyethylene compounds. They have a long polyoxyethylene chain at the middle of the molecules; a hydrocarbon chain is attached at one end and a hydroxyl group exists at the other end. Their general formulation is $C_nH_{2n+1}(CH_2CHO)_mOH$ or $n-C_nH_{2n+1}(CH_2CH_2O)_mOH$ [50].

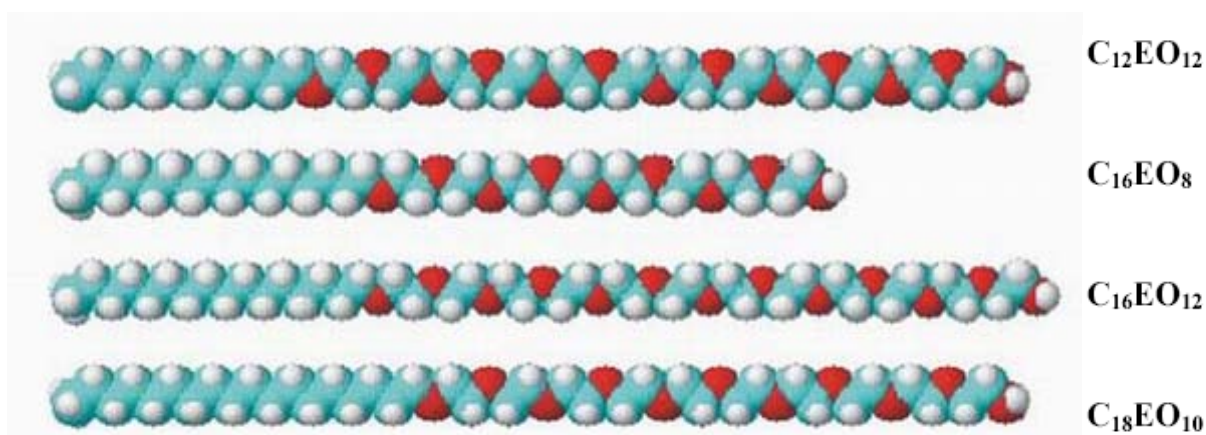


Fig. 2. 3. Structure of non-ionic surfactants [53]

Ionic surfactants are also used to prepare nanomaterials. Among them, the most interesting is the cetyltrimethylammonium bromide (CTAB) $\text{CH}_3(\text{CH}_2)_{15}\text{N}(\text{CH}_3)_3\text{Br}$. In CTAB + water system, electrostatic repulsion between the positively charged ionic groups dominates. Consequently structure with a high positive mean curvature, where the head groups are well spaced in comparison to hydrocarbon tails, are favored. Therefore, a large hexagonal domain dominates the phase diagram of the CTAB/water system [38].

- Principle of deposition using liquid crystal as template.

Mesoporous materials can be prepared from lamellar, cubic and hexagonal phases of lyotropic liquid crystals. But the hexagonal phase is widely used since it gives material with hexagonal array of cylindrical holes [54-56]. The principle of liquid crystal template deposition is illustrated by the following figure [43].

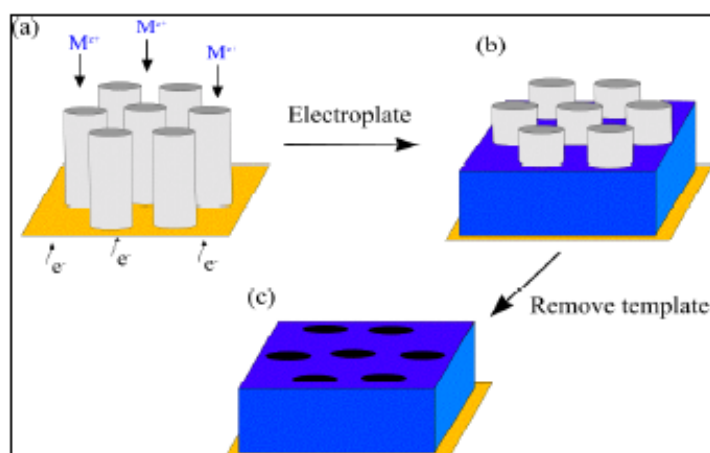


Fig. 2. 4. Principle of template deposition [43].

The electrodeposition reaction is constrained to the areas of the conductive substrate that remains exposed to electrolyte after application of the template. This method has been used to prepare a large variety of transition metal mesoporous films [40-60], semiconductors such as CdS [61], ZnO, Cu₂O [62], CuS [63] and NiCo alloy [64]. The influence of the electrodeposition conditions on the properties of mesoporous platinum [54] and the electrochemical reactivity of the same film was also studied.

2.3 Characterization of mesoporous films

Different types of microscopes including atomic force microscope (AFM), scanning electron microscope (SEM), transmission electron microscope (TEM) and electrochemical methods such as impedance spectroscopy can be used to characterize mesoporous films.

2.3.1 Scanning probe techniques

Scanning probe microscopes are a family of instruments used to study surface properties of materials from the atomic to the micron level. The other class of instruments used for surface analysis is the electron microscope. The advantage of the scanning probe microscope is that it gives the 3D resolution of the surface. In some case, this type of microscopes can measure physical properties such as surface conductivity, static charge distribution, magnetic field and elastic module [65].

The atomic force microscope (AFM) is one of the most interesting analysis tools in the SPMs family. The atomic force microscope probes the surface of a sample with a sharp tip, a couple of microns long and often less than 100Å in diameter. The tip is located at the end of a cantilever that is 100 to 200 µm long. Forces between the tip and the sample surface cause the cantilever to bend or deflect. The force commonly associated with AFM is the interatomic force also called Van Der Waals force. A detector measures the cantilever deflection as the tip is scanned over the sample, or the sample is scanned under the tip. The measured cantilever deflections allow a computer to generate a map of surface topography. AFM scanned the surface in 3D and the analysis of the images allow the determination of the average height of the particles, the root mean square roughness and the power spectra density gives the periodicity in the arrangement of particles [65].

- Average height

The average length of the particle can be deduced from a digital AFM image by the relation:

$$Z = \frac{1}{N} \sum_{i=0}^N Z_i \quad (1)$$

Where N is the number of particles on the selected surface and Zi the height of particle numbers i, Z in nm.

-Root Mean square Roughness (RMS)

The RMS roughness calculates the standard deviation of the surface irregularities with respect to some mean line or curve. It is commonly used to characterize optical components; in general the lower the RMS value, the less light is scattered by an optical surface, and hence the better the surface quality [66]. This parameter is used when the distribution of surface irregularities is random. Its value depends on the sampling length. For a surface profile Zi, RMS is given by the following expression from [66]:

$$R M S = \sqrt{\frac{1}{N} \sum_{i=1}^N Z_i^2} \quad R M S \text{ in nm} \quad (2)$$

-Power spectra density (special wavelength)

The power spectra density (PSD) is defined as the square magnitude of the Fourier transform of the surface profile Z (j). For digital image, the PSD is obtained from the following expression [66].

$$P S D (f) = \frac{\Delta}{N} \left| \sum_{j=1}^N Z (j) e^{-2 \pi f (i - 1) \Delta} \right|^2 \quad (3)$$

Where f is the spatial frequency in μm^{-1} , Δ is the sampling interval, i the complex number ($i = \sqrt{-1}$), Z (j) in \AA , PSD (f) is the power spectra density in $\text{\AA}^2 \cdot \mu\text{m}$.

The power spectra density allows the determination of the repeat distance in the sample that has ordered arrangement of particles. The PSD of the sine wave has one peak located at the spatial wavelength of the sine wave, while the more random profile from ground surface has a PSD comprising a lot of wavelengths [66]. The inverse of this wavelength is the periodicity or repeat distance: $d = 1/f$, where f is the spatial frequency.

2.3.2 Electrochemical impedance spectroscopy

Electrochemical impedance spectroscopy (EIS) is a well-established powerful technique for investigating many electrical properties of materials and their interfaces. This technique has been used for studying corrosion processes, interfacial reaction mechanisms, and dynamics of mobile charge in bulk or interfacial regions of any material. The flow rate of charged particles and current depends on the Ohmic resistance of the electrodes and the electrolyte. Large number of parameters can be deduced from EIS data; the material properties such as conductivity, dielectric constant, relaxation frequency and the interfacial properties such as adsorption-reaction rate constants, interface capacitance, diffusion coefficient. From the theoretical point of view, the impedance and the capacitance are quantities that are interesting to measure [67, 68].

The impedance method is based on the classical principle of transfer function. The system under investigation is perturbed with a sinusoidal wave (voltage) input and the response (current) is measured at the output [69].

$$E_t = E_0 \exp(j\omega t) \quad (4)$$

$E_0 =$ Amplitude in Volt
 $\omega = 2\pi f$ is the radial frequency in rad/s
 $j =$ Complex element

If the system is linear, the response of the applied sinusoidal voltage is a sinusoidal current with the same frequency and different phase and amplitude [69, 70].

$$I_t = I_0 \exp j(\omega t - \phi) \quad (5)$$

$I_0 =$ Amplitude in Ampere
 $\phi =$ phase shift in rad

The ratio between the response and the input signal determines the complex transfer function of the system. This ratio is known as the admittance of the system; the impedance of the system is simply the reciprocal of its admittance. Measurement of the current responses to voltage excitations (admittances) is often easier than the voltage response to current excitations (impedance). However, the admittance is measured and the impedance is computed from the data [69-71].

$$Z(\omega) = \frac{E_t}{I_t} = \frac{E_0 \exp(j\omega t)}{I_0 \exp j(\omega t - \phi)} = |Z| \exp(j\phi) \quad (6)$$

The impedance can be represented as a complex number, from the Eulers relationship,

$$e^{j\phi} = \cos \phi + j \sin \phi \quad (7)$$

The impedance can be written as

$$Z = Z' + j Z'' \quad (8)$$

where $j = \sqrt{-1}$, $Z' = |Z| \cos \phi$ and $Z'' = |Z| \sin \phi$.

The impedance is expressed as a vector, where the raw data at each measured frequency consists of the real and imaginary components of the applied potential and measured current.

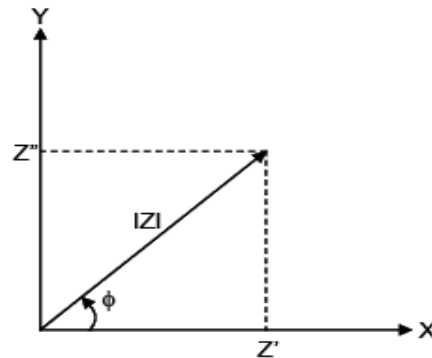


Fig. 2.5. Impedance planar vector representation

The phase shift ϕ for each applied frequency is given by

$$\phi = \arctan\left(\frac{Z''}{Z'}\right) \quad (9)$$

and the absolute impedance magnitude by [72, 73].

$$|Z| = \sqrt{Z'^2 + Z''^2} \quad (10)$$

The total impedance of a circuit is that of all its resistor, capacitors and inductors. The opposition of a capacitor and inductor to the flow of electrons is called reactance.

2.3.2.1 Data presentation

- Nyquist diagram

The most common graphical representation of the experimental impedance data is the complex-plane (Nyquist) diagram. It describes the dependence $f(Z', Z'')$ in Cartesian co-ordinates.

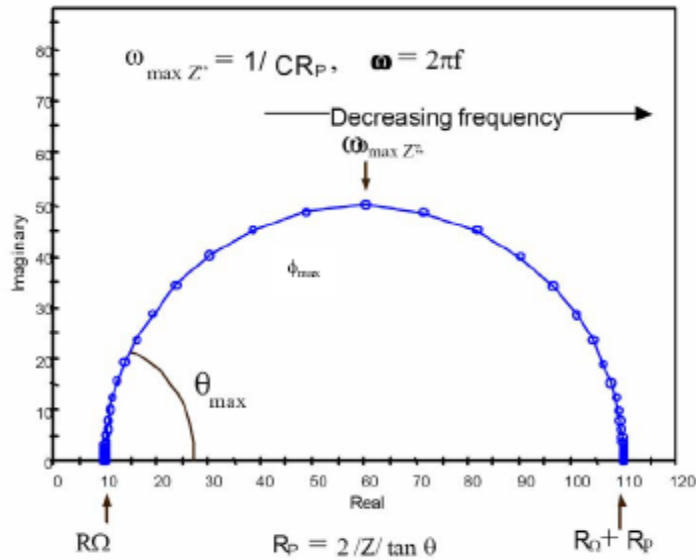


Fig. 2.6. Nyquist plot or complex impedance diagram for an equivalent circuit of simple electrochemical cell [73].

The plot illustrates the expected response of simple corrosion systems, which are entirely under charge transfer control [68]. At high frequencies, only the uncompensated resistance (all Ohmic resistances in the system such as electrolyte and cable resistance) contributes to the real portion of the impedance. At low frequencies, the polarization resistance (R_p) or charge transfer resistance also contributes to this measurement. The Nyquist plot shown in Fig. 2.6 is for a simple cell known as Randles cell [69-72]. Many parameters can be deduced from Nyquist representation. The intercept of the semicircle with the real axis at high frequencies give the solution resistance while at low frequencies, it gives the sum of polarization resistance and the solution resistance ($R_p + R_\Omega$). At intermediate frequencies, the imaginary part of the impedance (Z'') reaches the maximum value. The frequency corresponding to Z''_{max} is called characteristic frequency [69]; it is used to calculate the double layer capacitance according to the following relation [68, 74, 75].

$$C_{dl} = \frac{1}{R_p \omega_{max}} = \frac{1}{2\pi f_{max} R_p} \quad (11)$$

Where R_p is the polarization resistance (Ohm), ω the angular frequency (rad/s) and C_{dl} the double layer capacitance (Farad).

The Nyquist plot often contains several semicircles; only a portion of a semicircle is observed in some cases. The imaginary component of each semicircle reaches the maximum at the characteristic angular frequency; the reverse of this angular frequency is the time constant. It

controls the distribution of the total current between the charging of the capacitance and the electrochemical process [69, 70].

$$\tau = \frac{1}{\omega_{\max}} \quad (12)$$

τ is in seconds.

For a given semicircle of resistance R and capacitance C , the characteristic angular frequency is

$$\omega_{\max} = \frac{1}{RC} \quad (13)$$

R in Ohm, C in Farad and ω_{\max} in rad/s.

Therefore the time constant of each semicircle is given by [70, 76]

$$\tau = CR \quad (14)$$

One of the disadvantages of the Nyquist plot is that the dependence of the impedance on the frequency of the applied signal is not directly shown [77]. The Bode Plots offer another alternative to display EIS data.

-Bode representation

In Bode-plots, $\log|Z|$ or $|Z|$ and the phase angle are plotted versus $\log(f)$. One of the advantage of such representation is the possibility to detect the regions that are dominated by resistive elements such as R_{Ω} and R_p in which a slope of zero is observed; and regions dominated by capacitive elements for which a slope of -1 is observed in the ideal case [68]. The Bode plot of a simple electrochemical cell (Randles cell) is showed on Fig. 2.7 [73]

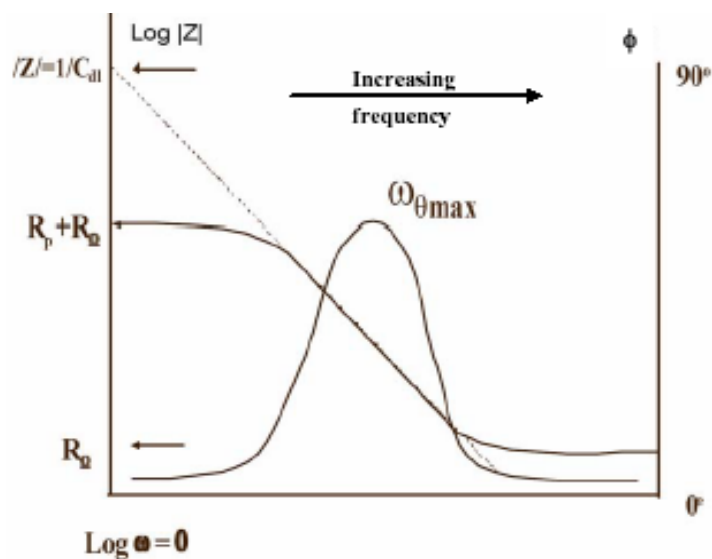


Fig. 2.7. Bode plot of simple electrochemical cell [73].

This representation permits the examination of the absolute impedance, the Ohmic resistance R_{Ω} and the polarization resistance R_p . At highest frequency, the logarithm of the solution resistance can be read as shown in the figure. Similarly the $\log(R_{\Omega} + R_p)$ can be deduced from lower frequency horizontal plateau. The extrapolation of the straight line obtained at intermediate frequencies to $\log|Z|$ axis, allows the determination of the double layer capacitance. $C_{dl} = 1/|Z|$ where $|Z|$ is the impedance magnitude at the y-axis intercept (in Ohm). Bode representation provides a clearer description of the electrochemical system's frequency dependence behavior than does the Nyquist plot [73].

2.3.2.2 Impedance data analysis

The aim of the impedance analysis is to identify the appropriate working model that corresponds to the experimental data. Most of the circuit elements in the model are common electrical elements such as resistors, capacitors and inductors. To be useful, the elements in the model should have a basis in the physical electrochemistry of the system. Therefore, components such as the constant phase element (CPE) and the Warburg element (W) need to be introduced in the model [69].

- Constant phase element (CPE or Q)

The material and interface electrical or dielectrical properties often do not behave ideally. The CPE represents an empirical relationship, which is introduced to describe the frequency dependence, caused by electrode surface roughness or by non-uniformly distributed properties of the irregular electrode surface [69, 78, 79]. Its impedance is described by the following relation [80-82].

$$Z = \frac{1}{A (j\omega)^\alpha} \quad j = \sqrt{-1} \quad (15)$$

Where ω is the angular frequency in rad/s; A is the CPE constant and α is its exponent, $0 \leq \alpha \leq 1$. For $\alpha = 1$, an ideal capacitor is obtained ($A = C$); for $\alpha = 0$ $A = 1 / R$, the CPE represent an ideal resistor. The double layer capacitor of real cells often behaves like a CPE.

- Warburg element

Diffusion of charge carriers in materials also creates impedance called the Warburg-impedance. It depends on the frequency of the potential perturbation. At high frequencies, the Warburg impedance is small since diffusing reactants don't have to move very far. At low frequencies the reactants have to diffuse farther, increasing the Warburg impedance [72]. The Warburg impedance is given by the following expression [69, 83].

$$Z_w = \frac{\sigma}{\sqrt{j\omega}} \quad (16)$$

Where ω is the angular frequency in rad/s and σ the Warburg parameter that include the diffusion coefficients.

This expression is valid only for semi-infinite diffusion. The impedance of the common elements used for data analysis is summarized in the following table.

Tab.2.1. Impedance of circuit elements

Circuit element (symbol)	Impedance equation	Dimensions
Resistor (R)	$Z = R$	R in Ω
Capacitor (C)	$Z = \frac{1}{j\omega C}$	C in F w in Rad.s ⁻¹
Inductor (L)	$Z = j\omega L$	L in H
Constant phase element (CPE)	$Z = \frac{1}{A(j\omega)^\alpha}$	A in F.s ^{$\alpha-1$}
warburg (semi-infinite diffusion) (W)	$Z_w = \frac{\sigma}{\sqrt{j\omega}}$	σ in $\Omega.s^{-1/2}$

-Double layer capacitance

The electrical double layer is the array of charged particles and oriented dipoles that exists at every material interface. In electrochemistry, such a layer reflects the ionic zones formed in solution to compensate for the excess of charge on the electrode. The double layer has a complex structure of several distinct parts. The compact layer close to the electrode and containing the outer and the inner Helmholtz plane, is made of solvent molecules and specifically adsorbed ions. The outer layer beyond the compact layer is the diffuse layer. The electrical double layer resembles an ordinary (parallel-plate) capacitor [84, 85].

$$C_{dl} = \frac{Q}{A(E - E_{pzc})} \quad (17)$$

Where A is the specific area of the electrode (cm²), E the applied potential (V), E_{pzc} the potential of zero charge (V) and Q the electric charge of the capacitor in Coulomb.

The value of the double layer capacitance depends on many variables: the electrode potential, temperature, ionic concentrations, type of ions, oxide layers, electrode roughness and impurity adsorption [72].

In the case of semiconductor-electrolyte interface, the capacitance is related to the space charge layer capacitance, C_s , and the Helmholtz layer capacitance, C_H , according to the relation [86].

$$C^{-1} = C_s^{-1} + C_H^{-1} \quad (18)$$

The space charge capacitance of a semiconductor electrode varies with the applied potential. Mott-Schottky relationship expresses the potential dependence of the electrode under depletion (band bending in semiconductor due to the applied potential) condition [87, 88].

$$\frac{1}{C_s^2} = \frac{2}{\varepsilon \varepsilon_0 q N_D} \left[E - E_{fb} - \frac{kT}{q} \right] \quad (19)$$

Where q is the elementary charge (+ e for electrons and $-e$ for vacancy), ε the dielectric constant of the material, ε_0 , the permittivity of vacuum, N the doping density of state, k the Boltzmann constant, T is the absolute temperature, E_{fb} is the flatband potential and C_s the space charge capacitance in Farad. This enables one to determine the flatband potential from an impedance measurement by plotting C_s^{-2} as function of potential E . The plot may be fitted with a straight line according to equation 19. Determining the flatband potential is very important to understand the interface behavior. This allows the location of the semiconductor band edges on the redox potential scale, or to determine the bandgap energy, $V_v - V_c = E_g/q$; where V_v and V_c are the valence and conduction band potential respectively, E_g the bandgap energy and q the absolute value of the electron charge [87].

3 Experimental parts

3.1 Reagents

Reagents of analytical grade were used without further purification: oxalic acid (Laborchemie Apolda), cobalt sulfate heptahydrate (Merck), ascorbic acid 99% (Acros organics), zinc chloride 98% (Aldrich), copper sulfate pentahydrate (Laborchemie Apolda), chromium oxide 99,9%(Acros organics), nickel sulfate heptahydrate and nickel chloride (Laborchemie Apolda) lithium perchlorate (Fulka), polyoxyethylene(20)-stearylether, (Brij78, Acros organics), decaethylenoxide monooctadecylether, (Brij76 Aldrich), hexadecyltrimethylammonium bromide 99% (CTAB, Acros organics), phosphoric acid 85 wt% (Acros organics).

3.2 Preparation of the templates

- Anodic aluminum oxide (AAO)

The thin alumina membrane used for experiments was prepared by a modified two steps anodization described by Masuda [26]. The aluminum foil was electropolished with 15 V_{DC} for 3 min in a mixture of 25 Vol% HClO₄ and 75 Vol% ethanol. Anodization was performed during 30 min in 0.3 M oxalic acid at various temperatures with 40 V_{DC}. The first anodic film formed in this condition was removed at 60 °C in a mixture of 0.2 M CrO₃ and 0.4 M H₃PO₄. The foil was anodized again for 30 min. Under these conditions, the aluminum oxide with hexagonal porous structure was obtained on aluminum. In order to study the influence of the electrolyte temperature on the pore parameters, foils were anodized at 0, 10, 20, 30 and 40 °C. The temperature of the electrolyte was controlled by a thermostated water bath. The perforated alumina remains on the aluminum foil; all depositions were made with intact barrier layer.

- Liquid crystal template

The plating mixture consists of a non-ionic surfactant C₁₈ [EO]_n; polyoxyethylene(20)stearyl ether (Acros organic Brij 78 with n =20) or decaethylenoxide monooctadecylether (Acros organic Brij 76 with n=10) or an ionic surfactant hexadecyltrimethylammonium bromide (Acros organic CTAB) and the aqueous solution containing metallic ions. The mixtures were prepared according to the procedure described by Attard et al. [45, 54, 57].

In the case of non-ionic plating mixture, the surfactant was heated to about 60 °C (above its melting point) in a glass and mixed on addition of the aqueous solution. After addition of the aqueous solution, mixing times of about 15 min under constant temperature (60° C) were required to obtain homogeneous mixtures.

For Brij78 plating mixture, the phase contains 60-65 wt% surfactant and 40-35 wt% aqueous solution. This composition range gives the hexagonal domain according to the phase diagram of a similar mixture described in [57] (see appendix). The Brij 76 mixture consists of 60 wt% surfactant and 40 wt% aqueous solution.

The hexagonal phase of the ionic surfactant (CTAB) was prepared by adding 50 wt% CTAB to 50 wt% aqueous solution. In this case the surfactant was not melted prior to addition of the solution. The mixture was heated to 30 °C after addition of the aqueous solution and mixed for about 10 min. According to the phase diagram of [38] (see appendix), the hexagonal phase of this mixture is obtained at temperatures higher than 25 °C.

3.3 Electrochemical deposition and characterization

3.3.1 Electrodeposition

Metallic and alloy nanomaterials were prepared by single and double template electrochemical methods.

In single template deposition technique, porous aluminum oxide on aluminum was used as working electrode. This electrode was mounted in a lab made electrochemical cell that allows the area of about 0.5 cm² to be in contact with solution. The electrode area for all deposition from aqueous solution within the pore of alumina was 0.5 cm². Ions dissolved in aqueous solution were reduced galvanostatically into the pore of the membrane using the Potentiostat / Galvanostat Model 273 A (PAR, EG&G Princeton Applied Research) connected to a computer. Graphite was used as counter electrode. The electric parameters (Current density, deposition time) were varied to achieve homogenous deposition of metallic nanorods. All deposition was done at room temperature.

In double template electrochemical deposition, the liquid crystal template was combined together with the aluminum oxide for deposition. The metal ions that should be reduced were dissolved in the aqueous solution used to prepare the liquid crystalline phase. With the non-ionic surfactant, the plating mixture was melted at 55–65 °C within the pore of the AAO. A thermoelectric module (Peltier element 193585-ZA) was mounted under the working electrode to regulate the temperature. Melting the liquid crystal is very important since the surfactant must wet the pore of the alumina membrane. The direct current Motor controller micropositionner C-842.20 (Physik Instrumente) was used to maintain the distance between the working and counter electrode to about 2 ± 0.1 mm in order to facilitate the electrical conduc-

tion. The ionic surfactant was heated at 30°C during deposition. The working station consists of a vibration-free table (Newport, USA) used to isolate the motor against vibrations. The DC motor controller M-126 DG of the micro machine drives two axes directly from a PC with C-842 WinMove software. This model has the following features:

- 25 mm travel range
- XY stages
- 118.6 c/ μm linear transmission ration
- 0.0085 μm linear resolution
- 0.1 μm minimum incremental motion
- minimal velocity 8.432 $\mu\text{m/s}$
- maximal velocity 1012 $\mu\text{m/s}$

The current was supplied with the same potentiostat 273A which operates from a PC via the IEEE-488 interface port (National Instruments USA).

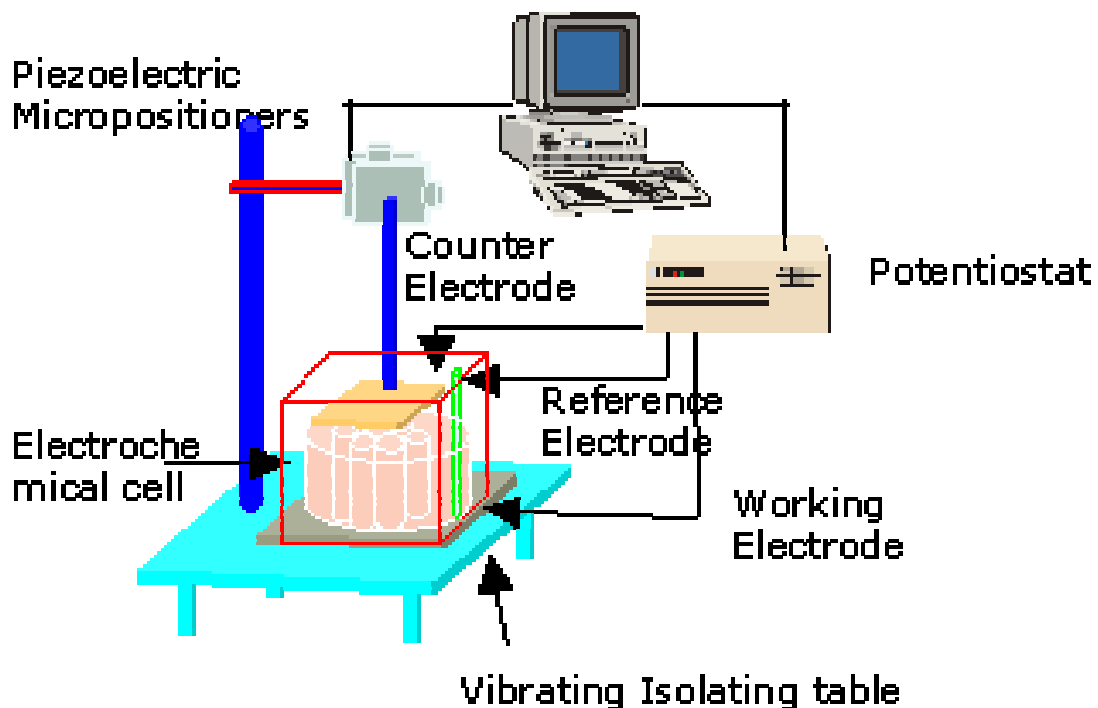


Fig. 3.1. Block diagram of the working station used for double template deposition: Redraw from [53].

After deposition, the surfactant was removed by soaking the electrode in distilled water for at least 6 hours; during this time the water was replaced every 2 hours. At the end, the electrode was cleaned with distilled water, dried in air and analyzed with AFM or STM.

3.3.2 Characterization

-Atomic force microscopy (AFM) and scanning tunneling microscopy (STM)

The surface of the anodic alumina membrane and the electrodeposited materials was analyzed by atomic force microscopy or by scanning tunneling microscopy.

AFM measurements were performed at room temperature under ambient conditions of approximately $35 \pm 10\%$ relative humidity using the TopoMetrix TMX 2010 Discoverer. The instrument operated in non-contact mode with a silicon tip and a cantilever resonance frequency of 321 kHz. The scan rate was generally the double of the scan range (for a scan range of $5\mu\text{m}$, the scan rate was $10\mu\text{m/s}$) and the “set point” was adjusted during measurements to obtain images with good resolution. The “integral” and “derivative” feedbacks were almost the half of the “proportional” feedback. All AFM images are direct topography without filter.

For double template deposition using CTAB liquid crystal, the surface of the film was analyzed by STM. The same AFM (TopoMetrix 2010) instrument was switched into STM by replacing the AFM head by the STM head; changing the scanner, connecting the bias wire to the new scanner, connecting the 8 pin STM scanner cable to the 8 pin connector labeled XYZ located on the translator. Details concerning this procedure can be found in [89].

The STM operated in constant current mode with a platinum-iridium tip. The tip was etched electrochemically (20 V_{AC}) in a mixture of 60 / 36 / 4 vol% of KCl_{sat} , H_2O and HCl respectively. The HCl was a 32 wt% concentrated solution. Details concerning the electrochemical preparation of STM tips are given in [90].

All AFM and STM images were analysed with WSxM 4.0 Develop 7.1 image browser software. The average height, the root means square roughness and the periodicity were deduced from AFM images by calculation using equations (1), (2) and (3) respectively. Gaussian filter was applied to STM images to eliminate noise.

- Electrochemical impedance spectroscopy (EIS)

Impedance spectra were recorded with the Lock-In Amplifier 5210 (PAR EG&G) coupled with the potentiostat / galvanostat 273A. The equipment were calibrated with the following electronic dummy Cell:

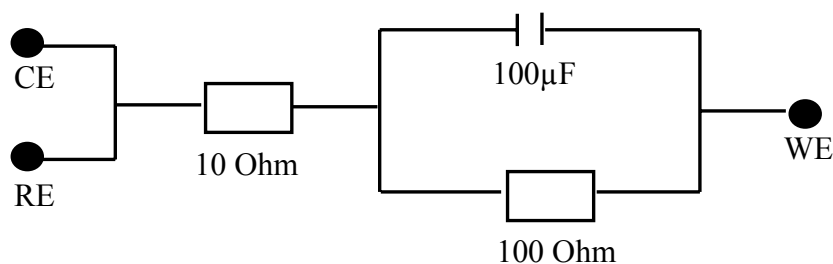


Fig. 3.2. Diagram of the dummy cell used for instrument calibration.

The parameters of the Lock-In Amplifier were changed and the impedance of the electronic cell (dummy cell) was recorded. The aim is to search for good parameters that give the optimal response of the system. The impedance data recorded with the dummy cell was fitted and the values of the capacitance and resistance were compared with that reported on the electronic cell as shown in figure 3.2. The calibration will be successful if the numerical values of the fitting data are in agreement with the values reported on the cell.

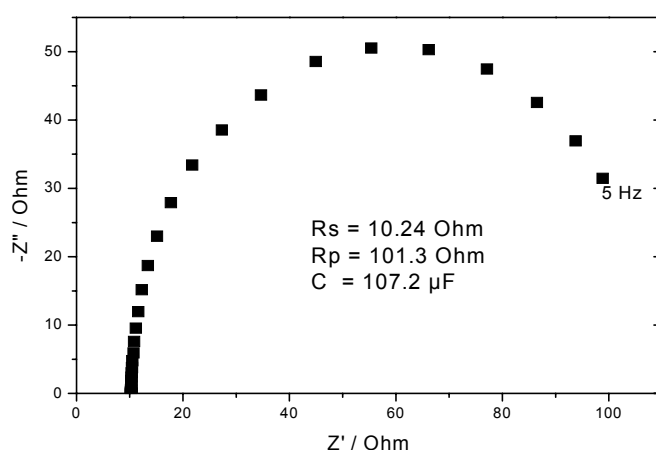


Fig. 3.3. Nyquist representation of the impedance of dummy cell used for calibration, the inset shows the numerical values obtained by fitting.

The numerical values of the resistors and capacitor of the dummy cell measured by the instrument are shown in Fig. 3.3. All values are close to those reported on the electronic cell and account for good calibration. After many measurements, the calibration was checked and no deviation was observed.

All impedance spectra were recorded in 0.4 M LiClO₄ with low ac amplitude (10 mV in the case of AAO and 5 mV for all metallic film) to ensure the linear response of the system and avoid destruction of the film during measurement. The electrode was maintained at a constant

DC potential to obtain the steady-state condition required for impedance measurement. The value of the DC potential depends on the film under investigation. The frequency was stepped from 100 kHz to 5 Hz with 10 points per decade. Impedance data were fitted with ZsimDemo 3.2 simulation software operating with non-linear least square algorithm.

- Semiconductivity measurements: Mott-Schottky plot

The semiconductor behavior of the films was investigated in 0.4 M LiClO₄ with 1 kHz and 5 mV ac amplitude of sinusoidal voltage. The CompactStat instrument BO5030 (InVium electrochemical interface) operating in potentiodynamic electrochemical impedance spectroscopy mode measured the space charge capacitance (C_s) of the material as a function of the electrode potential (in single operation) and the InVium software allows the analysis of results in term of Mott-Schottky plot.

- Electrochemical noise measurements

The electrochemical current noise between a pair of identical electrode was measured in 0.4 M LiClO₄ with the CompactStat instrument B05030. The current noise is the galvanic current flowing between two identical working electrodes. The WE + Sense was connected to the working electrode one while Ground (Gnd) was attached to the WE two. A SCE was used as reference electrode; no additional counter electrode was used.

- Polarization curves and corrosion measurements

Potentiodynamic analysis of the nanostructured materials was performed in 0.4 M LiClO₄ with the potentiostat / galvanostat 273A. The working station consists of a saturated calomel electrode (RE), a platinum foil (CE) and the aluminum electrode coated with nanoparticles (WE).

For all electroanalysis or spectroscopy measurements, the area of the WE in contact with the electrolyte was 0.2 cm². Measurements were carried out at room temperature, without stirring and in the presence of (open-air) diluted oxygen.

4. Template deposition of cobalt nanoparticles

4.1 Preparation and characterization of porous alumina membrane.

4.1.1 Preparation of AAO

Anodic alumina membrane presents a highly ordered porous structure, consisting of an array of hexagonal cells perpendicular to the surface and separated from the anodized metal by a barrier type oxide film [28]. However, the geometry of the anodic porous alumina usually obtained is far from that of the idealized model. Moreover, the thickness of the barrier layer has influence on the electrodeposition process when the membrane is not separated from the metal. The dependence of long-range ordering of holes configurations on the anodization voltage has been studied in various electrolytes. It appears that ordered AAO membrane can be obtained at 25V in sulfuric acid solution, at 195 V in phosphoric acid solution and at 40 V in oxalic acid [27]. The anodization temperature and time may also influence the structure of the alumina and particularly the thickness of the under barrier layer. The aim of this part is to prepare a thin AAO film with a smallest under barrier layer; this small barrier layer will allow electrons to flow across the membrane during deposition.

The preparation of AAO was done in three steps: electropolishing of the foil, first and second anodization.

The electropolishing process is the removal of grease and mirror texture of the aluminum foil. A commercial aluminum foil (15 x 55 x 0.5 mm) was electropolished under galvanostatic condition (15 V_{DC}) in a 25:75 volume mixture HClO₄ and C₂H₅OH during three minutes. Potentiodynamic and potentiostatic experiments were carried out to understand the mechanism of the process.

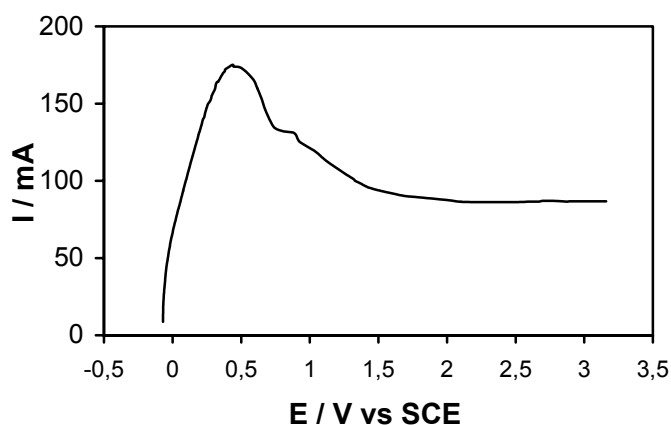


Fig. 4.1.1. Potentiodynamic curve recorded during the electropolishing of aluminum foil in 25:75 volume mixtures of perchloric acid and ethanol. Scan rate 1.5 mV/s

The current-potential curve recorded during the electropolishing process shows a typical passive behavior of aluminum. This classical curve shows an active phase at potential below 0.5 V vs SCE and a passive phase above the given potential. Current-time function was recorded at more positive potential (3.5V vs SCE) and the curve obtained is shown in Fig. 4.1.2.

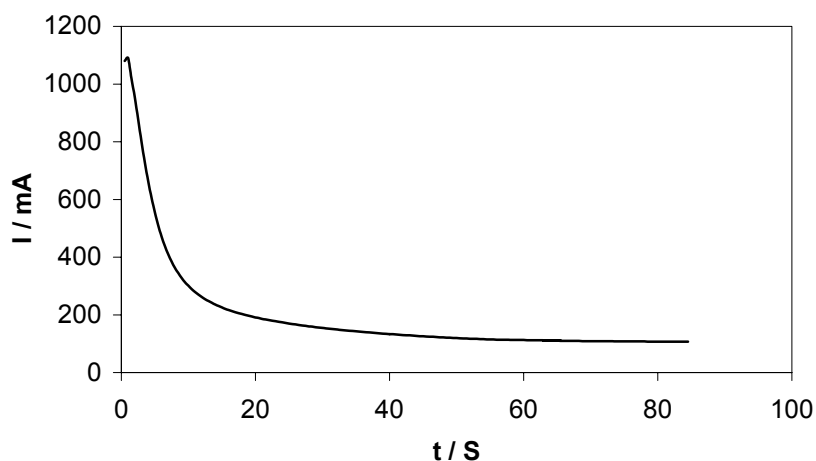


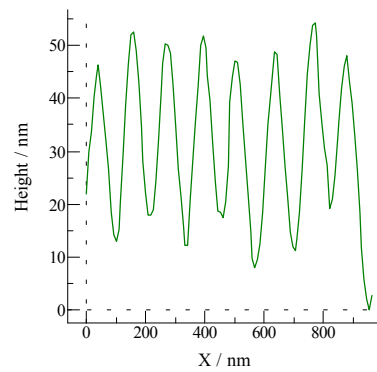
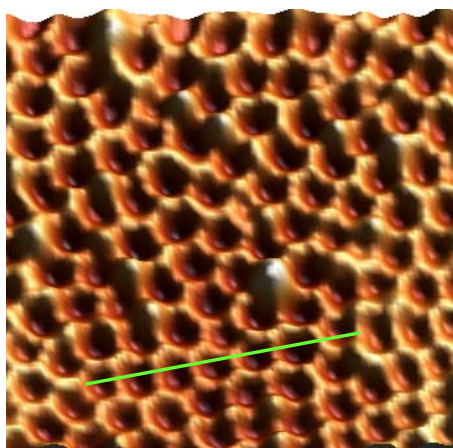
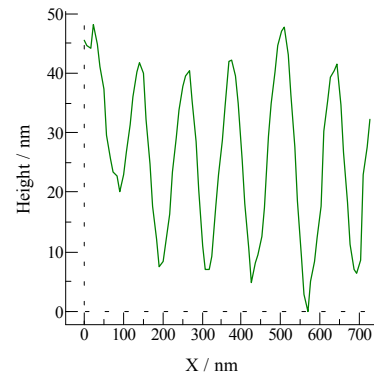
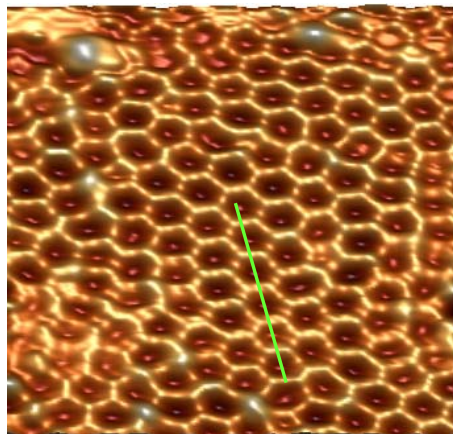
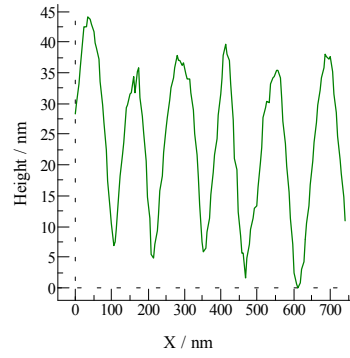
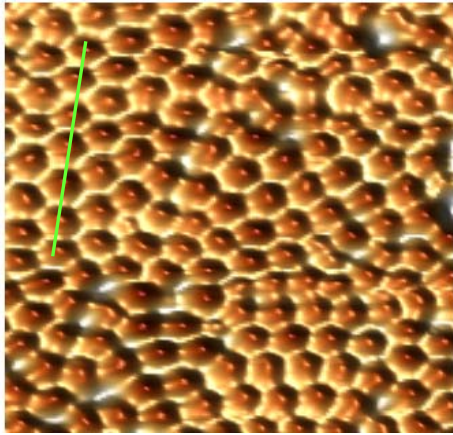
Fig. 4.1.2. Potentiostatic curve recorded at 3.5V vs SCE at the beginning of the electropolishing of aluminum foil.

It can be observed from the diagram that current decreases exponentially during the first 40s and becomes constant at a value close to 100 mA. This indicates a rapid passivation of the aluminum electrode at high electrode potential. Electropolishing creates a surface texture with hexagonal cells of about 100 nm [91]; those cells will form the hexagonal pores during anodization. The unstable patterns also appear by implicating the adsorption of alcohols on the surface [92]. The formation of the patterns leads to a thin passive film that accounts for the decreasing of current during the polishing process.

The electropolished aluminum foil was anodized in 0.3 M oxalic acid solution under constant voltage (40V) for 30 min. Immersing the foil in a mixture of 0.2 M CrO_3 and 0.4 M H_3PO_4 for 10 min at 60°C leads to the dissolution of the outer part of the AAO formed during the first anodization. The aluminum sheet was rinsed intensively with distilled water and anodized for 30 min in oxalic acid (second anodization). The anodization experiment was repeated at different temperatures to study the influence of the temperature on the structure of the film and the thickness of the barrier layer. Samples were anodized at 0, 10, 20, 30 and 40°C. At each temperature, three samples were prepared to be sure that the structure obtained could be reproduced. The temperature was controlled with a thermostated water bath.

4.1.2 Characterization of AAO: AFM and impedance spectroscopy

Atomic force microscopy (AFM) was used to examine the AAO surfaces and the pore diameter, depth and roughness factor of each sample were deduced from picture analysis.



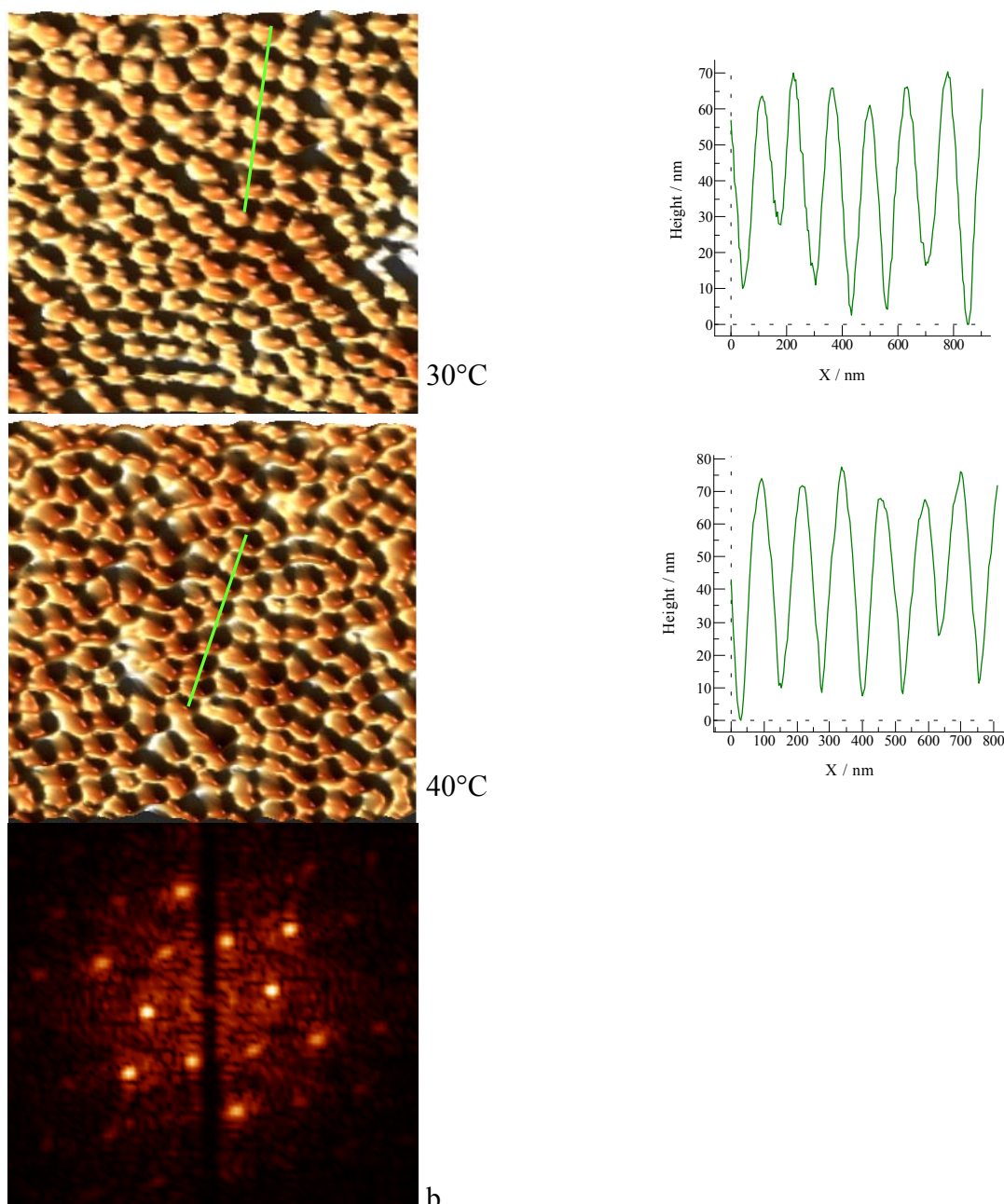


Fig. 4.1.3. AFM images of porous alumina anodized at different temperature in 0.3 M oxalic acid with 40 V_{DC}. The anodization time was 30 min for the first and second anodization. The profile along the line shows the thickness of the film in each case; (b) is the 2D Fourier transform (FFT) of the image of the sample anodized at 10°C. Each picture is 1.6 x 1.6 μm².

Investigation of the pore arrangement revealed that the cell homogeneity on the AAO surface decreases dramatically as soon as the anodization temperature is higher than 20 °C. A very disordered structure was obtained at 50 °C. The most highly ordered AAO film was obtained at 10 °C. The pores with narrow size distribution are surrounded by hexagonal oxides, which are interconnected to form a network structure. The 2D FFT of the image of the sample prepared at

10°C (Fig.4.1.3b) shows clearly the hexagonal symmetry in the organization of porous AAO cells. The inter-pore separation of this sample is about 110 nm. In general, the degree of self-ordering of the hexagonal cell increases at low anodization temperature. According to Bocchetta et al. [28], a relatively low electrolyte temperature favors the formation of hard and abrasion resistance anodic film. Each picture was analyzed; the average pore diameter at mid-height, depth and the root mean square surface roughness of the samples were determined. The variation of these parameters with the anodization temperature is summarized in the following graphs.

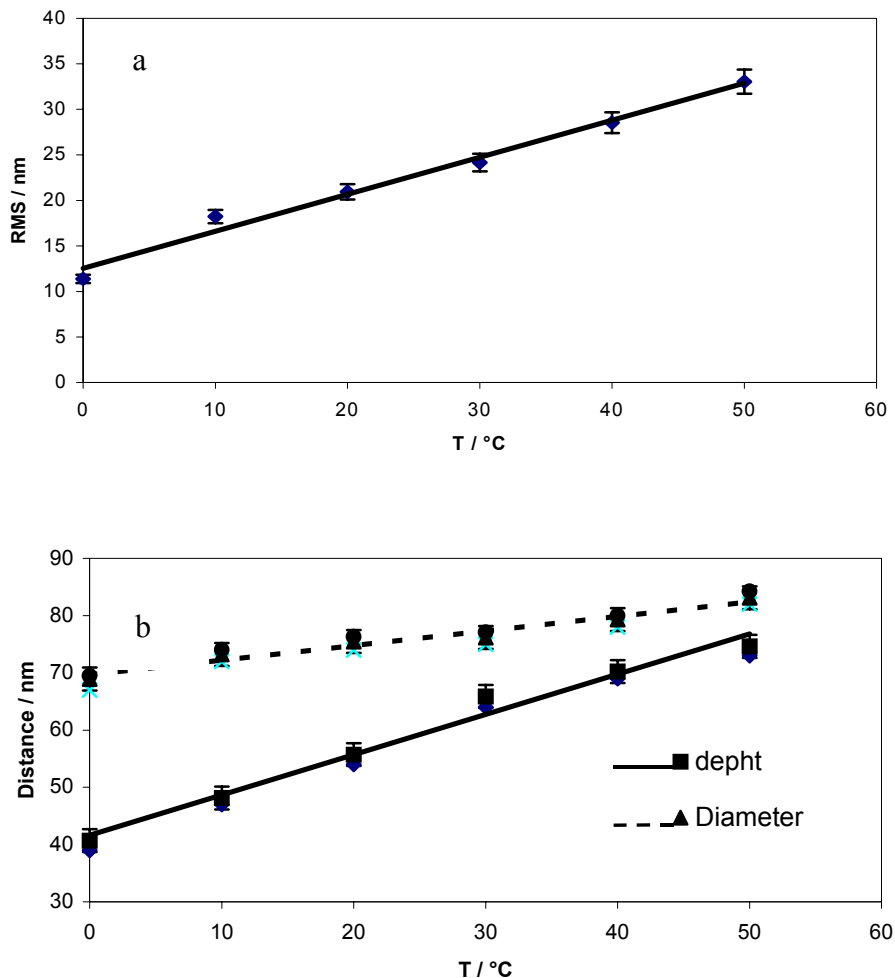


Fig. 4.1.4. Variation of the surface roughness (a), pore depths and diameters at mid height (b) of the AAO anodized in 0.3 M oxalic acid with temperature.

The effects of the anodization temperature on pore parameters of AAO are shown in Fig. 4.1.4. The results from the graphs show that, the root mean square roughness, the pore diameters and depth are linear function of the anodization temperature. Increasing the temperature will favor

the formation of thick anodic film with wide pore diameters. Changing the temperature may vary the rate of the chemical reactions that lead to the formation of the aluminum oxide. The variation of the rate of formation of AAO could influence the arrangement of aluminum oxide molecules on the surface of aluminum foil.

A mechanical stress mechanism was proposed to explain the self-ordering of anodic aluminum. The repulsive forces between neighboring pores caused by mechanical stress at the metal/oxide interface promote the formation of hexagonally ordered pore arrangement. According to this theory, the expansion of aluminum during oxidation leads to less than twice the original volume under usual experimental conditions. The expansion strongly depends on experimental conditions. Ordered arrangements are accomplished by moderate expansion of aluminum; whereas no ordered domains can be observed in the cases of contraction or very strong volume expansion [93]. Therefore the variation of pore parameters with the anodization temperature can be understood since the expansion depends on temperature.

A self ordered hexagonal array of cylindrical pores has been fabricated by double anodization of aluminum sheet in 0.3M oxalic acid at temperature between 0 and 50°C, and the dependence of pore parameter on temperature was investigated. But the AFM cannot give information about the barrier layer situated at the bottom of the pores, or the exact thickness of the AAO membrane. The pore depths displayed on Fig. 4.1.4b are approximate since the AFM tip may not go deeper in the pore to measure the real height. The thickness and the electrical properties of this layer may affect the electrochemical deposition when the membrane is used with intact barrier layer. Therefore it is interesting to know the anodization temperature that gives AAO film with lower electric resistance.

-Impedance of porous aluminum oxide

The aim of this work is to optimize the deposition of nanoparticle within the pore of alumina membrane with intact barrier layer. It is well known that the aluminum oxide film is an electrical insulator. When this membrane is porous and thin enough, it can be polarized. In order to test the possibility of charge transfer across the thin $\text{Al}_2\text{O}_3/\text{Al}$ electrode, the impedance spectra of the porous film prepared under different anodization conditions were measured. Fig 4.1.5 shows the complex plane representation of the impedance data of the aluminum oxide film on aluminum.

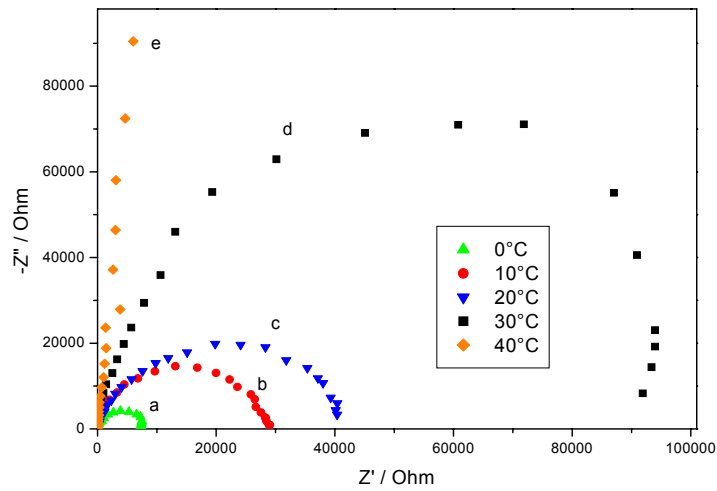
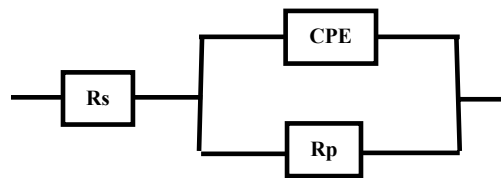


Fig. 4.1.5. Nyquist representation of the impedance of porous alumina film on aluminum.

The impedance spectra were recorded in 0.4 M LiClO₄ with 10 mV ac amplitude of sinusoidal voltage and the frequency range from 100 kHz to 5 Hz. The electrode DC potential was -1 V vs SCE. The amplitude of the AC signal was chosen to be small enough to obtain the linear response of the material. Except for the curve e, i.e. the sample anodized at 40°C, all films exhibit Nyquist-like diagram characteristic of electrode processes that are entirely under charge transfer control [68]. The following Randles type of equivalent circuit (EC) was used to analyze the experimental data of film under charge transfer control.



$$Z(j\omega) = R_s + \frac{R_p + R_p^2 A \omega^\alpha \left[\cos \frac{\alpha\pi}{2} - j \sin \frac{\alpha\pi}{2} \right]}{1 + R_p^2 A^2 \omega^{2\alpha} + 2R_p A \omega^\alpha \cos \frac{\alpha\pi}{2}} \quad (20)$$

The double layer capacitance is represented in the model by the constant phase element that accounts for the non ideal behavior of this layer. Rp and Rs represent the polarization and the solution resistance, respectively. The mathematical dependence of the complex impedance on the frequency of the sinusoidal voltage (shown on equation 20) was determined by adding together the instantaneous impedance expression of various elements, as they were resistors. That is, the impedance of elements in series adds directly while the admittance of elements in

parallel is also added [71]. See appendix for details about this calculation and for the example of fitted curves.

Tab. 4.1.1. Polarization resistance (R_p) and CPE variables (A & α) of porous aluminum oxide. The values were obtained by fitting the experimental result with the proposed model.

Temperature		0°C	10°C	20°C	30°C
Rs [Ω]		53.82	39.71	26.88	23.49
Rp [Ωcm^{-2}]		3.8×10^4	1.4×10^5	2.1×10^5	4.6×10^5
CPE	α	0.98	0.83	0.89	0.75
	A [$\mu\text{F}\cdot\text{cm}^{-2} \text{s}^{\alpha-1}$]	0.067	0.051	0.049	0.019

It appears from Fig. 4.1.5 and Tab. 4.1.1 that the polarization resistance of the alumina / aluminum electrode increases with the anodization temperature. Porous film with high charge transfer resistance is not appropriate for the deposition of nanoparticles; the electrochemical process at this electrode will be difficult due to the higher resistance.

The film anodized at 40°C shows impedance spectrum (vertical line nearly perpendicular to the real axis of Fig. 4.1.5) close to Nyquist representation of pure capacitive system. This ideally polarizable electrode is characterized by the absence of any process (no charge transfer and no reaction) at the surface. The impedance of such system contains only the electrolyte resistance and the double layer capacitance; this gives a vertical line in Nyquist plot [68, 69]. In the present case, the small deviation from the vertical behavior is caused by the inhomogeneity and electrode roughness. This film has very high impedance values; the pore of the membrane could have been partially sealed at high temperatures. Or the under barrier layer could be very thick in this case. The measurement also confirms the absence of charge transfer across the film. Therefore it cannot be used for the preparation of nanoparticles.

Combining the result of AFM and EIS measurements, it is easy to choose the optimal condition to prepare AAO film that can be used for nanomaterials. AFM analysis reveals that the porous AAO anodized at 10°C contains well organized pore geometry. From impedance results, it is observed that the same film has a relatively low polarization resistance (that is, it allows charge to flow easily than the film with larger polarization resistance) and impedance values. It is easier for electrons to tunnel across the barrier layer of films anodized at 10 °C. The electrode prepared at this temperature is appropriate for intact barrier deposition of nanoparticles.

In the next sections, all depositions and experiments will be described with respect to alumina / aluminum working electrode anodized at 10 °C.

4.2 Electrochemical deposition of cobalt nanorods from aqueous solution to the pore of AAO.

Two methods have been developed to obtain uniform and complete filling of the pores of AAO by electrodeposition. In the first (deposition in open pore templates) the membrane is detached from the aluminum substrate. This method is applicable when the AAO is stable enough to handle and the thickness is greater than 20µm. For most of the nanostructure applications, a porous alumina of only a few hundred nanometers is required [92]. In the second method (deposition with intact barrier layer), the aluminum oxide remains on its substrate and the metal is deposited on the barrier layer at the pore tips. The advantage of this method is ease of material handling [92, 93]. Only few report exits on direct deposition of metal on alumina with intact barrier layer. Using this method, Nielsch et al. [92] achieve homogeneous deposition of nickel by pulse current (with short I_{pulse} of 70 mA/cm²) within the pores of 1µm thick membrane. According to [92], high potentials are required for the electrons to tunnel through the barrier layer. Moreover, electrodeposition by direct current is very unstable and uniform filling of the pores cannot be achieved.

Since the AAO membrane prepared in the present work is thin enough ($h < 80\text{nm}$), we expected that electrons could tunnel across its barrier layer (as shown by EIS) during electrodeposition with direct current. Furthermore, homogenous filling of the pores could be achieved by appropriate control of electric parameters.

The electrolyte used for cobalt deposition consists of 0.5 mol/l CoSO₄ 7H₂O, 5x10⁻³ mol/l ascorbic acid and 0.3 mol/l H₃BO₃. The electrodeposition is carried out galvanostatically in a cell with an alumina/aluminum working electrode and a graphite counter electrode. The distance between electrodes is about 1cm.

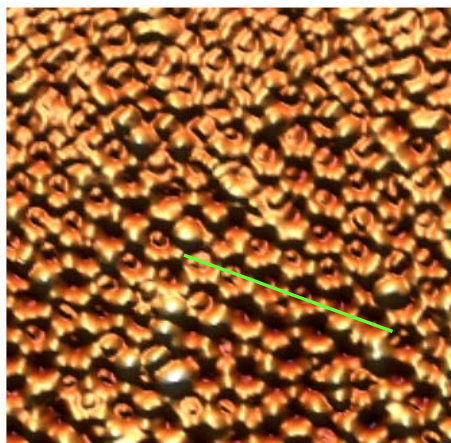
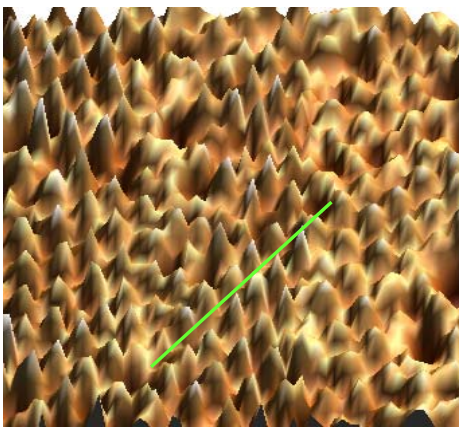
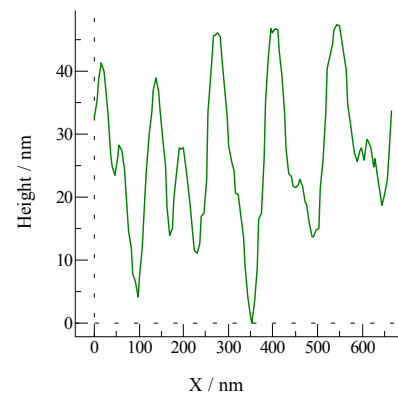
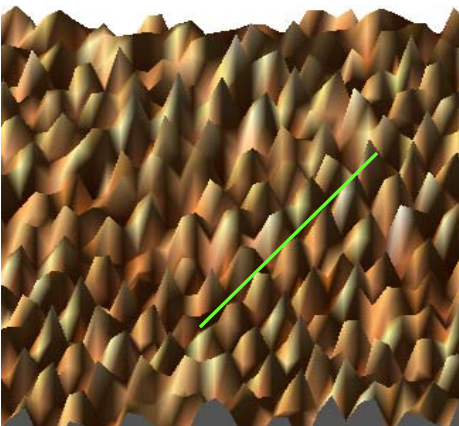
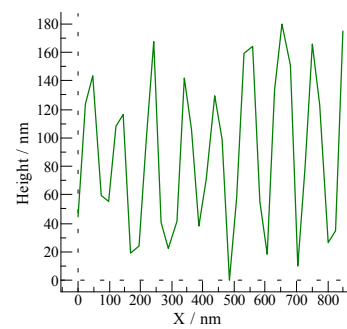
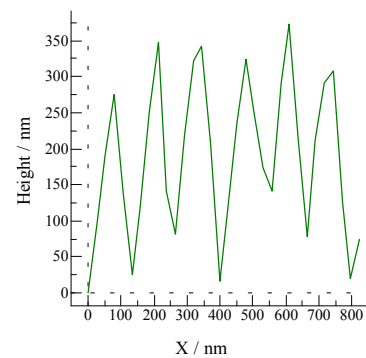
4.2.1 Influence of the deposition charge on the structure of cobalt nanomaterial

All experiments were carried out with a current density of 1 mA/cm²; varying the deposition time will change the quantity of electricity. The surface topography of the cobalt nanomaterial was determined by atomic force Microscopy (AFM).

The variation of the surface topography with the deposition charge is represented on Fig. 4.2.1.

At lower quantity of electricity (Fig. 4.2.1a), the pores are partially filled with cobalt. The hexagonal structure of the AAO is observed and nanodots can be seen at the bottom of each pore. This picture shows the initial stage of electrochemical deposition of cobalt particles in the pore of AAO.

The hexagonal structure of the AAO disappears when the deposition charge increases. Pictures b and c show the beginning of the nucleation of cobalt out of the pore of the alumina membrane.

**a****b****c**

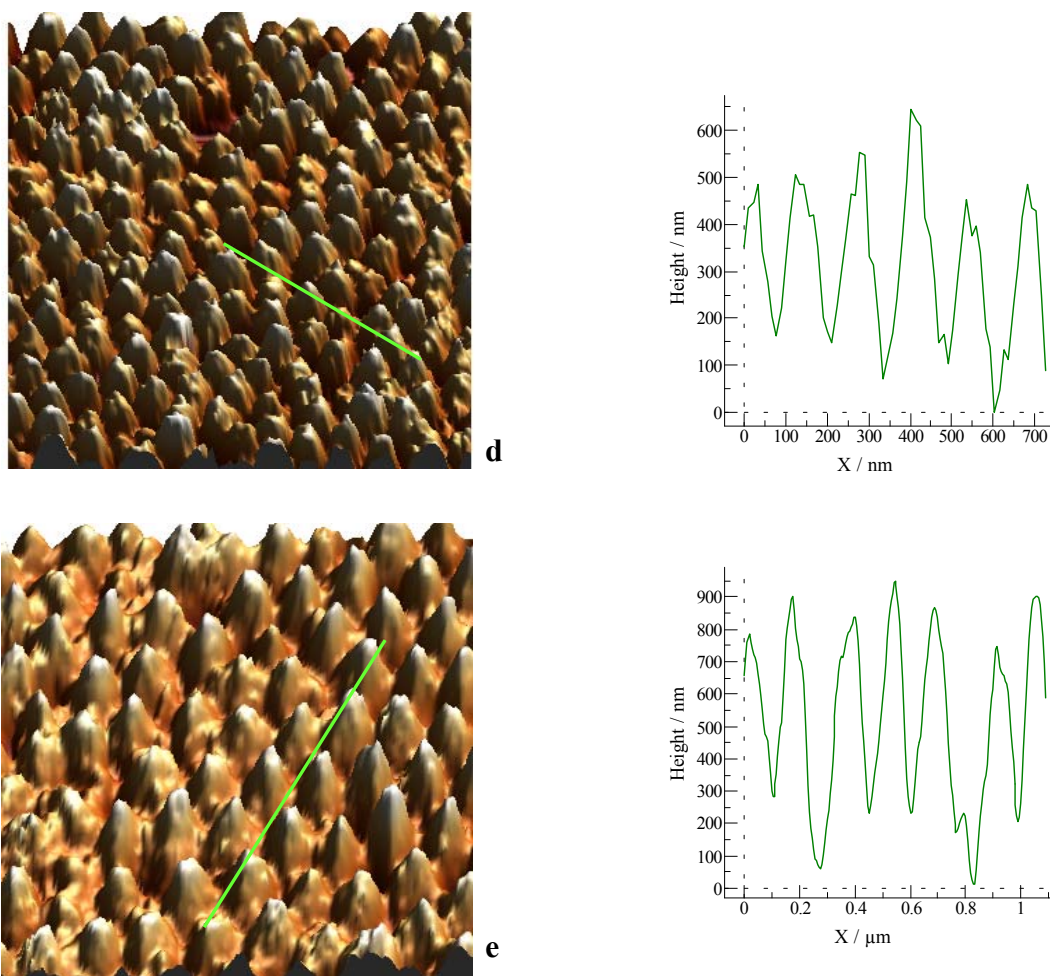


Fig. 4.2.1. Cobalt nanorods deposited with various quantity of electricity: a) 0.226 C, b) 0.452 C, c) 0.602 C, d) 0.753 C, e) 0.904 C. The profile along the line shows in each case, the thickness of the film. Each picture is $1.6 \times 1.6 \mu\text{m}^2$.

With higher deposition charge (Fig. 4.2.1d-e) well-defined nanorods with regular periodicity is observed. The profile along the line shows the thickness of the cobalt film at various deposition charges, the thickness of the films increases with the quantity of electricity. The average height and the root mean square roughness (RMS) of each sample were deduced by picture analysis. The variation of these parameters with the deposition charge is summarized in the following graphs.

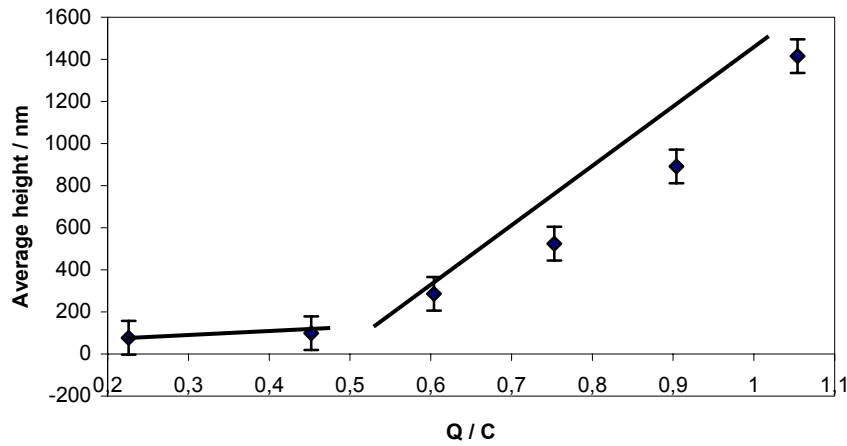


Fig. 4.2.2. Variation of the average height of the samples with the quantity of electricity. Films were deposited with a current density of 1 mA/cm².

Figure 4.2.2 shows the dependence of average height on deposition charge; it is clear that the deposition charge has a major influence on the structure. According to the Faraday law, the thickness of an electrodeposited film is proportional to the quantity of electricity.

$$h = \frac{ZQ}{ad} \quad \text{where} \quad Z = \frac{A}{nF} \quad \text{therefore,} \quad h = \frac{AQ}{nFad} \quad (21)$$

Where A is the atomic mass of the element in g / mol, a is the electrode area in cm², d the density of the element in g/cm³ and h the thickness in cm [94].

From this relation, a plot of the thickness of the film as function of Q should give a straight line passing through the origin at zero charge.

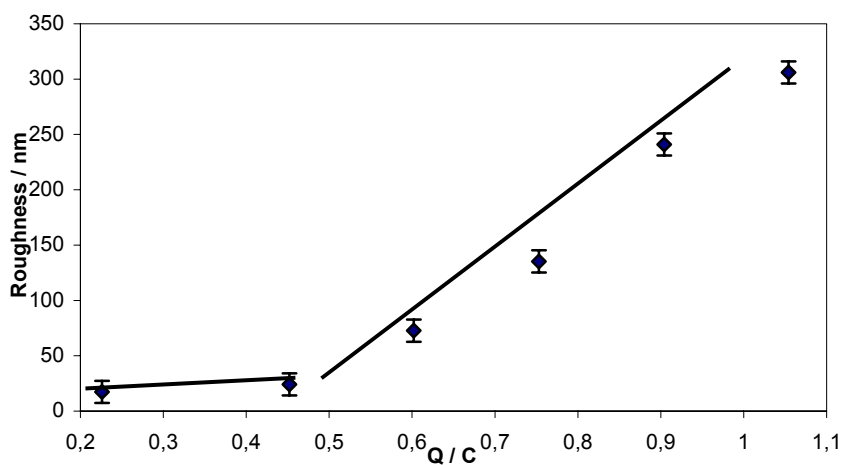


Fig. 4.2.3. Variation of root mean square roughness of the samples with deposition charge. Films were deposited with current density of 1 mA/cm².

Both the average height and the RMS factor are linear function of the quantity of electricity for Q values above 0.5 C. The observation is in agreement with the Faraday law as described by equation 21. At lower deposition charge (below 0.5 C), the process is more complex. In general, both the height and the RMS seem to increase very slowly with Q . As shown in Fig. 4.2.1a, the pores are partially filled at low charge; and it is normal that the RMS and the thickness of the samples should be close to that of the AAO membrane (See Fig.4.1.4) anodized at 10°C.

If we consider the density of cobalt, 8.65g/cm^3 , and the electrode area, 0.5 cm^2 , the thickness of cobalt film (calculated from equation 21) that will be deposited on the equivalent smooth area with a quantity of electricity of 0.5 C will be close to 340 nm. This value is obtained assuming 100% current efficiency. In real cells, some factors such as hydrogen evolution and Ohmic drop at the under barrier layer of the AAO may reduce the current efficiency. Therefore, it is possible that the pores should be partially filled at Q values below 0.5C as shown on Fig. 4.2.1a. From this analysis, the observed variation of the average height and the RMS with Q could be understood. The following models explain the growth process:

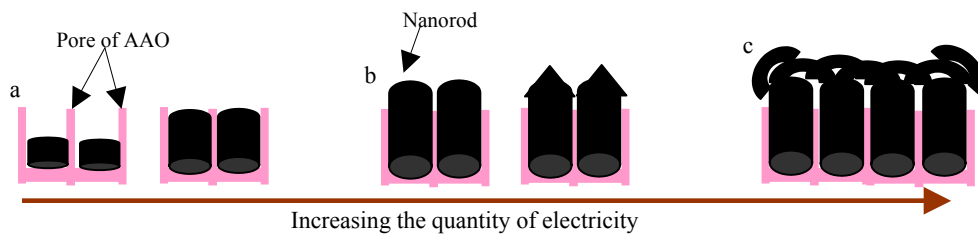


Fig. 4.2.4. Evolution of the length of nanorods during deposition into the pores of AAO.

When the electric charge is low (Fig.4.2.4a) the pores of AAO are partially filled; the RMS and the average height of such samples should be lower. At medium deposition charge (Fig. 4.2.4b), material grows out of the pore of AAO and the RMS and the height are more important. At this intermediate charge, the grow process follows equation 21. The nanorods overlap when the charge becomes more important (Fig.4.2.4c) and macro size particles are formed. This last case was not of interest in the present work.

It is important to mention that this result may suffer from some experimental error; the AFM tip may not go deeper enough to measure the exact length of the particles when the sample is very thick. Moreover, the morphology of the deposit is not really identical at each point of the surface; some areas have more material and disordered structure.

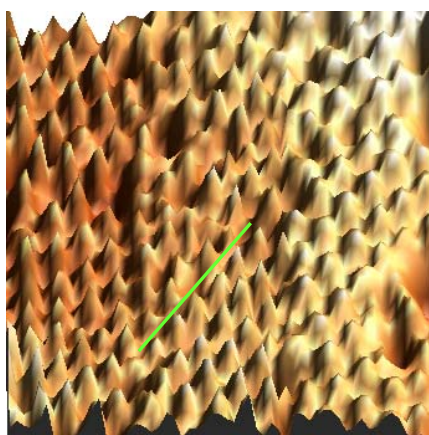
Comparative analysis of the deposits indicates that the nanorods are well formed when the charge is greater than 0.753C. The diameter of the particles at mid height is about 60 nm and the periodicity (center-to-center spacing between two neighboring fibers) determined by Fourier transform of the images is about 125 nm. In order to optimize the quality of the films, the electrochemical parameters such as the current density and time were varied.

4.2.2 Influence of the current density on the structure of cobalt nanomaterial.

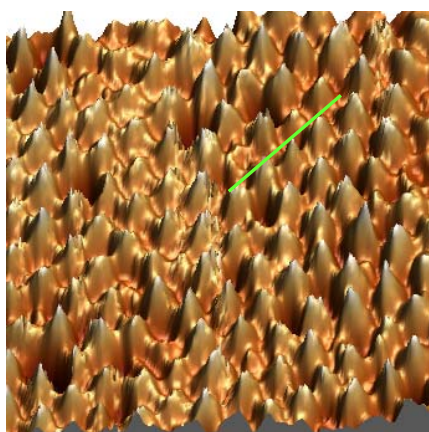
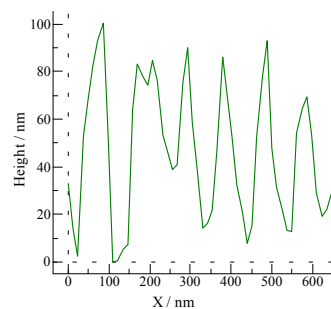
Samples were initially prepared by varying the current density and deposition charge at the same time. That is, the deposition time is constant and the current density varies; from one experiment to another the quantity of electricity ($Q = it$) should change. Secondly the current density was changed and the time was adjusted in such a way that the total quantity of electricity remains constant.

- Variation of current density at constant deposition time.

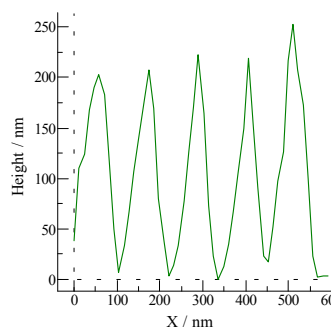
The deposition time was 900s with an electrolyte of the same concentration. The AFM micrographs of the samples are shown below.



a



b



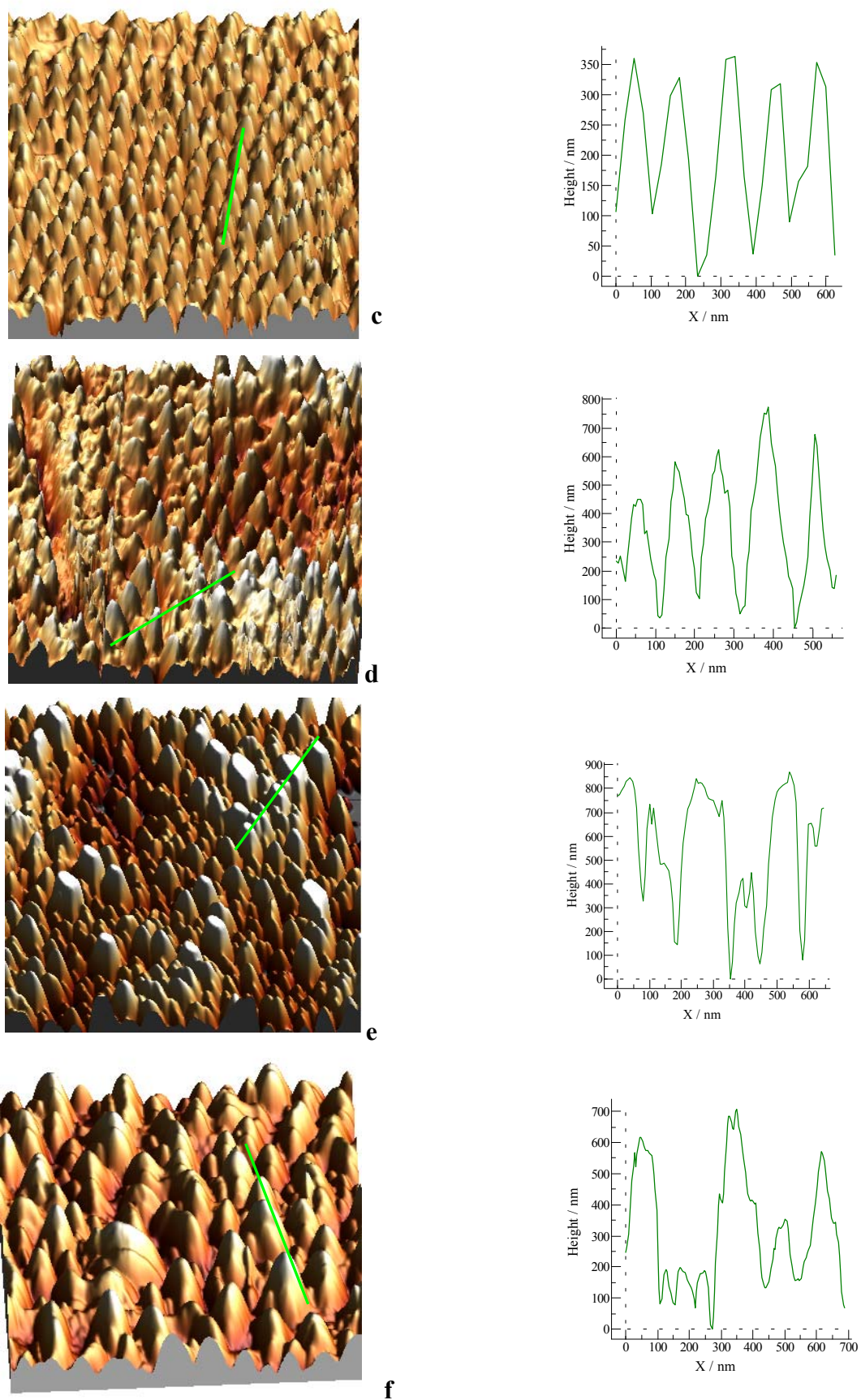


Fig. 4.2.5. Cobalt nanorods deposited at different current densities: a) 1, b) 2.5, c) 5, d) 7.5, e) 10 and f) 12.5 mA/cm². Each picture is 1.6 x 1.6 μm².

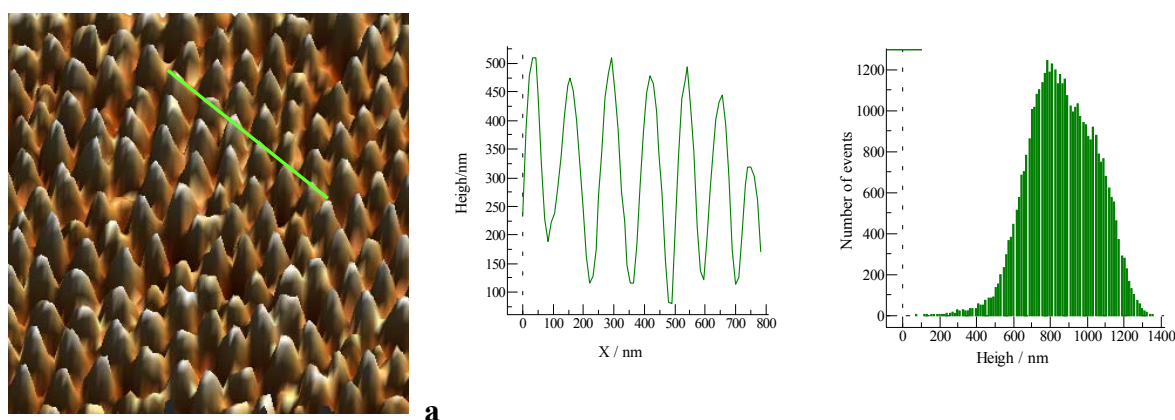
The effect of deposition current density is shown in Fig. 4.2.5. At lower magnification (a-c), particles of about 60 nm in diameter are present on the surface. This diameter is in the same range as the pore in aluminum oxide. It can be seen that the pores of the aluminum oxide are filled by the metal, the constant periodicity between these particles accounts for the homogeneous deposition of the material at low current density. At intermediate current density the same periodicity is observed but the nanorods are longer than in the last case.

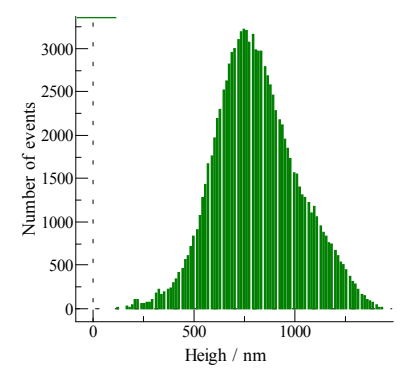
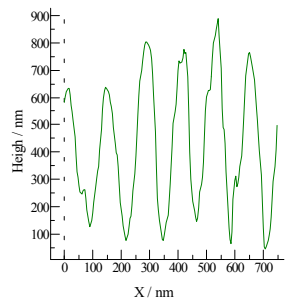
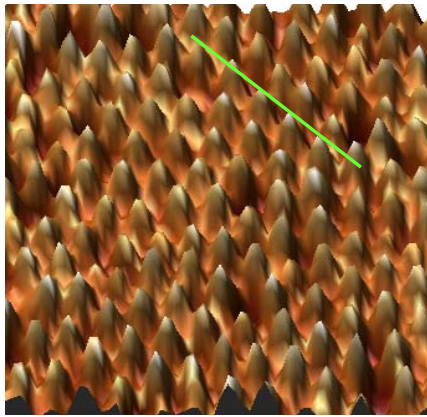
At large current density (Fig. 4.2.5e-f) no periodicity is observed in the arrangement of cobalt in the aluminum oxide. Large and small size cobalt particles are dispersed in a disordered fashion on the aluminum oxide. This is due to the fast deposition rate that occurs at high current density. Furthermore, many small nanorods could have overlapped out of the pore (as shown in the model of Fig. 4.2.4c) when the quantity of material was larger.

From the following study, it can be deduced that the samples prepared with a current density less than 7.5 mA/cm^2 (Fig. 4.2.5a-c) are relatively ordered. It was shown in the previous section that the current density of 1 mA/cm^2 and a deposition charge of 0.904 C lead to the formation of well ordered nanorods in the pores of alumina membrane. The combination of these two conditions may give structures with a very good arrangement of particles.

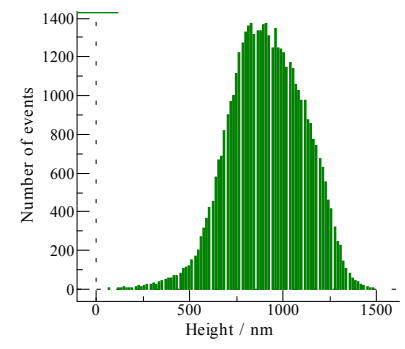
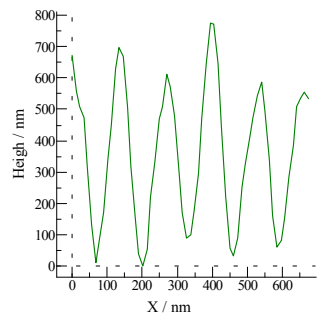
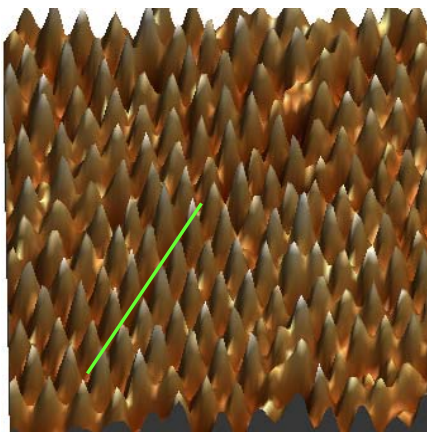
- Constant charge electrochemical deposition at different current density

The current density was changed and the deposition time adjusted so that the quantity of electricity ($Q = It$) should be the same. The constant charge used in this study was 0.904 C ; the following results were obtained.

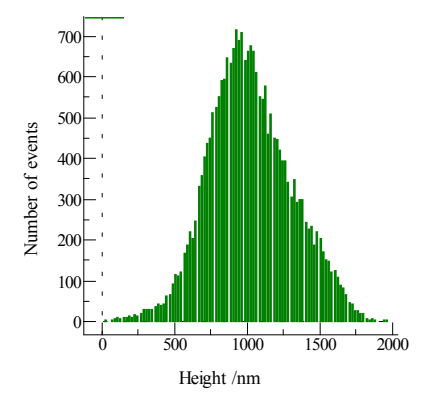
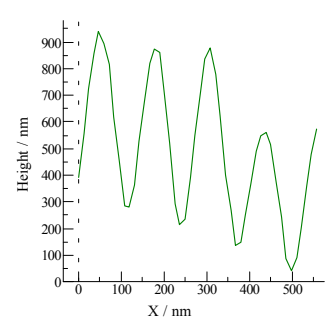
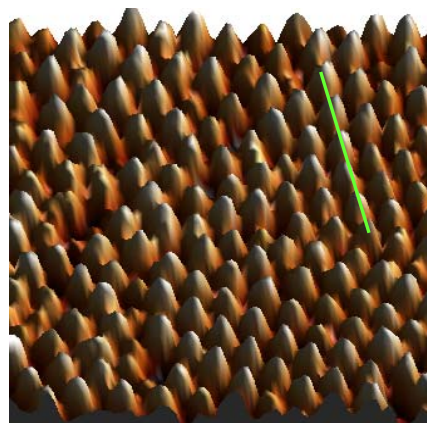




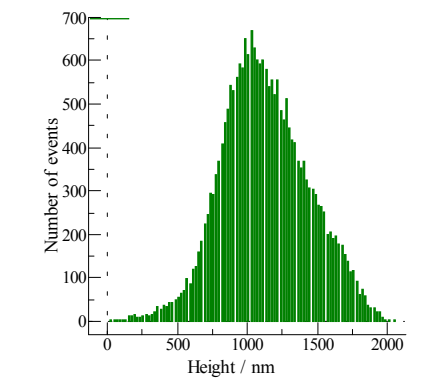
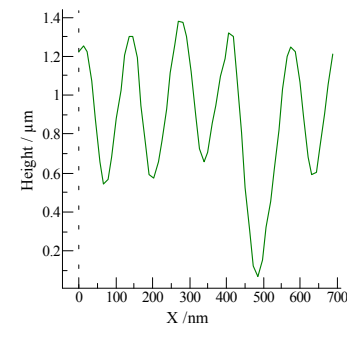
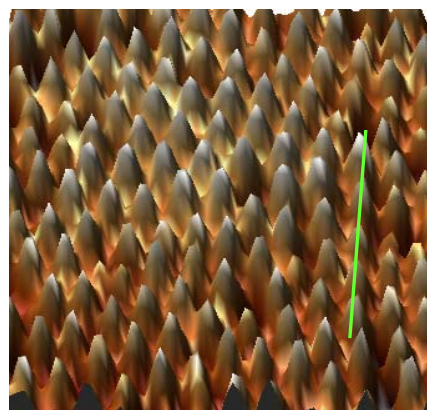
b



c



d



e

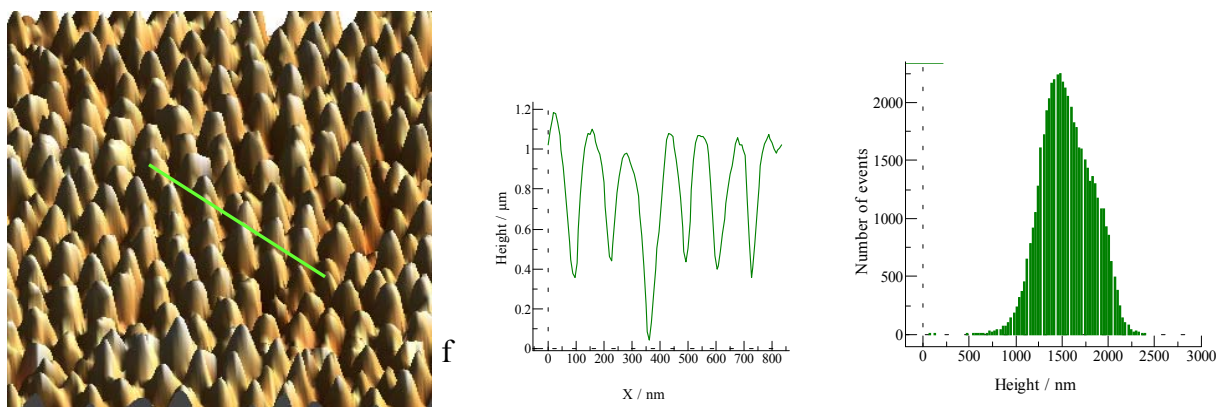


Fig. 4.2.6. Structures ($1.6 \times 1.6 \mu\text{m}^2$) of samples prepared at various current densities with a charge of 0.904 C: (a) 1; (b) 2.5; (c) 5; (d) 7.5; (e) 10; (f) 12.5 mA/cm^2 . Each picture is followed by the profile along one line and the histogram of fibers distribution; the histograms were generated from $5 \times 5 \mu\text{m}^2$ scales to show the distribution of particle in large scale area.

The surface topography is very uniform when the Cobalt nanorods are deposited within the pores of thin AAO membrane with constant quantity of electricity of 0.904 C. Without dissolving the AAO template (since it is very thin), cobalt fibers of about 800 nm (a-d) to $1.5 \mu\text{m}$ (e, f) height stands straight out of the $\text{Al}_2\text{O}_3 / \text{Al}$ foil. This particular construction of well-ordered fibers out of the AAO is due to the accurate control of both current density and deposition charge. Since the pictures show only one part of the structure, the histogram of size distribution was carried out in large-scale area. It shows the numbers of fibers with a specific height and indicates that the regular arrangement of fibers is extended to at least $5 \times 5 \mu\text{m}^2$.

The diameter of the fibers at mid-height is about 60 nm; the value is in the same range as the pore diameter of the AAO membrane. The periodicity (center- to- center spacing between two neighboring fibers) determined by both line measurement analysis and 2D Fourier transform is about 125 nm.

The thickness of the AAO was about 55 nm, but on the profile carried in Fig. 4.2.6, the under layer looks to be greater than the real value. In the first point of view, this indicates that the fibers may be linked together at the base by a thin layer of cobalt. This hypothesis shows that a conically continuous film was prepared rather than single fiber. Secondly, we may assume that the small (diameter =10 nm) AFM tip cannot go deeper in the hole between the fibers to give better resolution of the bottom. This second hypothesis seems to be true because the under layer is more important in thick sample (e and f).

The variation of the surface roughness of the samples with the current density at constant and various deposition charges are summarized on the following graph.

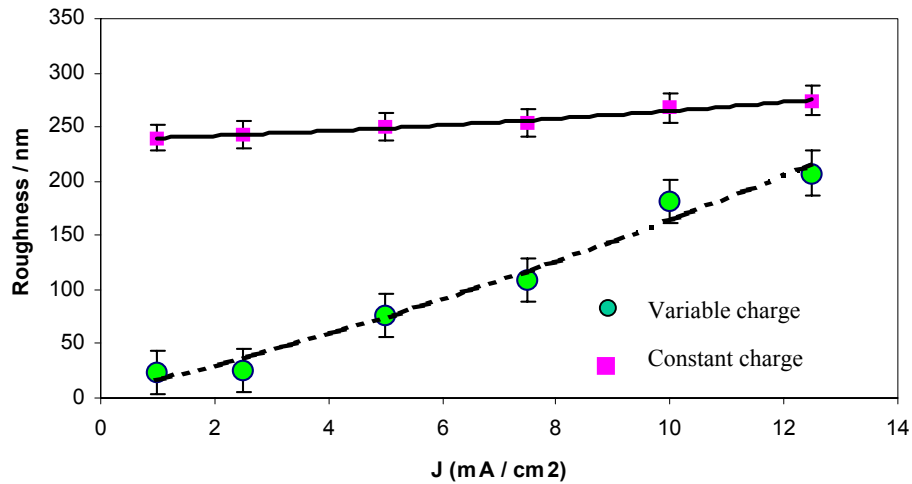


Fig. 4.2.7. Variation of the roughness factor of the sample with the current density.

When the quantity of electricity varies, the surface roughness increases with the current density; this indicates how far the surface deviate from the horizontal smooth surface. The variation is less pronounced with the samples prepared at constant charge since the quantity of material deposited is the same. In all cases the roughness factor increases with the current density in accordance with Marozzi and Chialvo [95,96] who reported that the surface roughness is a linear function of the deposition current density. The electrochemical deposition of particle within the pore of alumina membrane follows the same principle. Of course, an increase of the surface roughness is most beneficial for electrocatalysis when the whole surface is accessible to reactants [97].

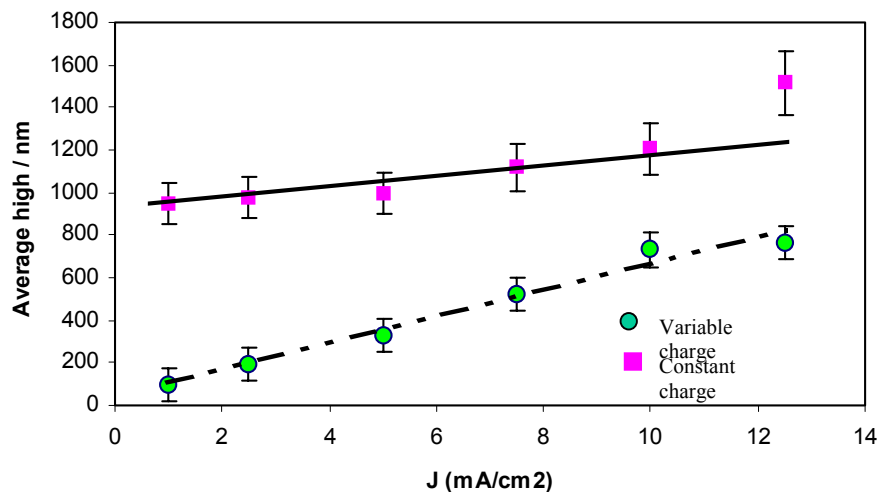


Fig. 4.2.8 Variation of the average height of the samples the current density

The average height is also a linear function of the current density. This accounts for the increase of the quantity of the material deposited per unit area according to the Faraday law. The linear dependence of the thickness on the current density (in the case of variable quantity of electricity) follows the same idea. The small deviation observed at high current density (in the case of constant Q) can be attributed to the kinetics of deposition. Samples prepared at constant charge should normally have the same thickness; the variation of this parameter may be due to the change of the deposition rate when the current density is varied. At higher current density, particles may have grown faster and preferentially along the z-axis; this may account for the relatively high values of thickness observed in those cases. As mentioned in the previous section, this may also come from the non uniformity of the surface at each point or from experimental error.

From the following study on the influence of the current density, it can be noticed that significant change occur on the structure when the current density and the quantity of electricity are varied at the same time. The change of the topography of cobalt nanomaterial with the current density will be negligible if the quantity of electricity consumed during the electrodeposition is constant. Cobalt nanorods of about 800 nm to 1.5 μ m height are successfully prepared in the thin AAO film by direct current electrodeposition without any dissolution of the template. According to Jinxia et al.[98], single crystalline nanomaterials are obtained with direct current deposition while pulse and alternative currents give polycrystalline nanomaterial.

The outgrow of the deposit above the pore of alumina could be interpreted as the consequence of high current density, short deposition time and the small thickness of the alumina membrane. These allow particles to grow faster along the z-axis. Moreover, the surface could be formed of conically nanostructured film rather than single nanorods; this is possible since AFM cannot give information about the bottom of the deposit. It was also observed that the particles collapsed when the quantity of electricity was high enough, and no memory of the porous structure was kept outside the pores.

4.2.3 Electrochemical impedance characterization of ordered cobalt nanofilm on AAO.

Samples were prepared in the conditions of figure 4.2.6. EIS measurements were performed in order to evaluate the electrical properties of the cobalt nanomaterial. The impedance technique is very sensitive to defect dimension; drilling small defects of about 150 μ m or less results to

impedance values in the order of some dozens of $M\Omega\text{ cm}^{-2}$ at low frequencies [99]. The Nyquist representation of impedance data of films deposited with the same quantities of electricity are shown on Fig. 4.2.9.

The impedance spectra were recorded in 0.4M LiClO_4 with 5 mV ac amplitude of sinusoidal voltage in the frequency range from 100 kHz to 5 Hz. The DC potential of -0.5 V was chosen to maintain the electrode in steady state conditions and avoid any oxidation of the particles that may occur at potential greater than -0.25 V .

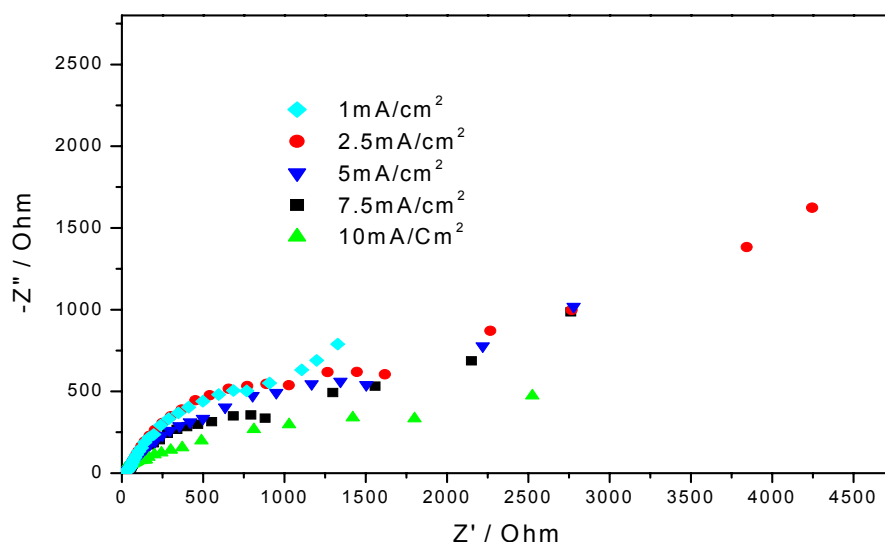


Fig. 4.2.9. Nyquist representation of impedance data of cobalt nanorods deposited from aqueous solution into the AAO.

The Nyquist-like diagram of the samples is characteristic of electrode process under kinetic and charge transfer control. In the present case, the diffusion process is linear and semi-infinite type. The dissolved oxygen diffuses from solution to the electrode surface. The line at low frequency may also be due to the solid-state diffusion of Lithium ions within the electrode material. In general, this type of Nyquist diagram is characteristic of porous electrode. At critical frequency, the excitation signal reaches the bottom of the pore and the entire surface area of the electrode is sensed. Further lowering of frequency results in an increase of impedance; that is characteristic of purely capacitive interface. This results in a vertical line in complex plane representation of ideal porous electrode [68]. Depending on the roughness or inhomogeneity of the electrode, this line can deviate from its ideal vertical position [100]. The deviation from the ideal porous electrode diagram may also be due to the pore geometry of the

samples; the pores are opened and not cylindrical or hexagonal like that studied by other authors [101].

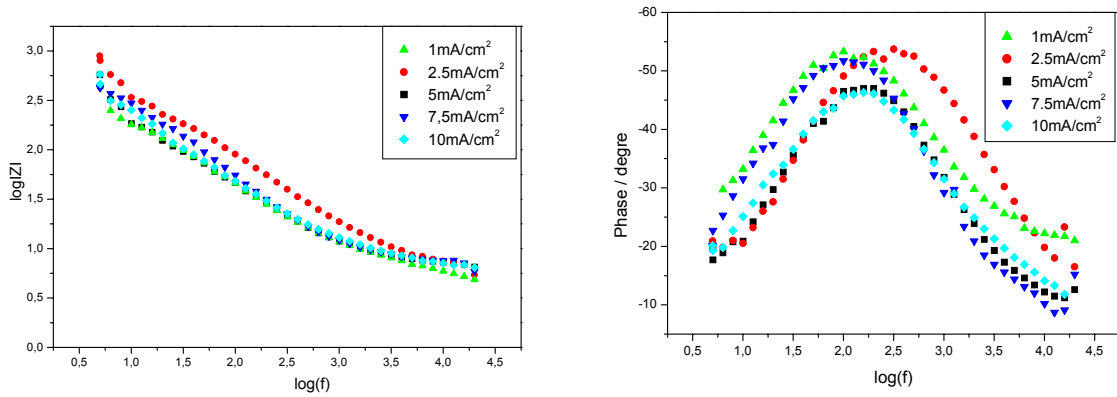
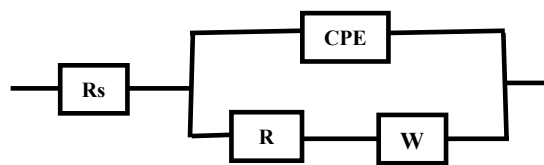


Fig. 4.2.10. Bode magnitude and phase of cobalt nanorods deposited from aqueous solution.

In general, the magnitude of impedance decreases with increasing frequency. The curve with lower values of impedance magnitude corresponds to the sample that has the higher specific area. Similarly, samples with high impedance magnitude have smaller specific area. It can be observed that the difference in the surface area of the samples is not large since the curves are nearly superimposed. The impedance magnitude in these samples is very small compared to that of the porous alumina membrane. That is caused by the introduction of metallic particles in the pore of AAO, and by the high specific surface area of the film of cobalt nanomaterial. The impedance data were fitted with the following equivalent circuit.



$$Z(j\omega) = R_s + \frac{R_p \sqrt{\omega} + \sigma e^{-j\frac{\pi}{4}}}{A\omega^\alpha e^{j\alpha\frac{\pi}{2}} \left[R_p \sqrt{\omega} + \sigma e^{-j\frac{\pi}{4}} \right] + \sqrt{\omega}} \quad (22)$$

See Appendix for the calculation of equation (22). The double layer capacitance is represented in the model by the constant phase element (CPE); it is more appropriate for porous and rough samples. The Warburg element (W) accounts for the diffusion in the pore. R_p is the polarization

resistance; it can also represent the corrosion resistance if we are interested in corrosion of cobalt nanofilm in LiClO_4 . In this case, the film will have better resistance to corrosion when the R_p is high.

Tab. 4.2.1 Impedance data of cobalt nanorods deposited from aqueous solution

J [mA/cm ²]		1	2.5	5	7.5	10
CPE	A [F cm ⁻² s ^{α-1}]	2.35×10^{-5}	1.83×10^{-5}	1.08×10^{-5}	6.4×10^{-5}	2.77×10^{-5}
	α ($0 \leq \alpha \leq 1$)	0.89	0.96	0.80	0.81	0.87
R_p [Ω cm ⁻²]		10875	10795	10680	11530	10235
R_s [Ω]		26.07	38.42	31.72	36.54	32.92
W / σ [$\Omega / \text{s}^{1/2}$]		1.16×10^{-4}	8.82×10^{-4}	5.322×10^{-4}	5.591×10^{-4}	2.07×10^{-4}

The values of R_p decrease slowly with the current density; that is in opposite to the variation of the thickness of the sample. It can be suggested that the polarization resistance decreases when the quantity of material on the surface increases. The presence of more metallic particles increases the conductivity of the electrode and lowers the polarization resistance. That is true since the values of R_p in the case of cobalt film are very small compared to that of porous aluminum membrane (Tab. 4.1.1). The films have lower corrosion resistance than the AAO. Moreover, the value of the constant phase exponent is in all cases greater than 0.7, the double layer is close to the ideal capacitor.

As summary, EIS confirmed the porous nature of cobalt nanomaterials deposited within the pore of AAO. Many parameters were deduced from impedance data: the Warburg constant that contains the diffusion coefficient of lithium ions or diluted oxygen within the pores of the porous film, the polarization resistances and the values of the constant phase coefficient.

4.2.4 Discussion of the impedance results

The EIS technique provides very detailed data on a localized basis that can be used to distinguish the topography of the electrode surface. The Nyquist representation of the impedance data of porous aluminum oxide are different from those of the same membranes filled with cobalt particles. EIS is sensitive to the change of surface properties caused by the introduction of metal particles.

A semicircle is generally observed in the complex-plane representation of the EIS data of AAO membrane anodized at low temperature (Fig. 4. 1.5). The electrode process is characteristic of charge transfer mechanism. The membrane is highly porous and we may expect a frequency response characteristic of porous electrode as predicted by the transmission line model. This is not the case because a thin aluminum oxide barrier layer exists at the bottom of the pores. The high impedance magnitude of alumina/aluminum electrode is also caused by the same barrier layer. The dominant effect is the transfer of electrons across this layer.

In the electrodeposition process, the under barrier layer of the AAO is broken and the pores are filled with metallic particles. This increases the conductivity of the surface; the consequence is the reduction of the impedance magnitude to a factor more than 15 from Fig. 4.1.5 to 4.2.9; i.e the values of the real and imaginary part of the impedance are more than 15 time lower in Fig 4.2.9 than in Fig. 4.1.5.

4.2.5 Electrochemical deposition of single nanorod and clusters in the pore of AAO.

Recently, investigations have been focused on confined systems with micrometer and nanometer dimensions. Due to their restricted size, these structures exhibit novel physical and chemical properties, and have opened up a new field of research and applications [102]. Nanometric single particles are currently considered as functional building blocks in single-electron devices and nanoelectronics [103]. The emission from single dot has the form of a very sharp line similar to that observed from an atom [104]. Therefore, the electrochemical study of single nanoparticle and clusters could be of basic interest.

The electrochemical systems used for deposition consists of a potentiostat / galvanostat 237 and a piezoelectric micropositioners that allow the regulation of the distance between the tip (platinum wire counter electrode of about 0.002 cm^2 diameter; this should not be assigned to STM or AFM tip) and the working electrode. Single fibers and clusters were deposited galvanostatically from aqueous solution within the pores of alumina membrane. The distance between the electrodes was fixed at about 1mm and a current of $0.79 \text{ }\mu\text{A}$ passed between the electrodes. The tip can be translated on the working electrode with the help of the micropositioners. The AFM analysis of the samples revealed the follow structures.

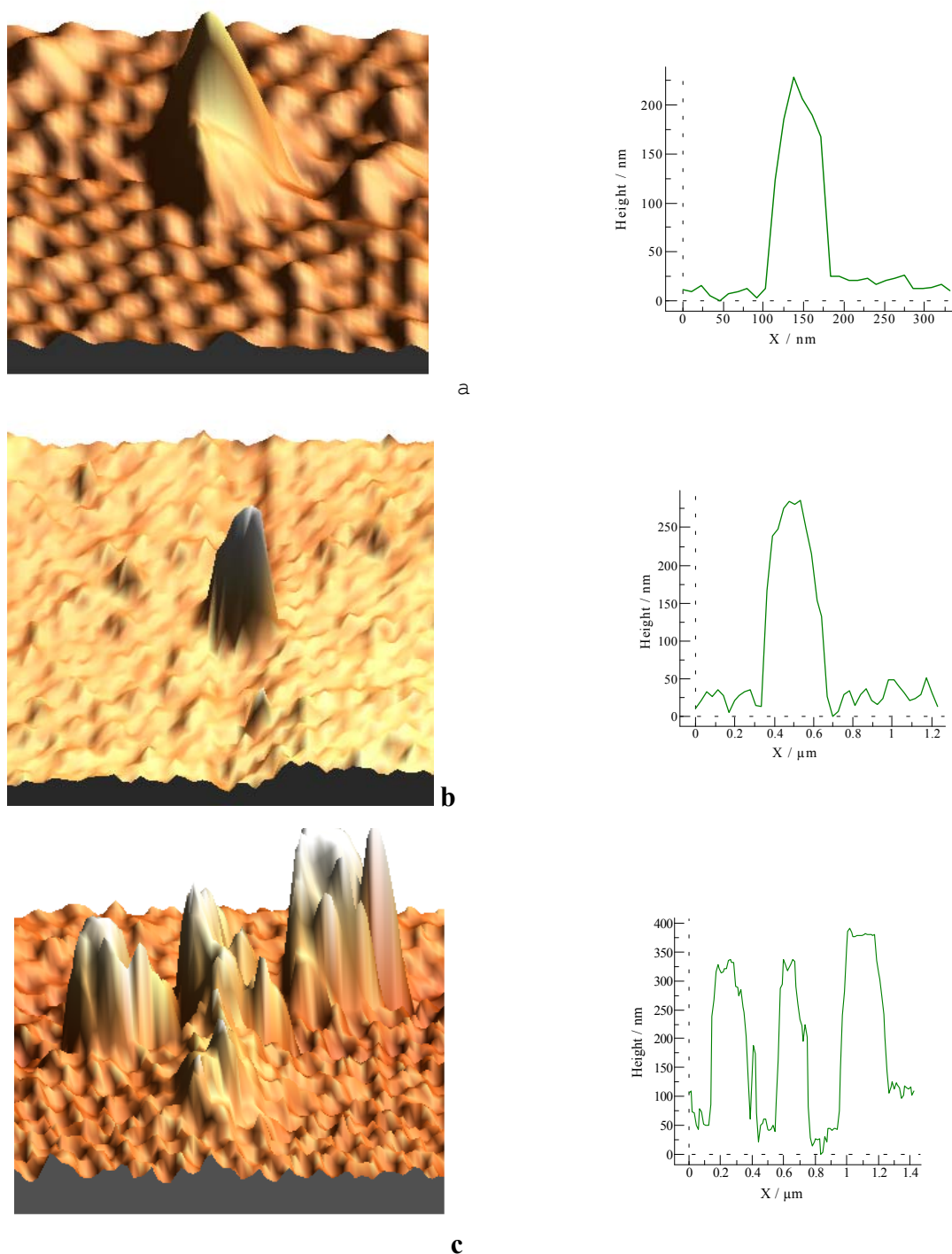


Fig. 4.2.11. AFM micrograph of single cobalt nanorods and clusters deposited within the AAO membrane.

Very small single nanorods of about 200 nm in diameter and 250 (a) or 300 nm (b) in height are shown on Fig. 4.2.11. Cobalt nanoclusters (c) obtained by moving the tip on the surface of the working electrode are represented on the same figure. The initial idea was to make one line constituted of single fibers by translating the tip on the electrode. Since the diameter of the tip is

not small enough, particles formed during a small translation of the tip collapse. Moreover, the AFM measurement was not carried out in situ; therefore, increasing the translation distance of the tip (Counter electrode of the micropositionner, which is difference from the AFM tip) gives fibers with periodicity far enough to be observed in the AFM scan range of 24 μm . Therefore it was difficult to construct and to visualize a series of three, four or more aligned single particles. Such experiment could be succesfull in-situ using STM or a scanning electrochemical microscope, SECM.

4.3 Deposition of Cobalt in the AAO membrane using the hexagonal phase of lyotropic liquid crystal: Double template electrodeposition.

Surfactant have often been reported as component of electroplating nanomaterial; but nothing is known about how the electrodeposition process variables and the combination with other template might affect the structure and properties of films. In this part we extend the application of liquid crystal template by combination with aluminum oxide membrane to produce mesoporous cobalt. The structures of cobalt films deposited by double template technique using direct and pulse current will be compared. The influence of the current density on the structures will be examined. The objective is to reduce the size of the particles and increase the specific area of the material. The surface-to-volume ratio is very high in nanoparticles, and surface effects play an important role on the physical properties of the film [105]. For example, to increase the storage density of semiconductor memories, the size of each memory cell must be reduced. A smaller memory cell leads to faster speeds, lower power consumption and low signal-to-noise ratio [106, 107].

4.3.1 Preparation and characterization of the liquid crystal mixtures

The plating media used is a binary system containing oxyethylene surfactant and aqueous solution. The solution contained 0.5 mol/l cobalt sulfate, 5.6×10^{-3} mol/l ascorbic acid and 0.3 mol/l boric acid. The composition (see experimental) was chosen according to the phase diagram (see appendix) of the Brij78 described in [57]. The phase of Brij 78 was found to be less sensitive to the addition of aqueous solution containing metal ions; the hexagonal domain is obtained with 52 to 80 wt % Brij 78 and is stable in a temperature range from 20 to 85 °C [57]. The solution has paste-like consistency at room temperature. The addition of the aqueous solution containing ions to the melted surfactant leads to a significant and immediate change of its melting point. The melting point of the mixture is greater than that of the pure surfactant.

Small-angle x-ray scattering (SAXS) was used to characterize the phase. Two basic regions of the diffraction pattern are used to identify the phase. The low angle region identifies the symmetry and long-range organization of the phase, whereas the wide-angle region gives information on molecular packing or short-range organization of the phase [39]. The SAXS spectra of the cobalt plating mixtures are shown on Fig. 4.3.1. The long range ordering of aggregates onto three dimensional lattices gives rise to Bragg reflections whose reciprocal

spacing ($S_{hkl} = 1/d_{hkl}$) are in the characteristic ratio of 1: $\sqrt{3}$: 2: $\sqrt{7}$...in the case of hexagonal system [39, 108].

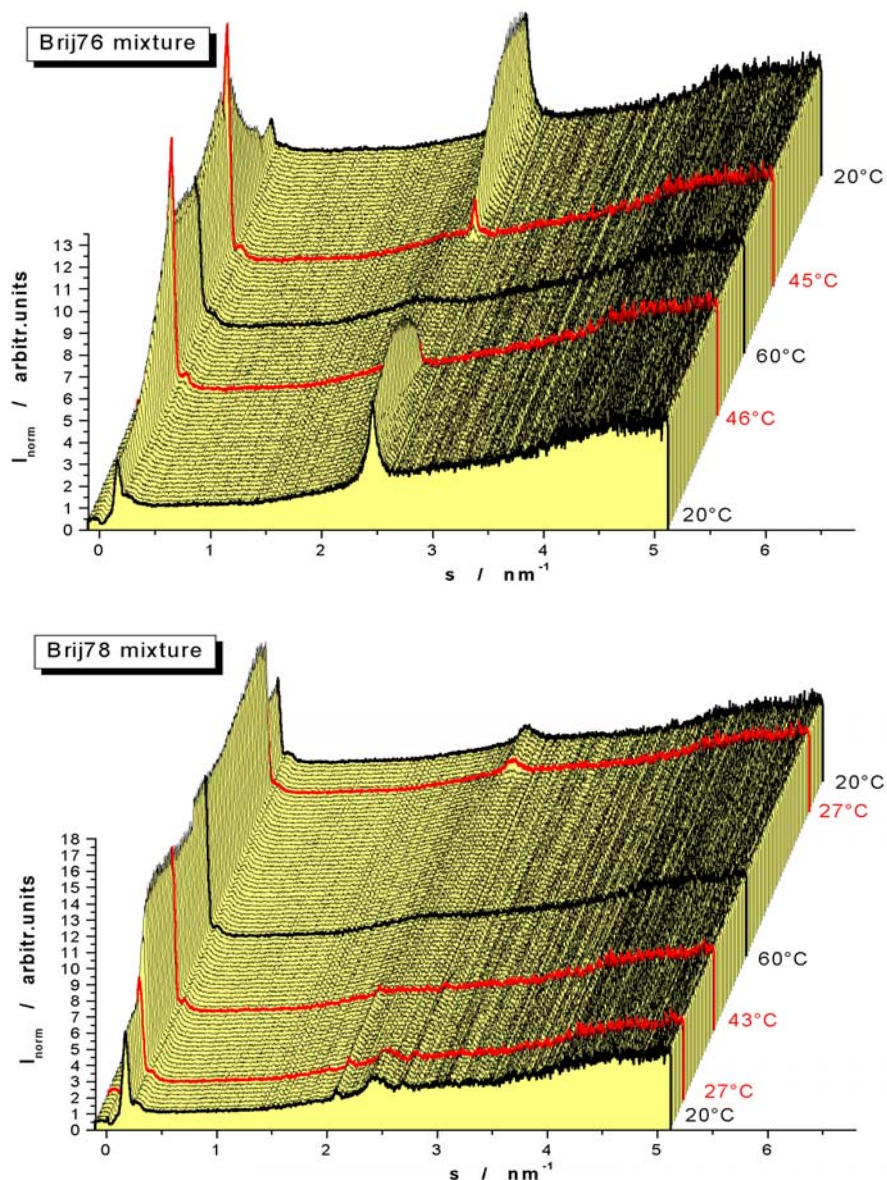


Fig. 4.3.1. SAXS spectra of Brij 76 and Brij 78 lyotropic system. The aqueous solution used for the mixture contains 0.5 mol/l cobalt sulfate, 5.6×10^{-3} mol/l ascorbic acid and 0.3 mol/l boric acid. The phase composition is 60 wt% of Brij 76 or 65 wt% of Brij 78 respectively; the other fractions correspond to the aqueous phase weight percentage.

The low angle regions ($S_{hkl} < 2 \text{ nm}^{-1}$) of both spectra show two peaks with S_{hkl} -spacing 0.126 and 0.239 nm^{-1} , the decomposition of the SAXS signal shows another small peak at $S_{hkl} 0.313 \text{ nm}^{-1}$. The S values of the three signals are approximately in the ratio 1: $\sqrt{3}$: 2 that corresponds

to the diffraction planes of the hexagonal structure with d-spacing of 7.98, 4.18 and 3.19 nm respectively. Whitehead et al. reported a d-value of 8.2 nm for the first reflexion of the hexagonal mixture of Brij 78 of similar composition [59].

The low resolution of the signal at 0.239 and 0.313 nm^{-1} is due to the large d spacing. To scan such peaks with good resolution, a camera design operating in vacuum or with helium should be used to eliminate air scattering [39].

In the wide-angle region ($2 < S_{\text{hkl}} < 3 \text{ nm}^{-1}$) a sharp peak with d-spacing 4 \AA is observed in the case of Brij 76 mixture at temperature between 20 and 46°C . It accounts for strong interaction and the greater correlation in the mutual position of molecules in the aggregates. A similar signal with low intensity appears on the Brij 78 mixture. Below the melting point, the molecules have fix positions in the columns. When the temperature increases up to the melting point, the molecule have free motion in the columns; such motion is characteristic of liquid and gas state of the material. This accounts for the extinction of the wide-angle signal at higher temperature.

In general, the three signals at low angle didn't change significantly with temperature; therefore both mixtures remain in the hexagonal phase at this temperature range. But at low temperatures (20 - 46°C), the samples are in ordered columnar phase (col_{ho}) with constant periodicity between molecules while at $T > 46^\circ\text{C}$, the arrangement of molecules in each column is disordered (col_{hd}). The hexagonal behavior of Brij 78 in temperature range between 20 and 60°C is in accordance with the phase diagram of a similar mixture reported by Nelson and coworkers [57].

4.3.2 Principle of double template deposition

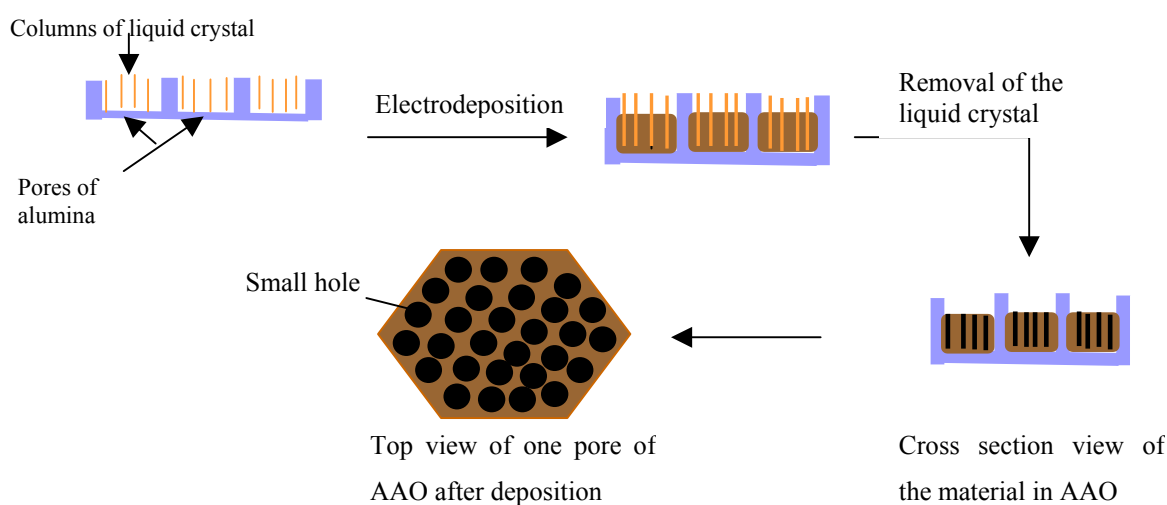


Fig. 4.3.2. Illustration of the principle of double template electrochemical deposition.

A double template deposition is a combination of two moulds for the electrochemical preparation of nanomaterial. In the present case, the porous alumina membrane and the hexagonal phase of liquid crystal are combined together. The idea is to prepare highly porous and ordered nanomaterial. Since the pore of the alumina membrane is about 7 times larger than the diameter of the columns of liquid crystal, we expected that many columns of surfactant could penetrate in one pore of alumina. After deposition and removal of the columns, the material prepared from the bottom of the pore of alumina will present many pores. The alumina membrane will orient the particles; therefore a nanofilm prepared in such conditions could be highly porous with two repeat distances; one due to the inter pore separation of the alumina membrane and the other caused by the liquid crystal columns as shown on Fig. 4.3.2.

4.3.3 Double template electrochemical deposition of cobalt

Electrochemical experiments were conducted with a cell consisting of a lab made Ag/AgCl, KCl_{sat} reference electrode ($E^\circ \sim 0.177V$ vs SHE), an alumina / aluminum working electrode and a platinum counter electrode. The hexagonal phase of surfactant is viscous at room temperature. The conditions that need to be addressed when developing new template synthetic method include the following: the precursor solution used to prepare the material should wet the pore or the surface of the electrode. The membrane or the phase should be stable thermally and chemically with respect to the reaction conditions [24]. To satisfy those conditions, the H₁-phase was melted during electrodeposition by heating the cell with a thermoelectric (Peltier element) module. The electrochemical cell and the thermoelectric module were mounted together with a micropositioner that helps to adjust the distance between the working and the counter electrode. Since the conductivity of the surfactant-alumina is low when they are mixed together, the distance between the working and counter electrode was fixed between 1.5 and 2 mm by the micro machine.

- Direct current electrochemical deposition

All samples were prepared at 55°C with a current density of 0.50 mA/cm². The deposition time was varied in order to have correlation between the quantity of electricity and the properties of the film. Since the structure of the nanofilms prepared from Brij 78 and Brij 76 with direct current was similar, only one case will be showed. The following pictures represent the AFM micrographs of the samples obtained from Brij 78 mixture.

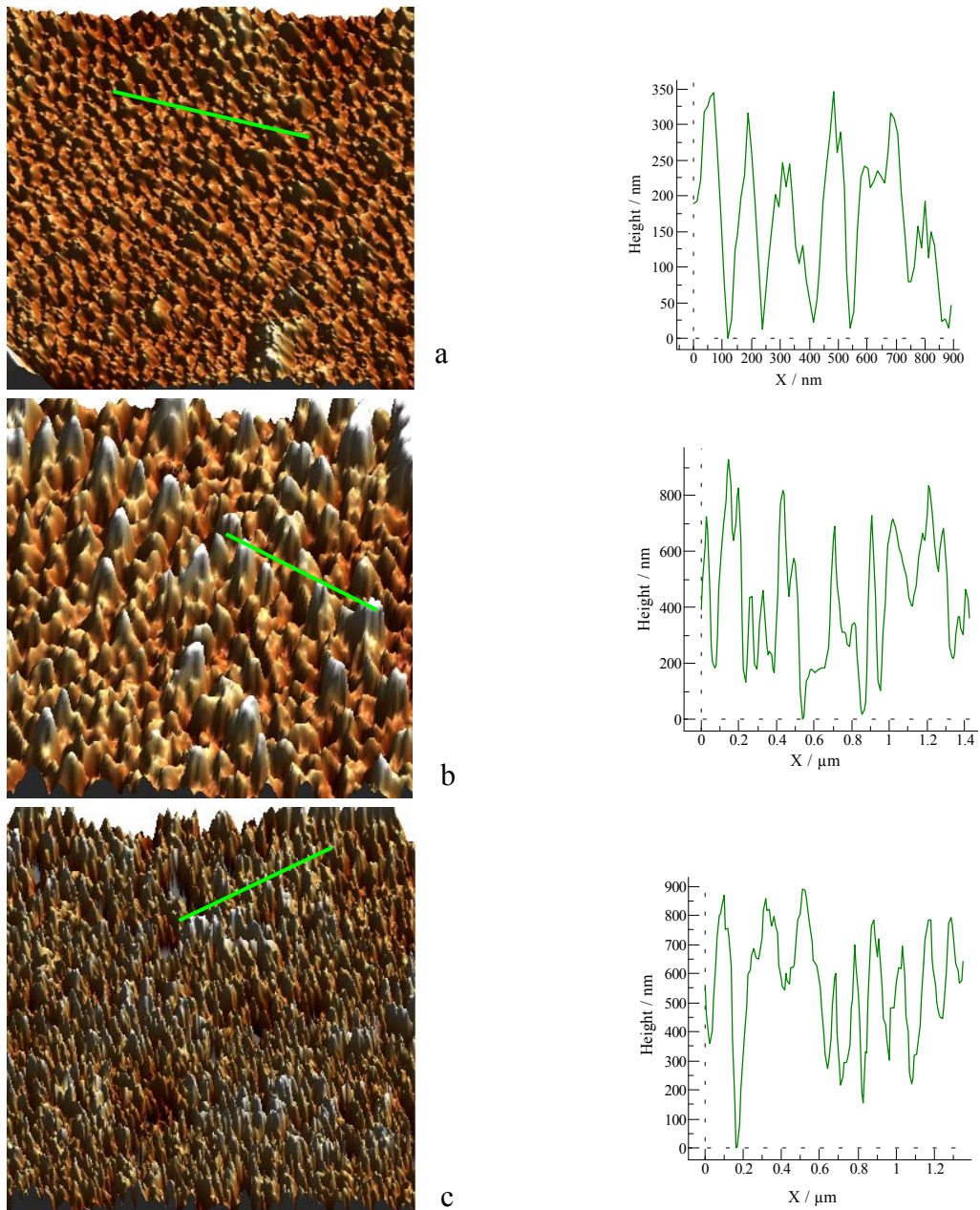


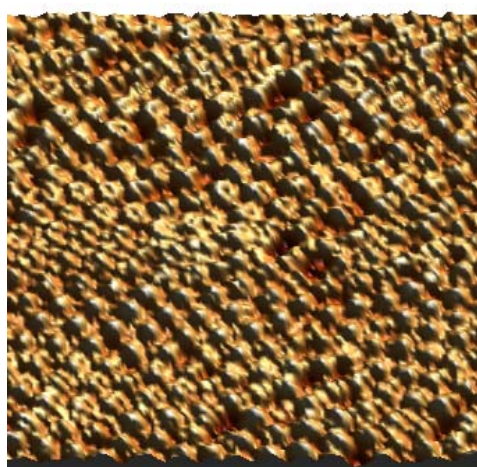
Fig. 4.3.3. Structures of samples prepared at different quantity of electricity: (a) 0.24; (b) 0.95; (c) 1.18 Coulomb. The picture is followed by the profile along one line. Each picture is $1.6 \times 1.6 \mu\text{m}^2$.

We note that the AFM micrograph doesn't show direct evidence of the hexagonal nanostructure. Particles that grow from the bottom of the pore of AAO are not regularly separated like in the material deposited from aqueous solution. However the mesoporosity of the cobalt nanomaterial produced from Brij 78 is well observed. The absence of long-range continuity or hexagonal nanostructure may be due to the inhomogeneity and imperfect alignment of the hexagonal columns in the plating mixture (liquid crystal). It may also be due

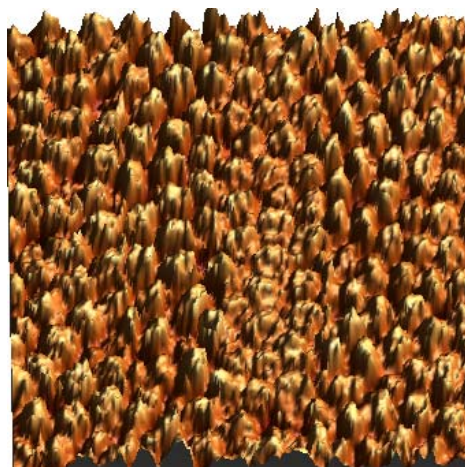
to the deposition temperature. Increasing the temperature during deposition was found to increase the repeat distance and the roughness factor of the deposit prepared from liquid crystal [54]. At 55°C the plating mixture is in liquid state; the interaction between surfactant molecules is lower compared to a solid sample (as shown by the SAXS of the mixture); this allows free motion of the surfactant molecules and columns. It may account for the absence of ordering on the structure of the deposit. On the other hand, the hexagonal pattern due to surfactant columns may not appear clearly in the AFM scale. Bartlett and co-workers [60] reported that the hexagonal arrangement of particles deposited from liquid crystal on polished gold electrode was not visible on the scale of the SEM, the hexagonal pattern of the structure was found only with TEM. Therefore ordered hexagonal array of uniform channels could be seen if the samples are analyzed by high resolution TEM.

- Pulse current electrochemical deposition

Cobalt was deposited at constant pulse current density of 2.5 mA/cm² with $t_{\text{on}} = 0.3$ s and $t_{\text{off}} = 0.1$ s; values that correspond to a pause-to-pulse ratio ($t_{\text{off}}/t_{\text{on}}$) of 1/3. The total charge used for the deposit was varied from one sample to other. It is established that pulse current density has a beneficial effect on the properties of deposits. Pulse electrodeposition yields finer-grained and more homogeneous surface appearance of the deposit because of higher instantaneous current that increases the nucleation rate [109]. Moreover, pulse current is reliable for the deposition into high aspect material (AAO) and can compensate for the slow diffusion-driven transport in the pores of AAO. The following result was obtained with Brij 78 mixture.



a



b

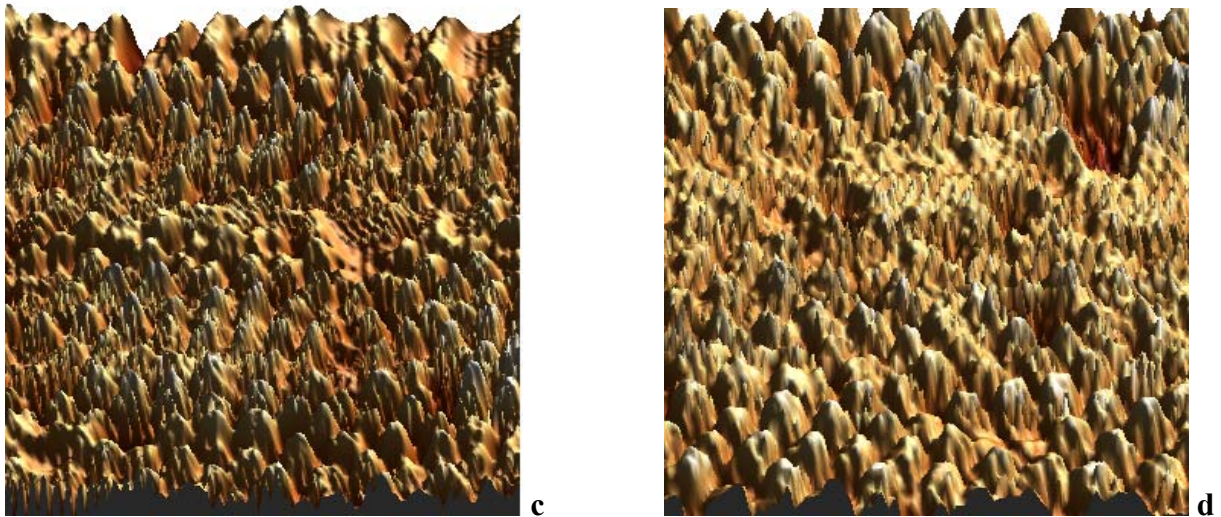


Fig. 4.3.4. AFM micrographs ($1.6 \times 1.6 \mu\text{m}^2$) of cobalt mesoporous films prepared by double template and pulse current. The deposition charges are: (a) 0.488, (b) 0.576, (c) 1.029, (d) 1.106 C. $j = 2.5 \text{ mA}/\text{cm}^2$, $t_{\text{on}}/t_{\text{off}} = 1/3$.

Fig. 4.3.4 represents the direct topography of cobalt nanofilm deposited by double template and pulse current techniques. On each image, direct observation of the hexagonal channels caused by the AAO is possible. The surfaces have small substructure caused by the columns of liquid crystal; fibers that grow from the bottom to the top of the AAO membrane have many subdivisions. Since the films prepared from aqueous solution in identical conditions (by pulse current) show no evidence of substructures and considering the results of the DC deposition; it appears that the double substructures are caused by the combination of both pulse current and liquid crystal. In the hexagonal phase of liquid crystal, the periodic orientation of the surfactant aggregate provides the mould in which material is deposited [57].

The periodicity (center-to-center spacing of two consecutive fibers) determined by 2D Fourier transform is about 85 nm. This value is less than that of the nanocobalt deposited from aqueous solution within the AAO membrane, which was about 125 nm. The reduction of the periodicity in this last case is due to the subdivisions of the particles.

The combination of pulse and liquid crystal bring significant change on the structure of cobalt nanomaterial. To obtain more information about the structure of this material a small part of some sample was zoomed-in and scanned. The micrographs in Fig. 4.3.5 represent the small-scale structure of cobalt nanomaterials prepared by double template technique.

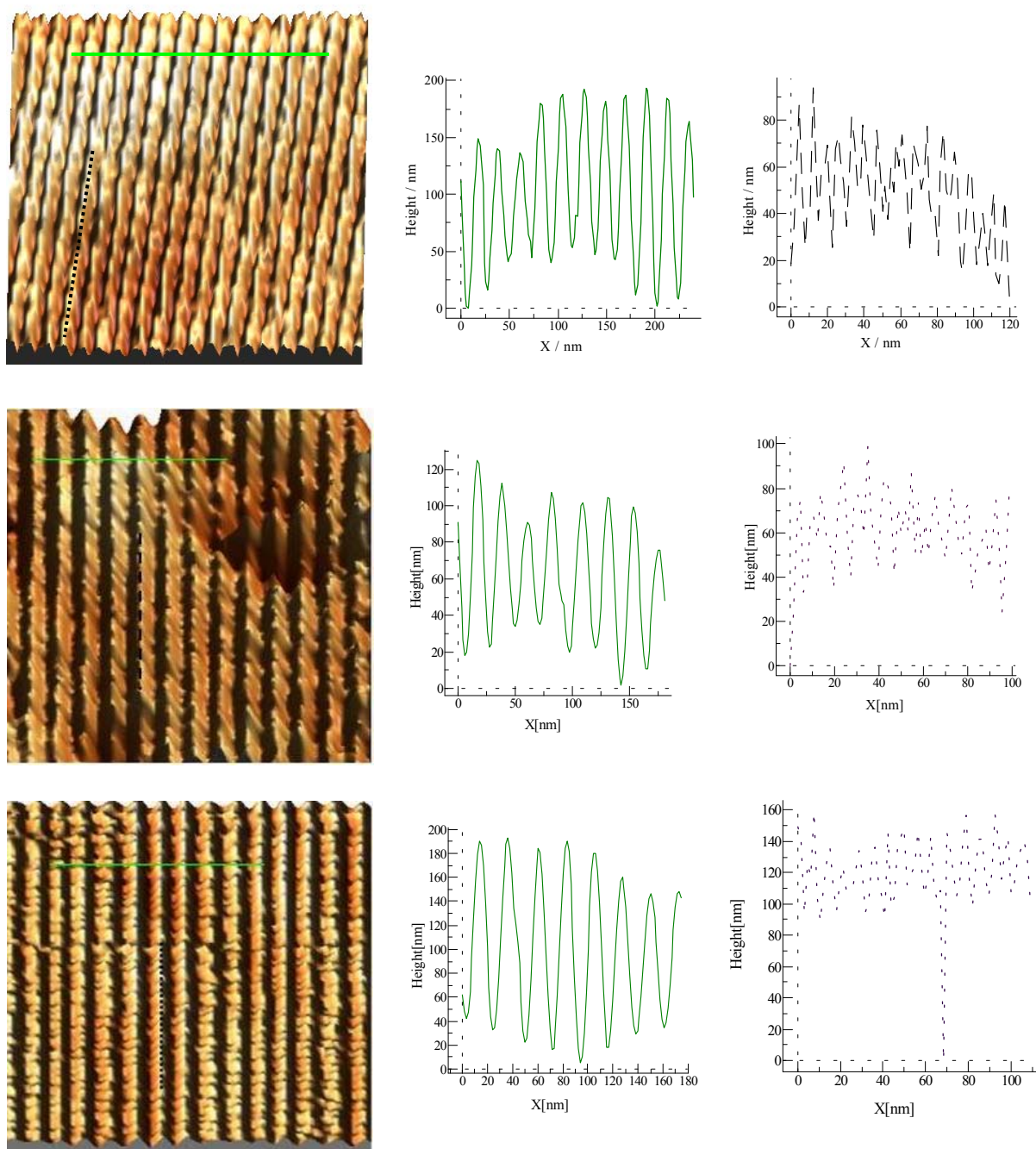


Fig. 4.3.5. Small-scale structure ($350 \times 350 \text{ nm}^2$) obtained from double template deposition: (a), (b) and (c) come from samples of Fig. 3.3.4 b, c and d respectively.

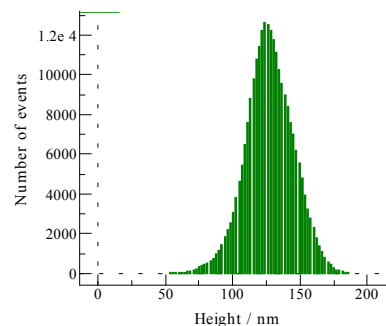
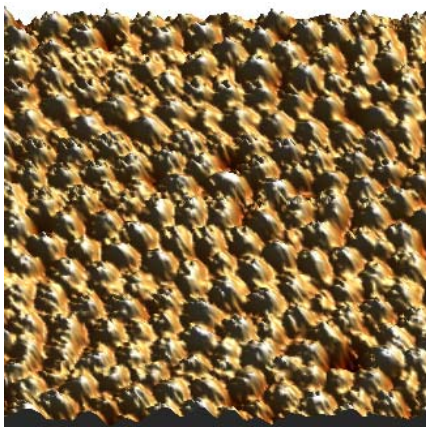
In all cases, the material has parallel arrangement on the surface of the electrode. From the profile carried in the direction perpendicular and parallel to the line of cobalt, it is observed that this material is made of very small cobalt particles with specific orientation. The columns of liquid crystal orient these particles. The structure gives an idea on the orientation of the columns of surfactant; the axes of the columns may be parallel to the plane of the electrode and

not perpendicular as expected. The lower part (valley) of the structures represents the free spaces that were occupied by the columns of surfactant. In the direction perpendicular to the line, the distance between the centers of two consecutive lines is about 20 nm. Since the first neighbor distance is about two times the distance of the free space between the lines, the diameter of the valley is about 10 nm; this value is close to the diameter of the columns of liquid crystal which is about 7.93 nm (from the SAXS spectrum). The difference between the values is due to the instrumental error since the AFM tip of 10 nm in diameter cannot measure such distance accurately.

The significant change on the structures may come from the variation in the orientation of columns of liquid crystal. The instantaneous current could polarize the surfactant aggregate and induce a preferential orientation of the columns. Even copolymers consisting of polymers with a very small polarisability can be aligned using electric fields [104]. A change on the orientation of liquid crystal (known as Freedericksz transition) due to the competition between the surface and the electric or magnetic field of sufficient strength was reported [110]. The orientation of the columns in the present case is possible since the plating mixture is in liquid state (low intermolecular interaction) with the possibility of free motion.

• Deposition from Brij 76 mixture with pulse current.

In order to check the reproducibility of the double substructures with other mixture and to confirm the validity of the method, cobalt films were prepared in the same working station using Brij 76 mixture and pulse current. The quantity of electricity was varied and the structures of cobalt nanofilms determined by AFM are show as follow.



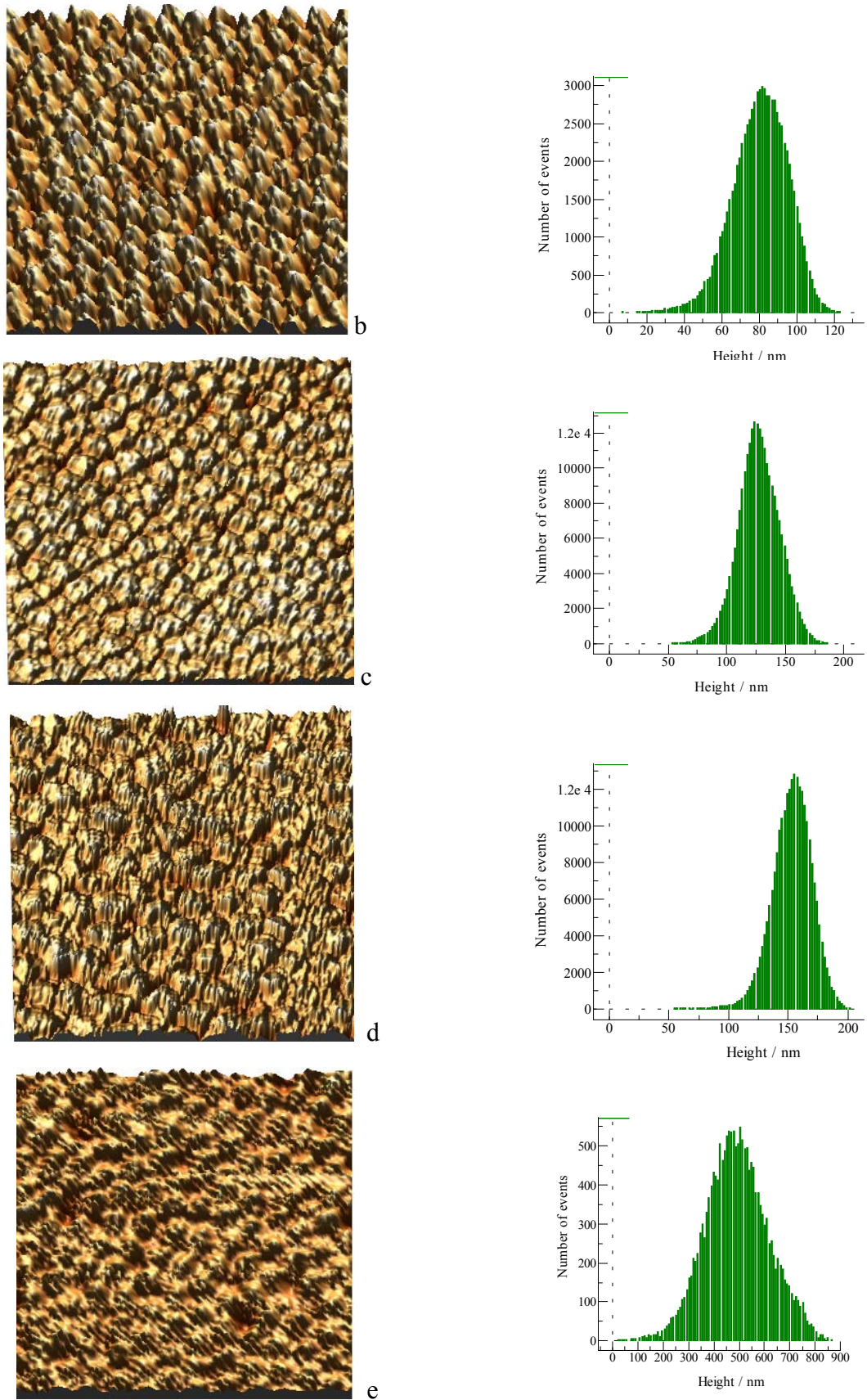


Fig. 4.3.6. AFM micrograph ($1.6 \times 1.6 \mu\text{m}^2$) of cobalt nanofilms prepared by pulse current ($j = 1 \text{ mA/cm}^2$, $t_{\text{off}}/t_{\text{on}} = 1/3$) at various deposition charges: (a) 0.24, (b) 0.48, (c) 0.72, (d) 0.95, (e) 1.2 Coulomb.

In all case the double substructures due to liquid crystal is observed. At higher deposition charge (e), the substructure caused by the alumina seems to disappear because the quantity of material deposited on the surface is large. All samples have homogeneous surface as expected for pulse electrodeposition. These structures are close to the ideal construction expected from the concept of double template deposition as shown on Fig. 4.3.2.

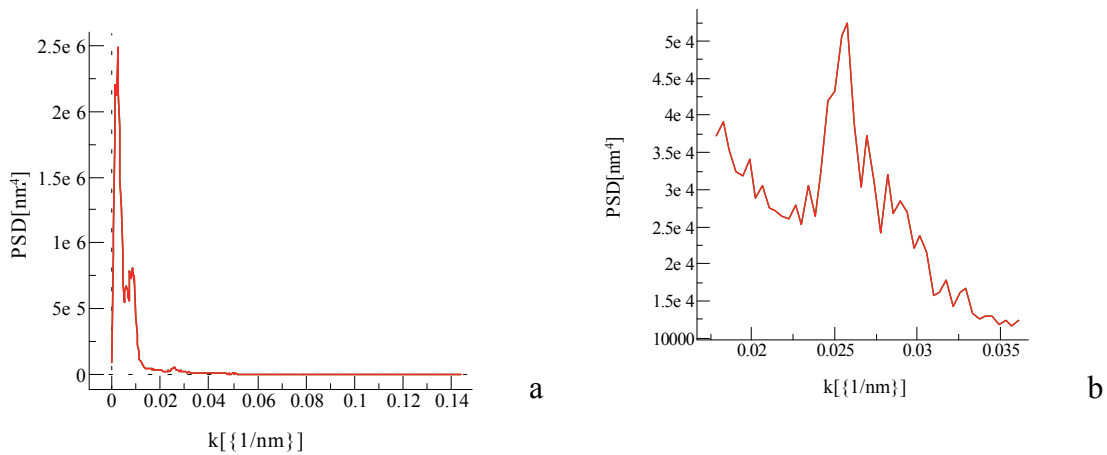


Fig. 4.3.7. Power spectra density functions of the cobalt film deposited by double template. (b) is a zoom of the small signal that appears at the wave number 0.025 nm^{-1} in spectrum (a).

The existence of the double substructure appears on the power-spectra density functions obtained from the 2D Fourier transform of the pictures. Two signals at k values 0.01 and 0.025 nm^{-1} can be observed on Fig. 4.3.7a. The first signal, with relatively high intensity comes from the repeat distance caused by alumina membrane. In many cases the inverse of this wave number is about 110 nm ; the values are close to the periodicity of samples deposited from aqueous solution within the AAO. AFM can scan this larger distance with good resolution; hence the high intensity of this signal. The second peak at relatively high wave number has small intensity (its zoom is shown on Fig. 4.3.7b) and account for the repeat distance caused by the columns of liquid crystal.

The double substructure was successfully reproduced with the Brij 76 plating mixture; the characteristics of the samples are in agreement with the results obtained with Brij 78 mixture. The average height and the surface roughness of samples prepared by DC and pulse current from Brij 76 mixture was determined. The comparison of the values can give more information about the change in the structure due to pulse current.

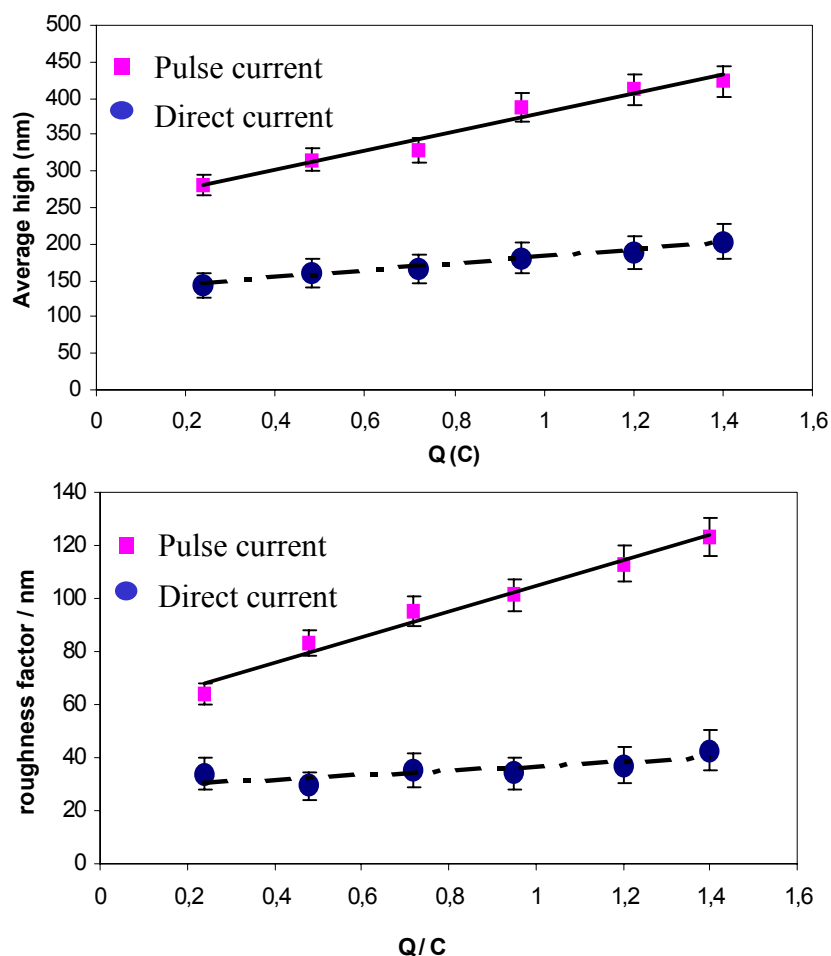


Fig. 4.3.8. Variation of the average thickness and the root mean square roughness of samples with the quantity of electricity.

The variations of the average thickness and the root means square roughness of the samples with the deposition charge are show on Fig. 4.3.8. In both cases the parameters have linear dependence on the quantity of electricity. The thickness obtained with pulse current is greater than that with direct current. Therefore the quantity of material deposited by pulse is more important. The rate-determining step of pulse electrodeposition is controlled by mass transport [111]. During the current relaxation, metallic ions have enough time to migrate from the solution to the electrode where it will be deposited.

The roughness factors of material deposited with pulse current are also larger compared to those with direct current. The presence of well defined substructures in this case account for the higher values of RMS.

4.3.4 Impedance spectra of cobalt film deposited from Brij 76 plating mixture

De Levie calculated the impedance of a porous electrode consisting of cylindrical pores, all with equal diameter and depth. In the absence of faradaic process, the Nyquist plot consist of a vertical line at low frequency and a line forming a 45° angle with the real axis at high frequency. At a critical frequency, the penetration depth of the ac signal is equal to the pore length, this lead to the double layer charging of the whole inner pore / electrolyte interface [100].

Fig. 4.3.9 shows the Nyquist representation of the impedance data of cobalt nanoporous film deposited from liquid crystal mixture within the pore of alumina membrane. The spectra were recorded in 0.4 M LiClO₄ at -0.5 V vs SCE and the frequency range from 100 kHz to 5 Hz. The negative potential (-0.5V) was used to avoid any oxidation of the cobalt film during the measurement. The potentiodynamic curve shows the oxidation and passivation of the film for potential greater than -0.35V vs SCE.

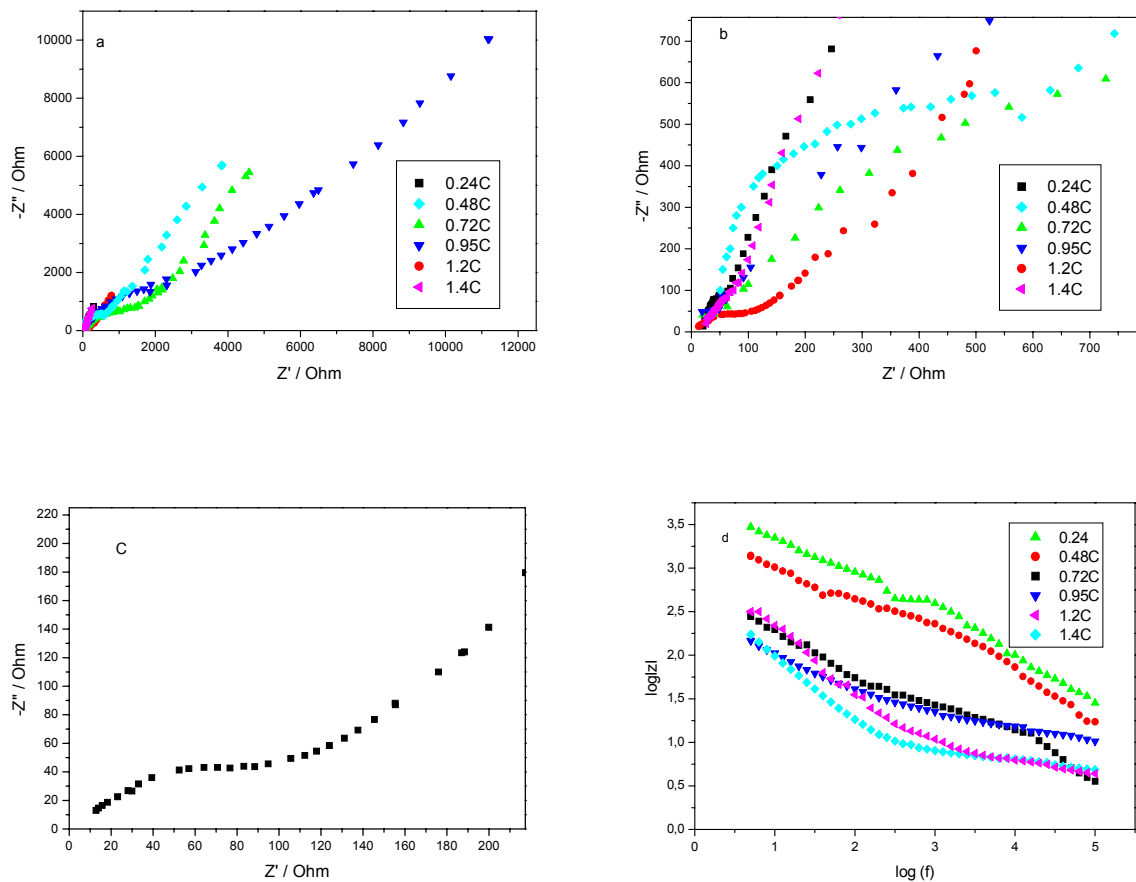
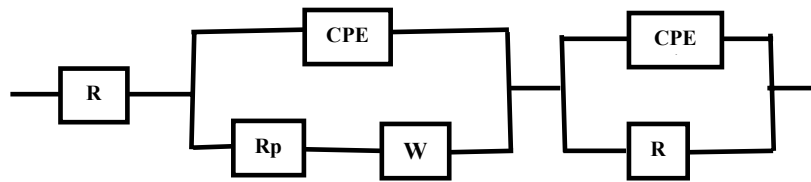


Fig. 4.3.9. Impedance data of cobalt nanofilm deposited from Brij 76 liquid crystal mixture: (a) high and low frequency part, (b-c) high frequency details and (d) Bode magnitude.

The nanoporous films from liquid crystal give Nyquist plot similar to that of samples deposited from aqueous solution; but the high frequencies semicircle is less pronounced. The details at high frequency (b-c) show the 45° inclined lines, this indicates the charging of the electrical double layer as predicted by the transmission line model of electrode with cylindrical or hexagonal pore arrangement [71,101,112]. Therefore, ordered hexagonal pores exist on the cobalt nanofilm as expected from the liquid crystal. However, the data differ from the expected vertical lines that are supposed to appear at low frequencies. The ~45° deviation of the low frequency line may come from the opened space that exists between the nanorods. The pores between the fibers are open as indicated on AFM micrograph. Song et al. [113] showed that the pore size distribution causes a decrease of the angle formed by the low frequency line with the real axis, from 90° to lower values; owing to the fact that the penetration depth at each frequency depends on the pore radius. The impedance results were analyzed with the following equivalent model.



$$Z(j\omega) = R_s + \frac{R_p \sqrt{\omega} + \sigma e^{-j\frac{\pi}{4}}}{A\omega^\alpha e^{j\alpha\frac{\pi}{2}} \left[R_p \sqrt{\omega} + \sigma e^{-j\frac{\pi}{4}} \right] + \sqrt{\omega}} + \frac{R}{1 + A'\omega^{\alpha'} R e^{j\alpha'\frac{\pi}{2}}} \quad (23)$$

The arrangement of the elements in the equivalent circuit points to the presence of two separated time constants. The high frequency time constant represented by (CPE' x R) is attributed to electrode surface inhomogeneity or to its porosity. This parameter is very small and cannot be clearly separated from the kinetic part of the Nyquist representation. This time constant may be related to shape or the small size of the particles. Some relaxation process could take place on Cobalt /Aluminum oxide composite. The high frequency time constant can also be attributed to the charging of the space charge layer. The low frequency time constant (C_{dl} x R_p) is proposed to be the consequence of charge transfer process (electrode kinetics) at the electrode-electrolyte interface. The Warburg element accounts for the diffusion observed at low frequency. At low frequency, diluted oxygen and/or lithium ions diffuse into the pore of the material. In this last case the diffusion of lithium corresponds to the solid-state diffusion or intercalation. Shengyi [114] developed the analytical model that accounts for the intercalation

of Li^+ into cobalt oxide and graphite porous electrode immersed in conductive electrolyte. See appendix for the calculation of $Z(j\omega)$ and for the example of impedance curve fitted with the model.

In all cases, the proposed model was in total agreement with the experimental data. The characteristics of the samples determined by fitting with the model are summarized in the following table.

Tab. 4.3.1. Impedance data of cobalt nanofilm prepared with the Brij 76 liquid crystal.

Q [C]		0.24	0.48	0.72	0.95	1.2	1.4
R_s [Ω]		5.50	26.75	28.28	27.51	26.32	15.36
R_p [Ωcm^{-2}]		1394	5415	10615	13780	611.5	5135
R [Ωcm^{-2}]		83.5	0.89	7275	8780	394.25	2197.5
W / σ [$\Omega\text{cm}^{-2}\text{s}^{-1/2}$]		6.11×10^{-5}	7.86×10^{-4}	3.97×10^{-6}	1.3×10^{-6}	1.42×10^{-4}	4.40×10^{-6}
CPE'	α'	0.73	0.84	0.75	0.91	0.66	0.74
	A' [$\text{Fcm}^{-2}\text{s}^{\alpha-1}$]	1.96×10^{-8}	1.74×10^{-8}	4.22×10^{-8}	9.25×10^{-9}	1.23×10^{-8}	8.3×10^{-9}
CPE	α	0.78	0.41	0.65	0.54	0.63	0.69
	A [$\text{Fcm}^{-2}\text{s}^{\alpha-1}$]	1.28×10^{-4}	1.42×10^{-4}	7.8×10^{-5}	4.89×10^{-5}	4.14×10^{-4}	4.48×10^{-4}

The exponent (n') that corresponds to the film constant phase element (Q') is very close to one in all cases, therefore the space charge layer behave like a real capacitor. On the other hand, the non-ideal behavior of the interface double layer capacitor is observed from the small exponent (n) of the corresponding constant phase element. The film constant phase coefficient (Y'_0) is in the nanofarad range and its resistance is very small. The time constants deduced from these values will be very small. This explains why the two frequency loops are not clearly separated on the Nyquist plot.

The present results show how electrodeposition of metal by combination of metallic salt dissolved in lyotropic crystalline phase of surfactant with the porous alumina membrane, produces metal films that contain two well-defined nanostructures. The materials that grow from the bottom of the pore of alumina have many subdivisions caused by the columns of liquid crystal. The films have a high specific area and good stability. In summary, the hexagonal phase

of lyotropic liquid crystal provides a versatile route for the production of porous electrode with high surface area. Such electrodeposition technique could offer a new method of modification of aluminum surface with metallic nanoparticles. It could also offer new generation of electrode materials used in batteries, fuel cell and electrochemical capacitors or in electroanalysis. Therefore, it will be beneficial to study the behavior of such metal film in aqueous solution.

4.4 Electrochemical behavior of cobalt nanoparticles in LiClO_4 aqueous solution.

Various electrochemical techniques have been developed to study the electron transfer or the interface between aqueous solution and solid electrode material under potential control. Among them, anodic linear sweep voltammetry, linear polarization and electrochemical noise give information about the oxidation and corrosion of a metal; while Mott-Schottky analysis is useful for the behavior of semiconductor electrode in solution.

4.4.1 Anodic linear voltammetry and corrosion measurement.

Samples from Brij 76 mixture were submitted to anodic linear sweep voltammetry (ALSV) analysis. ALSV has been shown to be a convenient electrochemical method for the characterization of the phase structure of an alloy [115]. It is also used to detect the presence of metal on a surface. In particular, ALSV gives various current peaks characteristic of metal oxidation or phase structure of an alloy [116]. Cobalt film deposited by double template technique was oxidized in 0.4 M lithium perchlorate at room temperature with slow sweep rate of 2 mV/s. Platinum and SCE were used respectively as counter and reference electrode.

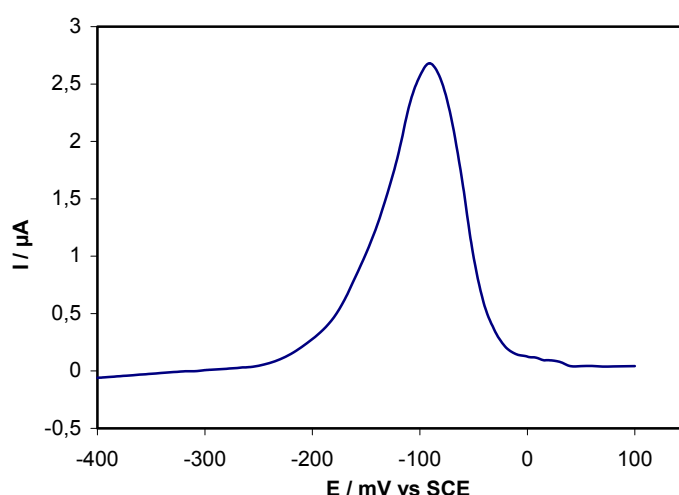


Fig. 4.4.1. ALSV of cobalt nanomaterial recorded in 0.4M LiClO_4 with the scan rate of 2 mV/s. The sample was prepared by double template with a pulse current density of 1 mA/cm^2 for 15 min. The geometric electrode area is 0.2 cm^2 .

The presence of one oxidation peak on the ALSV spectrum accounts for the existence of one element that forms a single phase system on the surface of the electrode. At potential close to -200 mV vs SCE, an oxide film grows on the electrode surface; passivation occurs when the surface is completely covered; the current decreases rapidly and tends to zero.

Corrosion is a complex process involving the oxidation of metal and the concurrent reduction of a species in solution, usually the proton in acid solution and oxygen in neutral or alkaline media. The metal ion may dissolve in solution or form an oxide layer, which may or may not be dense enough to prevent further oxidation, depending on the nature of the corroding metal and the composition of the solution [117]. Tafel suggested that the kinetics of electrochemical reactions, away from the reversible potentials of the half-cell or corrosion potentials in the case of corrosion reactions, could be described by a semi-logarithmic relationship between the overpotential and the log of the current [118].

$$\eta = a + b \log j \quad (24)$$

The over potential is a linear function of the log of current density. For accurate estimation of the corrosion rate by Tafel method, the linear portion should extend over about one decade of log i axis [119].

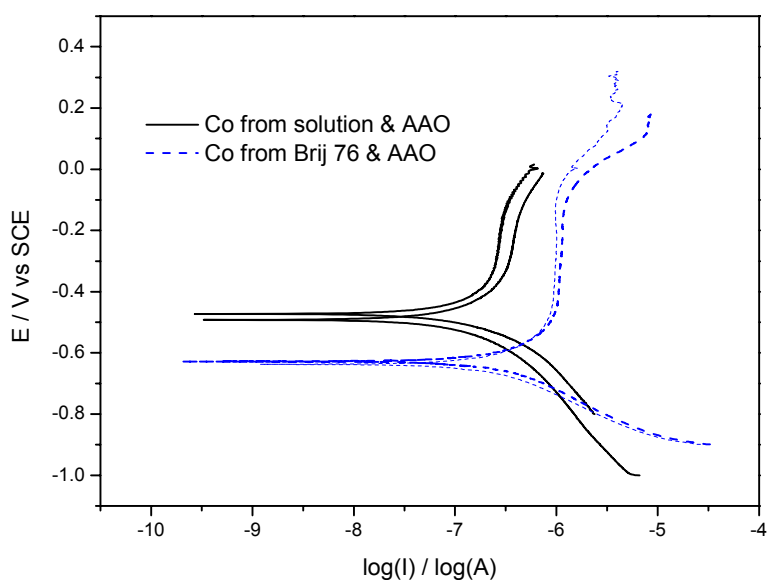


Fig. 4.4.2. Polarization curve when cobalt nanoparticles are in the pores of alumina membrane. The spectra were recorded in 0.4 M LiClO_4 aqueous solution with 3 mV/s scan rate; the electrode area was 0.2 cm².

The graph of Fig 4.2.2 compares the corrosion curve of cobalt deposited from Brij 76 (with substructure) to that prepared directly from solution within the pore of the alumina. In each case two curves were measured in similar conditions to confirm that the difference observed in the corrosion potential of the films is not due to experimental error. Two common aspects exist on the corrosion curves of sample prepared with Brij 76 or directly from aqueous solution.

The cathodic branch of each curve obeys to Tafel equation; the reaction at the cathode is assigned to the reduction of water ($2 \text{H}_2\text{O} + 2\text{e}^- \rightarrow \text{H}_2 + 2 \text{OH}^-$) or open-air diluted oxygen ($\text{O}_2 + 2 \text{H}_2\text{O} + 4 \text{e}^- \rightarrow \text{H}_2 + 4 \text{OH}^-$) all in neutral medium.

The part of the anodic branch close to the corrosion potential is seen to be curved; it does not follow Tafel equation. Moreover, a passive zone where the current remains nearly constant is observed after the curved region. This behavior may be attributed, according to Flitt [119] in the case of steel corrosion, to the formation of non-passive surface film by deposition of impurities or corrosion product. At potential greater than -0.2 V vs SCE , the current begins to rise; such anodic polarization curve account for homogeneous corrosion. The pitting potential is defined as the potential below which, the metal surface remains passive and above which pitting corrosion starts to grow on the surface [120]. In the present case, the current rise at potential above -0.2 V vs SCE ; that is the potential at which active dissolution of cobalt nanofilm occurs in LiClO_4 .

The major difference between the corrosion curves is the value of the corrosion potential. Film deposited by double template (ie from Brij 76 mixture) has more negative corrosion potential, $E_{\text{corr}} = -0.65 \text{ V vs SCE}$. The E_{corr} of a similar film prepared directly from aqueous solution into AAO (solid lines of Fig. 4.4.2) is about -0.48 V vs SCE .

Since corrosion is a kinetic process, the observed potential difference cannot be explained with thermodynamic arguments such as the higher surface free energy ($\Delta G = -nF\Delta E$) which is proportional to the change in potential. This difference can be assigned to the size of the cobalt nanomaterial or to the specific area of the electrode. As showed by AFM measurements, the double template deposition using Brij 76 gives cobalt film with substructures and smaller particles size. This film should have higher specific area compared to that deposited directly from aqueous solution into the AAO. Particles with smaller size are more reactive, easier to oxidize and more catalytic compared to large particles. This should be the reason why the corrosion potential of such film is more negative.

4.4.2 Electrochemical noise measurement

Electrochemical noise is a general term describing the spontaneous fluctuation in current or potential that occurs in the electrochemical systems [121]. One of the sources of noise is the surface process occurring on the electrodes and specifically their inhomogeneities. These give rise to fluctuations at frequencies below 1 Hz. Other sources of noise are localized corrosion such as pitting and uniform corrosion [122, 123]. Three parameters derived from short noise theory have been reported to provide information related to the nature of the corrosion processes. The characteristic charge Q gives an indication of the mass of the metal lost in the event. The characteristic frequency f_n provides information about the rate at which these events are happening [123]. Moreover, the noise resistance R_n or R_p was claimed to be related to the corrosion resistance [124]. Therefore, a system undergoing active uniform corrosion can have both large charge and frequency. Localized corrosion, such as pitting can be characterized by small number of events, and is then expected to have a low frequency and high charge. In the case of passivity, the charge is expected to be low, while the frequency will depend on the process occurring on the passive film [123].

The electrochemical noise (EN) data of cobalt nanoparticles in 0.4 M LiClO₄ were recorded using the CompactStat B05030 InVium technologies. Current noise was measured using two electrodes of the same material and a SCE reference electrode. The WE + Sense was connected to the working electrode one while Ground (Gnd) was attached to the WE two. No additional CE was used; the electrochemical current noise was measured as the galvanic coupling current between two identical working electrodes.

Contrary to the corrosion techniques such as Tafel plot that evaluate the behavior of the electrode material under the applied over potential, electrochemical noise measures spontaneous processes which did not involve any external perturbation of the corroding system. The aim of this investigation is to evaluate the dynamic processes related to cobalt nanoparticles in perchlorate solution; particularly the spontaneous pits initiation, homogeneous corrosion or passivation of cobalt nanoparticles in solution and in the absence of any external voltage. Understanding the passivation processes is fundamental if such films have to be use in electrocatalysis. The spontaneous corrosion or passivation of the nanoparticles could inhibit the active center of the catalyst and influence the catalytic activity of the film.

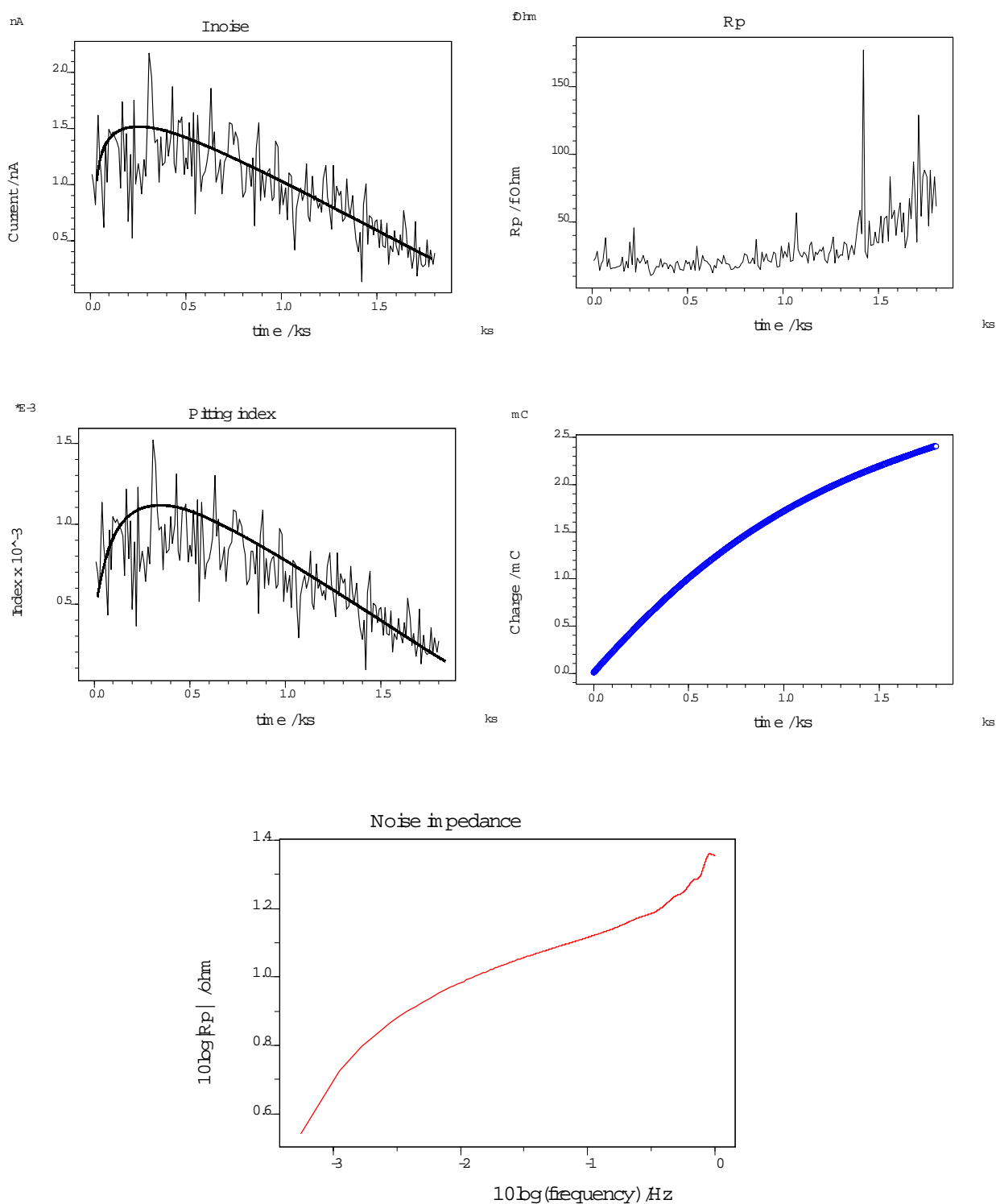


Fig. 4.4.3. Time domain electrochemical noise current, resistance, pitting index and charge of cobalt nanoparticles immersed in 0.4 M LiClO₄. The frequency domain analysis is also indicated in term of noise impedance. The frequency domain was generated by mean of maximum entropy methods. The film used for the measurement was deposited directly from aqueous solution into AAO membrane.

Fig. 4.4.3 shows the noise spectra of cobalt nanoparticles in LiClO₄ solution. According to Ma et al. [125], if the two electrodes suffer from localized corrosion, especially pitting attack, the net coupling current between two electrodes will be produced since the surface microstructure of the electrodes changes all the time. On the contrary, when two electrodes are corroded generally (homogeneous corrosion), their surface state may be considered to be approximately identical and no net current between the electrodes is observed.

The current noise increases slowly and remains relatively high for the first 500 seconds of the measurement; it could be due to oxide formation or to the surface inhomogeneities. The progressive decay of the current noise after 500 seconds measurement is assigned to surface passivation. Similar change with time is observed on the graph of pitting index. Moreover, the noise resistance (R_p), which is equal to the polarization resistance in some cases, increases slowly with time. This variation is in total agreement with the change of the pitting index or current noise with time and confirms the passivation of the surface. In general when the surface is passivated, its polarization resistance increases, therefore the noise resistance will increase and the net spontaneous current noise that flows between the coupled electrodes will decrease. The existence of net current noise in this case is assigned to the fluctuation caused by the surface inhomogeneities, roughness and formation of oxide or to the high specific area of the electrodes. This should not be assigned to pitting corrosion since there were no anodic passive films and no self-assembly monolayer on the particles before the noise measurement. Furthermore, there is no chloride or acid in solution. The passivation corresponds to the formation of a thin oxide layer on the particles.

The characteristic charge Q increases rapidly with time and tends to a constant value of about 2.5 mC. The total charge involved in this process (2.4 mC in 1800s) is high and accounts for homogeneous corrosion of the cobalt. If we assume that this process involves the oxidation of Co to Co²⁺, the mass of substance deduced from the Faraday law ($m = QM/2F$) and corresponding to the total charge consumed will be approximately 0.7 μ g.

In summary, EN offers a good method to the in situ monitor of spontaneous dynamic process of cobalt nanofilm in perchlorate solution at room temperature. The film undergoes homogeneous corrosion followed by passivation. The net current noise between two identical electrodes is assigned to fluctuations due to surface roughness and inhomogeneity or to the formation of an oxide layer on the particles, while the passivation is caused by the formation of a thin oxide layer on the particles. The evidence of the spontaneous oxidation of cobalt particles in LiClO₄ can be pointed out by the capacitance measurement in the form of Mott-Schottky plot.

4.4.3 Mott-Schottky analysis of cobalt nanofilm in Lithium perchlorate.

Much recent works have been devoted to semiconductor electrodes because of their application in photoelectrochemical conversion of solar energy. The behavior of a semiconductor-electrolyte junction is dominated by the large photosensitivity of the semiconductor, and the thick depletion layer that constitutes the space charge region of the semiconductor side of the junction [87]. For the two phases to be in equilibrium, their electrochemical potential must be the same. The electrochemical potential of the solution is determined by the redox potential of the electrolyte and the Fermi level determines the redox potential of the semiconductor. If the redox potential of the solution and the Fermi level do not lie at the same energy, a movement of charge between the semiconductor and the solution will occur to equilibrate the two phases. The excess charge that is now located on the semiconductor does not lie at the surface, but extends into the electrode for a significant distance. This region is referred to as the space charge layer and has an associated electric field [126]. Changing the electrode potential will shift the Fermi level of the semiconductor, the magnitude and direction of the band bending varies also with the applied potential. This will change the properties of the space charge layer. Mott-Schottky established (equation 19) the relation between the electrode potential and the space charge capacitance of a semiconductor electrode under depletion condition [88].

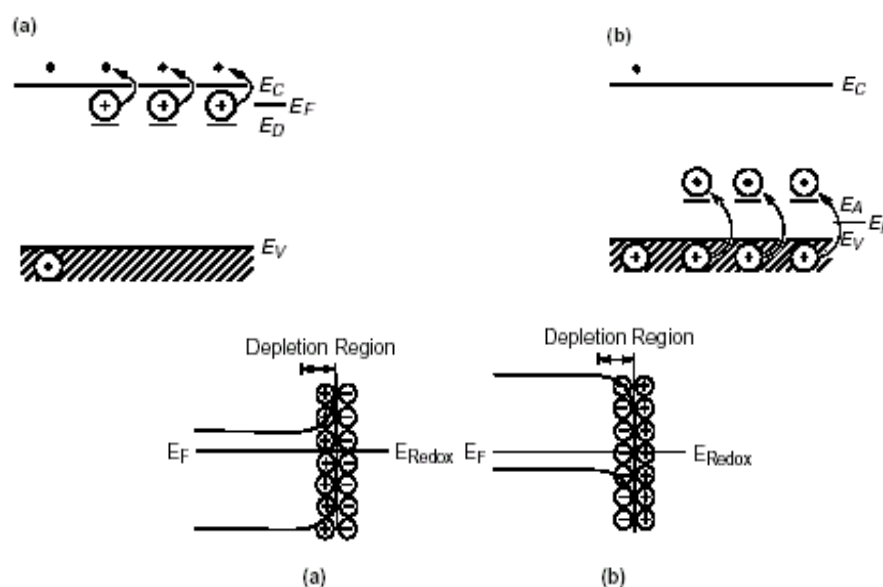


Fig. 4.4.4. Schematic diagram of the energy level and band bending for semiconductor electrode. In each case, (a) corresponds to n-type and (b) to p-type semiconductor. The band-bending diagram is for a semiconductor electrode in equilibrium with and electrolyte [126]. E_A , E_D , E_C and E_F refer to the energy level of acceptors, donors, conduction band and Fermi level respectively.

Fig. 4.4.4 shows the energy level and band bending of semiconductor electrode in equilibrium with electrolyte. In n-type semiconductor, the Fermi level lies just below the conduction band, whereas for p-type it is above the valence band. For n-type semiconductor electrode at open circuit, the Fermi level is typically higher than the redox potential of the electrolyte and electrons will be transferred from the electrode into the solution. For p-type semiconductor, the Fermi level is generally lower than the redox potential and electrons must flow from solution to the electrode [126].

The passive film of many metals exhibits electrochemical properties of semiconductor [127,128]. As example, the passive film of Zn in alkaline medium is known to be an n-type semiconductor with band gap energy of 3.2 eV [129]. Many surface physics and electrochemical techniques such as Moessbauer spectroscopy, x-ray photoelectron spectroscopy, EIS, electrochemical noise are widely used to study the passive films on metal. Mott-Schottky analysis is a powerful tool to probe semiconductor properties of passive film by which the donor or acceptor density of state and the flatband potential for the passive film can be obtained [127]. The aim of this investigation is to confirm the passivation of cobalt nanoparticles in LiClO₄ by the oxide layer, and to determine the electronic properties of the passivated nanoparticles.

Mott-Schottky (MS) plots were obtained by potentiodynamic electrochemical impedance spectroscopy (PDEIS), potential were scanned in the anodic direction using the CompactStat in-vitro technology instrument. The capacitance of the AAO or cobalt films was measured at 1 kHz in 0.4 M LiClO₄. At this frequency, the space charge layer capacitance C_s is easily separated from double layer and Faradaic responses. Thus the variation of the space charge layer capacitance with electrode potential is obtained straightforwardly from PDEIS spectrum analysis [130]. From impedance measurements, it was observed that diffusion is the dominant process at low frequency and that the film capacitance could be deduced from the high frequency part of the impedance spectra. Therefore, it is necessary to work at medium frequency (around 1000 Hz) since the space charge capacitance is sensitive around this frequency. A SCE was used as RE and a platinum foil as CE; the amplitude of the ac signals were 15 mV in the MS of alumina film and 5 mV in the case of cobalt film. Low ac amplitude was chosen to ensure the linearity of the frequency response and avoid destruction of the films.

According to equation (19) [$C_s^{-2} = 2(q \epsilon \epsilon_0 N_d)^{-1}(E - E_{fb} - kT/q)$] Mott-Schottky plot, the inverse square of the space charge capacitance C_s^{-2} versus semiconductor electrode potential E , gives a straight line.

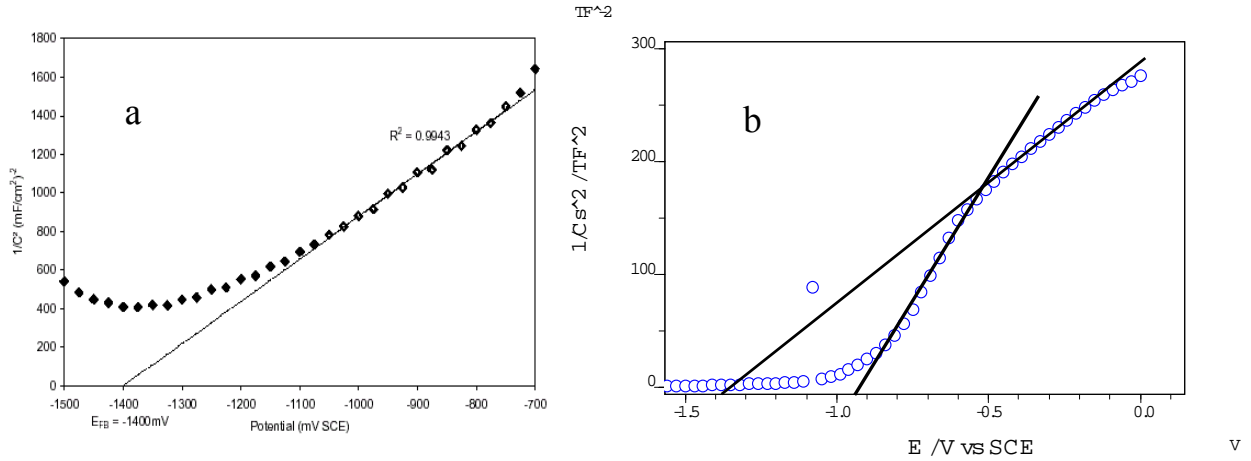


Fig. 4.4.5. Mott-schottky plot of passive alumina membrane formed on aluminum. (a) Curve copied from [131] to compare with the one measured, (b) Curve of thin alumina film obtained by double anodization at 10°C in oxalic acid; TF^{-2} refers to Tetra (10^{12}) Farad square. The electrode area was 0.2 cm^2 .

The Schottky plot of Fig. 4.4.5a was recorded in 0.1 M NaCl with an aluminum electrode polished and degreased in acetone, ethanol and methanol [131]. The spectrum measured in the present experimental conditions (Fig.4.4.5b) is in agreement with the literature result of Fig.4.4.5a [131]. In both cases, passive film on aluminum behaves like n-type semiconductor. The flatband potential (potential at which the Fermi level of the semiconductor is at the same energy as the solution redox potential, and no net charge transfer occur [126]) of the film in Fig 4.4.5a is -1.4 V vs SCE . In the case of Fig 4.4.5b, the flatband potentials determined from the intercept of the lines with the potential axis ($E_{fb} = E - kT/q$ when $C_s^{-2} \sim 0$) are -0.95 V and -1.4 V vs SCE . The difference between the spectra can be due to the composition of the electrolyte (NaCl in one case and LiClO_4 in the other case) or to the method of preparation of the passive film. This last situation seems to be most interesting since the anodized passive film consists of an under barrier layer and the porous outer part, both parts may have different electronic properties and this can account for the presence of two lines as shown on MS plot of AAO reported on Fig. 4.4.5b. The donor density of state or donor concentration in the passive film can be deduced from the slope S of the Mott-Schottky plot.

$$\text{From equation 19, } S = \frac{2}{q \varepsilon \varepsilon_0 N} \text{ therefore } N = \frac{2}{q \varepsilon \varepsilon_0 S} \quad (25)$$

Where q is the elementary charge, equal to $-e$ for holes and $+e$ for electron; ε the dielectric constant, ε_0 the permittivity of vacuum ($\varepsilon_0 = 8.85 \times 10^{-14} \text{ F/cm}$) and S the slop of the MS Plot.

The dielectric constant of Al_2O_3 is 9 at 25 °C. If we assume that the passive film on aluminum is made of Al_2O_3 and not aluminum hydroxide, the donor densities of the two lines will be 1.37×10^{15} and $3.14 \times 10^{15} \text{ cm}^{-3}$.

In summary, anodic aluminum oxide behaves like n-type semiconductor with a hetero junction leading to two flatband potentials of -0.95 V and -1.4 V vs SCE in 0.4 M LiClO_4 . As described in [131], the primary charge carriers in this passive film are oxygen vacancies. In the present case, they are present in high concentration 1.37×10^{15} and $3.14 \times 10^{15} \text{ cm}^{-3}$.

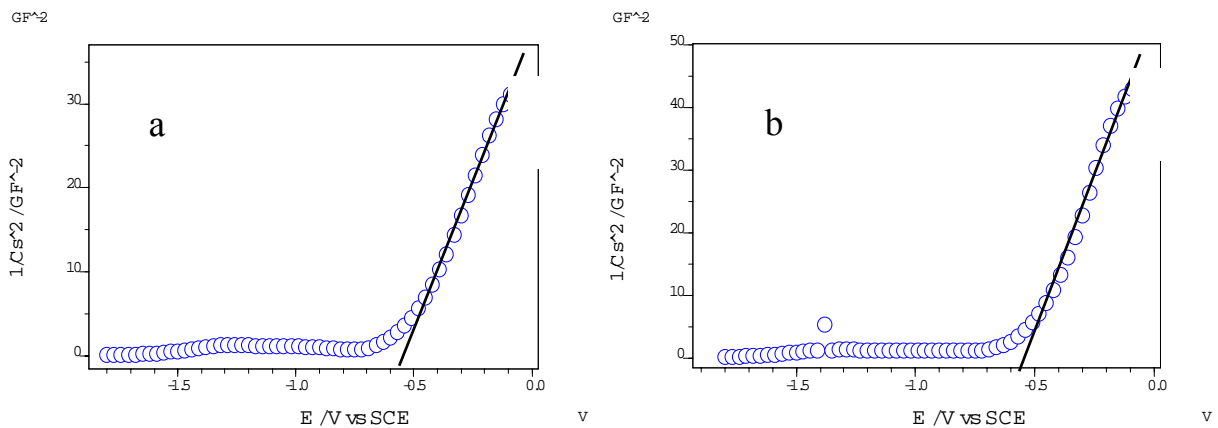


Fig. 4.4.6. Mott-Schottky plot of cobalt nanoparticles recorded in LiClO_4 aqueous solution. (a) Sample deposited with aqueous solution and AAO, (b) in the presence of Brij 76 and AAO. The curves were recorded with 1 kHz and 5 mV ac sinusoidal voltage. Electrode area 0.2 cm^2 . GF^{-2} refers to Giga (10^9) Farad square.

Fig 4.4.6 displays the MS plots of cobalt nanomaterial deposited from aqueous solution into AAO (a) or from Brij 76 into AAO (b). In both cases, the inverse of the square values of the capacitance C_s^{-2} is constant and tends to zero for potentials negative than -0.6 V vs SCE. Straight lines with positive slopes are observed at potential greater than -0.6 V . This refers to the n-type semiconductor behavior of the passive film formed on cobalt particles in perchlorate solution. The intercept of the lines with the x-axis gives a flatband potential of -0.6 V vs SCE in both cases. It is well known that at potential negative than the flatband potential for n-type semiconductor, there is an excess of charge carriers (electrons) in the space charge region, which referred to as an accumulation region. In p-type semiconductor, accumulation occurs at potential greater than the flatband potential [126]. The accumulation of charge may increase the value of the space charge capacitance, therefore the inverse of the square of high capacitance values may tend to zero in the accumulation region. This may account for the horizontal line observed in Fig. 4.4.6 at potential below -0.6 V .

If we assume that the passive film of cobalt consists of CoO (its dielectric constant is 12.9 at 25°C [132]), the donor density of state calculated from equation (23) will be $6.89 \times 10^{18} \text{ cm}^{-3}$.

It is important to note that the flatband potential of the cobalt film is very close to the corrosion potential ($-0.65 < E_{\text{corr}} < -0.55 \text{ V vs SCE}$) and that the straight line of the MS plots appears in the potential regions that correspond to the anodic branch of the corrosion curves (see Fig. 4.4.2). The flatband potential and the corrosion potential are equilibrium potential at which there is no electron transfer. Therefore, the results of both analytical methods are in good agreement.

4.5 Partial conclusion

Cobalt nanoparticles were deposited by single and double template techniques on a modified aluminum surface. During the electrochemical process the electrical parameters were controlled accurately. As a result, high current density and short time are needed to prepare organized particles from aqueous solution into AAO membrane with intact barrier layer. Moreover, pulse current is necessary in the case of double template deposition using non-ionic surfactant as plating mixture. In this last case, particles that grow from the bottom of the AAO have many substructures caused by the columns of liquid crystal. This subdivisions increase the specific area and the reactivity of the cobalt films. The corrosion potential of the cobalt film with substructure shifted cathodically and account for the high reactivity associated to particles with small size, or to the different in deposition processes. Further analysis such as electrochemical noise reveals the homogeneous corrosion and spontaneous passivation of the cobalt particles in perchlorate. The passivation of the particles was confirmed by Mott-Schottky measurement. The passive cobalt particles behave like n-type semiconductor with high oxygen vacancies or metal interstitials ($6.89 \times 10^{18} \text{ cm}^{-3}$) known as donors and a flatband potential of -0.6 V vs SCE . This observation is in agreement with various studies on the electron transfer at passive interfaces. The barrier layer of the passive film on metal surface is a defective structure containing high concentrations of point defects. The defects are the electronic dopants, oxygen vacancies and metal interstitials being donors and cation vacancies being acceptors [133].

5 Double template deposition and characterization of alloys nanoparticles.

The physical and chemical properties of many solids can be attributed to metallic elements. Examples include magnetic materials used in data storage, superconductors and catalysis [19]. Cobalt and nickel-based alloys are particularly attractive due to their magnetic properties. Electrodeposited magnetic films have application in computer read/write heads and micro electromechanical systems [134]. Other possible applications include magnetic recording media, sensor [30] and giant magnetoresistance properties of CoCu, FeAg and CoAg multilayers [135]. The binary alloy CuNi showed a promising magnetic phase transition in the desired temperature range for hyperthermia treatment of cancer [136]. ZnNi and ZnCo alloys present higher resistance to corrosion than pure metal [137]. Macroscale electrodeposition of CoNi and CoFe base magnetic films was investigated [138].

In the present chapter, we report on the nanoscale deposition and characterization of NiCo, NiCu and ZnNi alloys. Each alloy nanoparticles was first prepared by electrochemical reduction of ions dissolved in the appropriate aqueous solution within the pore of AAO. Secondly, the hexagonal phase of a lyotropic liquid crystal containing metallic ions was combined with the AAO for deposition. Two different types of surfactant molecules were used: a non-ionic surfactant (Brij 78) with larger columns (larger diameter) and an ionic surfactant with smaller columns. The aim is to show that surfactant can be used to control the size and the specific area of thin films. The corrosion and the semiconductivity of particles were also investigated to understand their electronic behavior.

5.1 Preparation and characterization of ZnNi alloy nanoparticles.

5.1.1 Electrochemical deposition

The aqueous solution used for electrodeposition of ZnNi contains 0.22 M zinc chloride, 0.11M nickel chloride, 0.5 M boric acid and 4 M ammonium chloride (solution A). The addition of large amount of ammonium chloride as supporting electrolyte reduces the increase in pH during deposition [137,139], while the boric acid improves the regularity and the quality (brightness) of the film [137]. In the case of double template processes, the first plating mixture contains 60 wt% of Brij 78 non ionic surfactant and 40 wt% of the aqueous solution A. The second mixture is made of 50 wt % CTAB ionic surfactant and 50 wt% of the aqueous solution A. After deposition, AFM and STM were used to analyze the surface of the film. The current density was

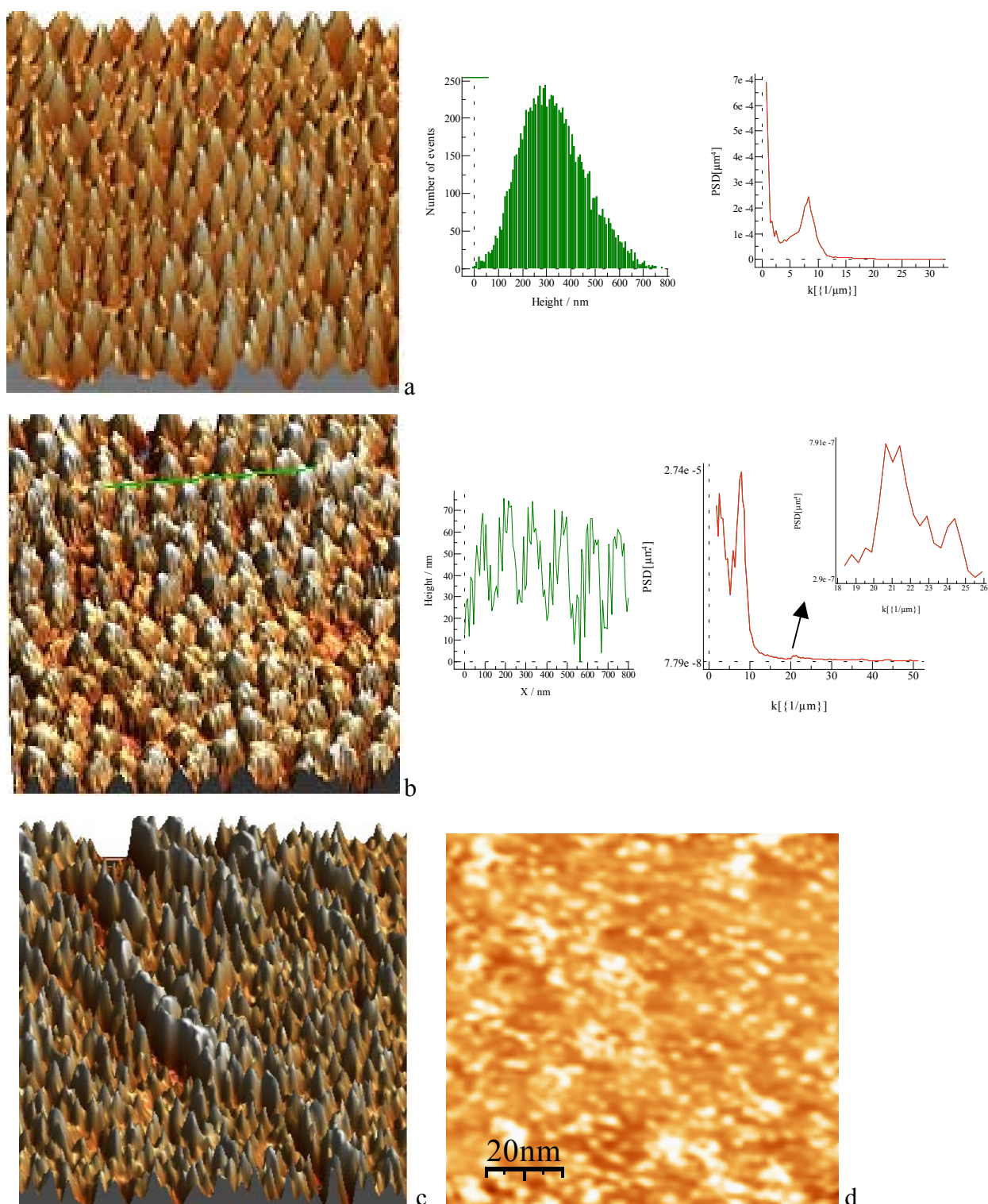


Fig. 5.1.1. AFM and STM micrograph of ZnNi alloy deposited (a) from aqueous solution into AAO, (b) from Brij 78 into AAO and (c-d) from CTAB into AAO. (a-b) are $1.6 \times 1.6 \mu\text{m}^2$ while (c-d) are $100 \times 100 \text{ nm}^2$. The bias voltage of the STM images (c & d) was 40 mV; the histogram of particle distribution shows in (a) the number of particles and their length. The profile in (b) shows the subdivisions of the particles and the power spectra density gives the wavelength that corresponds to the repeat distances. A 4 Matrix points Gaussian filter was applied to STM images for noise removal.

2.5 mA/cm² and the quantity of electricity were 0.6C and 0.4C in the case aqueous solution and liquid crystal respectively.

AFM reveals the formation of ordered nanoparticles when the material is deposited directly from aqueous solution within the pore of alumina (Fig. 5.1.1a). The periodicity (center-to-center spacing between two neighboring fibers) determined by line measurement and 2D Fourier transformed (see power spectra density function) is about 125 nm. The histogram of size distribution shows the number of particles and their specific height. The thickness of the AAO was about 50 nm; therefore it is possible to prepare fibers of about 600 nm in length in the pore of alumina.

The surface to volume ratio is very high in nanomaterial and surface effects play important role in physical properties of the films [105]. The hexagonal phase of lyotropic liquid crystal was used in order to reduce the size of the particles and increase the specific area of the film. Fig. 5.1b displays the AFM topography ZnNi alloy deposited from Brij 78 plating mixture. The particles have many subdivisions due to the columns of liquid crystal. The repeat distance in Brij 78 hexagonal mixture is 8.2 nm [59] and the diameter of the pore of AAO is about 65 nm. Therefore many columns of surfactant penetrate in one pore of the alumina; after deposition and removal of the columns, the particles have many holes as shown on the profile carried out along the line. This sample has a double periodicity as observed on the PSD function. The first repeat distance caused by the pore of AAO gives a peak with large intensity on the PSD. This peak is followed by another small signal with lower intensity at $k = 20\mu\text{m}^{-1}$ that account for the repeat distance caused by the columns of surfactant. The STM micrograph of this sample is similar to that of Fig. 5.1.1d.

Fig. 5.1.1c-d represents the STM topography of the same alloy deposited in the presence of CTAB hexagonal mixture. Noise was removed on the STM images by applying 4 Matrix points Gaussian filter. The repeat distance in CTAB mixture is 3.5 nm [20]; this mixture should give material with smaller particles. The pore in this case cannot be resolved with 10 nm AFM tip, hence the used of STM. The 100 x 100 nm scan range image confirms the existence of pores in the material.

In general, the size of ZnNi alloy nanoparticles decreases considerably from Fig 5.1.1a to d. Surface with mesoporous material could be very interesting in the electronics industry or in electrocatalysis. In electronics, plasmon resonance can be tailored by varying the structural features, sizes and spacing of metallic nanostructure film [9, 10]. By appropriate choice of the surfactant molecule, it is possible to control the size of nanoparticles.

5.1.2 Polarization behavior of ZnNi alloy nanoparticles.

The electrochemical deposition of two metallic species dissolve in solution may lead to the formation of an alloy or to bimetallic layers. A well crystalline alloy having two constituents A and B may give under potentiodynamic stripping, various anodic peaks characteristic of phases or phase transition that occur during oxidation. That is, a solid solution A_xB_y may not give separated peaks of A and B at their corresponding redox potential but continuous anodic peaks that account for phase transition. In the case of single-phase alloy and bimetallic layer of material, separated peaks of A and B will occur at their respective oxidations potentials. The phase of the ZnNi alloy nanoparticles was investigated by potentiodynamic in 0.4 M LiClO_4 .

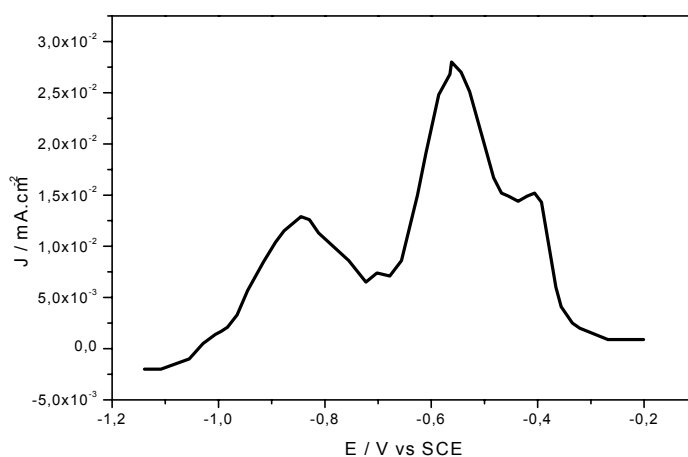
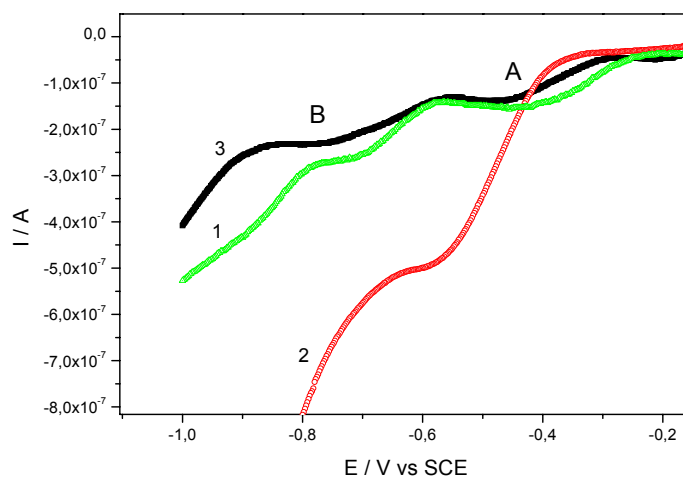
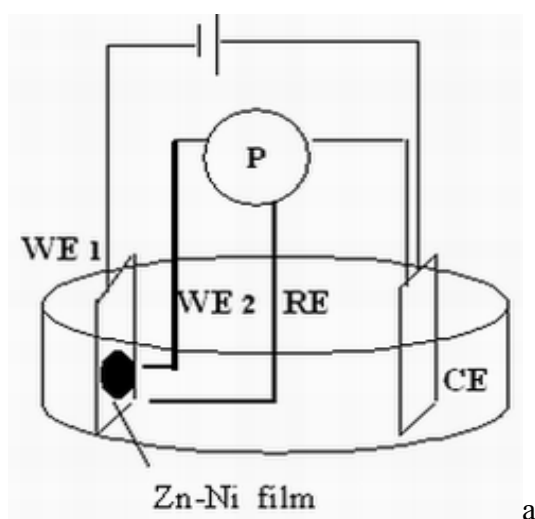


Fig. 5.1.2. Polarization curve of ZnNi alloy nanoparticles deposited from aqueous solution (with a quantity of electricity of 0.6 C) into AAO. The spectrum was recorded in 0.4 M LiClO_4 aqueous solution with the scan rate 5 mV/s.

Fig. 5.1.2 shows the polarization curve of Zn-Ni alloy nanomaterial. The I/E curve exhibits four anodic peaks at -0.85, -0.69, -0.55 and -0.40 V vs SCE. The peak at -0.4V may be attributed to nickel dissolution. Three other anodic peaks at more negative potentials may be attributed to successive transitions of alloy phases by progressive dissolution of zinc: as reported by Torres [137], δ -phase would be transformed into γ -phase then into α -phase through successive zinc dissolution steps. Considering the stripping result and the deposition technique (galvanostatic codeposition of ions), it can be suggested that the films consist of Zn-Ni alloy nanoparticles and not bimetallic layers.

The qualitative composition of the film was also investigated. The alloy was oxidized under galvanostatic condition at the working electrode one (WE₁). A small platinum wire (WE₂) placed near by the WE₁ was used as indicator electrode (see Fig 5.1.3a). The ions formed by dissolution of alloy at the WE₁ were reduced at WE₂ by linear voltammetry. A similar experiment was done with a nickel film. Secondly, zinc and nickel ions of an aqueous solution were reduced under the same condition on platinum electrode and the curve was compared with that obtained from the film. The results are summarized on Fig 5.1.3b. The voltammetry curve



b

Fig. 5.1.3. Reduction of Zn^{2+} and Ni^{2+} ions dissolved in aqueous solution containing 2.5×10^{-3} M ZnCl_2 and 5×10^{-3} M NiCl_2 (1). Reduction of ions formed after the oxidation of the Ni nanofilm (2) and Zn-Ni nanofilm (3). The current plateau A corresponds to the reduction of Ni^{2+} and B to that of Zn^{2+} . Scan rate 5mV/s. All reductions were done on 1.9×10^{-3} cm² platinum (WE₂ of scheme a) in an aqueous solution containing 0.4 M LiClO_4 .

obtained after oxidation of ZnNi film (curve 3) is in good agreement with the reduction curve of Zn^{2+} and Ni^{2+} recorded from an aqueous solution with known concentration (curve 1); this confirms the presence of zinc and nickel in the film.

According to the signal obtained after oxidation of the nickel film (curve 2); it can be deduced that the more cathodic signal (reduction signals B) correspond to the reduction of zinc ions while the less cathodic (signal A) is the reduction of nickel ions.

In linear potential sweep voltammetry, the peak current is proportional to the concentration of the electroactive element [84].

$$I_p = 2.69 \cdot 10^5 n^{3/2} A D^{1/2} v^{1/2} c \quad (26)$$

Where n is the number of electrons, A the electrode area (cm^2), v the scan rate (V/s), D the diffusion coefficient (cm^2/s) and c the concentration (mol/l). If we neglect the difference between the diffusion coefficient of Ni^{2+} and Zn^{2+} in $LiClO_4$, the sum of two peak currents should be proportional to the sum of the respective concentration. Since the ions present in solution come from the stripping of ZnNi alloy, the composition of the alloy can be obtained as follows:

$$x_{Ni} = \frac{c_{Ni}}{c_{Ni} + c_{Zn}} = \frac{I_{Ni}}{I_{Ni} + I_{Zn}} \quad \text{and} \quad x_{Zn} = \frac{I_{Zn}}{I_{Ni} + I_{Zn}} \quad (27)$$

Where c_i is the concentration and I_i the peak current of element i calculated from curve 3 by taking the reference (base line) at the point where the reduction of the element begins. The peak current of nickel and zinc reduction is about 0.06 and 0.1 μA respectively. The fraction of nickel and zinc deduced from the current is 0.37 and 0.63 respectively, and the alloy formula is approximately $Zn_{0.63}Ni_{0.37}$.

The mole fractions of zinc and nickel ions calculated from their concentration in the plating aqueous solution ($x_i = n_i/n$) are 0.66 and 0.33 respectively. It can be deduced after comparison of the mole fractions obtained with these two methods, that the compositions of the alloy reflect the one of the plating mixture. The electrodeposition of ZnNi alloy didn't exhibit anomalous characteristics.

5.1.3 Electrochemical impedance measurements

The ac EIS is widely used to analyze the electrical properties of materials having high-resistivity. The resistance contribution from various phases (double layer, grain boundary), the relaxation frequency and time constant of the material could be derived from ac EIS [140]. All

impedance spectra were recorded at -1V vs SCE. This potential was chosen to avoid the formation of oxide film or the degradation of the film during measurement. It can be seen from Fig. 5.1.2 that a potential more positive than -1V may cause different oxidative processes in the film.

The Nyquist representation of the impedance data of the nanoalloy is shown on Fig. 5.1.4. The film deposited from aqueous solution shows two half semicircles at high and medium frequency, and a straight line at low frequency. Similar spectra are obtained with samples from liquid crystal; but the semicircle at high frequency becomes very small. According to the comment made on similar spectra by Kim et al. [141], the intercept of the high frequency semicircles with the real axis is related to the bulk ($\text{Al}_2\text{O}_3/\text{ZnNi}$) resistance (R_{po}) of the nanofilm. The semicircles at medium frequencies are assigned to the parallel combination of the charge

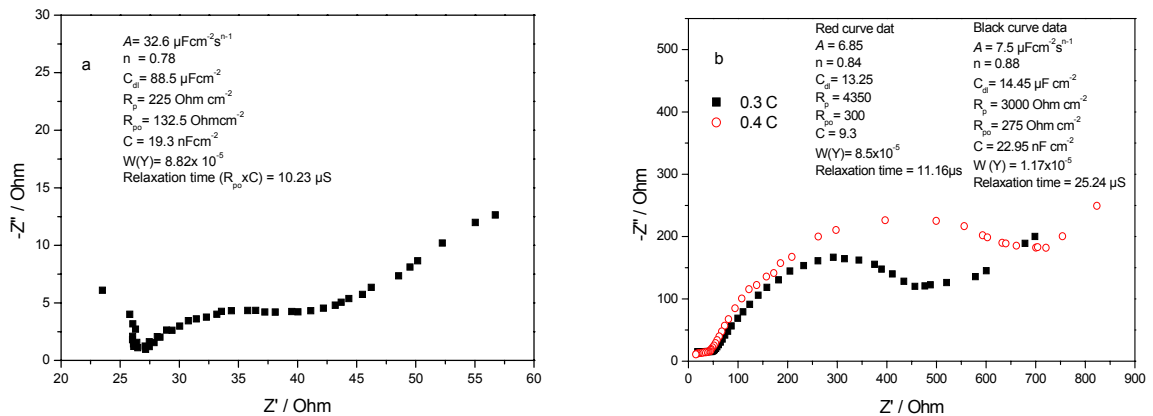
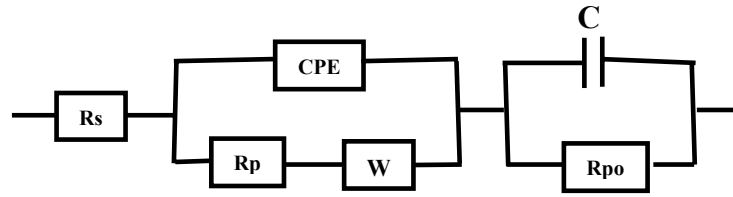


Fig. 5.1.4. Impedance spectra of Zn-Ni alloy mesoporous film deposit from aqueous bath (a) and in the presence of liquid crystals (b). Spectra were recorded in LiClO_4 form 100 kHz to 5 Hz with 10 points/decade and 5 mV amplitude of ac voltage. The electrode potential was -1V vs SCE. The inserted data represents the fitting values.

transfer resistance (R_p) in the electrode and the double layer capacitance (C_{dl}). At lower frequency there is a straight line due to diffusion of (open air) diluted oxygen and Li^+ ions within the pores of the thin film. Such curve shape reveals the presence of two-separated time constant at higher frequencies as shown on Nyquist plot. As described in [76], the separated time constant may be due to electrode surface roughness or to its porosity. Since the high frequency semicircle was not present in impedance spectrum of pure nickel nanofilm (not shown here) deposited in the same condition, the separate time constant may also be related to the composition of the material. Zn-Ni alloy has high resistance than pure metal [137] and its relaxation may appear in the high frequency region.

The impedance data of ZnNi nanoalloy were fitted using ZsimDemo 3.20 software following equivalent circuit was used for data analysis. See appendix for calculation of equation 28



$$Z(j\omega) = R_s + \frac{R_p \sqrt{\omega} + \sigma e^{-j\frac{\pi}{4}}}{A\omega^\alpha e^{j\frac{\alpha\pi}{2}} \left(R_p \sqrt{\omega} + \sigma e^{-j\frac{\pi}{4}} \right) + \sqrt{\omega}} + \frac{R_{po}}{1 + jC\omega R_{po}} \quad (28)$$

The capacitance of the deposit (c) is in parallel connection with the pore resistance (Rpo). The pore resistance is that of the solution in the free space between particles. The interface between the bare metal and the solution is modeled as a double layer capacity (represented in the circuit by the constant phase element) in parallel with the polarization resistance (Rp). The Warburg element accounts for the diffusion process observed at low frequency region of the Nyquist plot. This model shows clearly the presence of two separate time constants. The high frequency component (C x Rpo) is characteristic of material property (relaxation in ZnNi/Al₂O₃ composite). The material properties such as relaxation time constant and interface characteristic deduced by fitting with this model are shown in each figure. The relaxation time constant is higher in the films deposited in the presence of liquid crystal.

The transmission line model of ideal electrode with hexagonal or cylindrical pores predicts a straight line of about 45° with respect to the real axis at high frequency of the Nyquist plot. A vertical line should be observed at low frequencies [101]. In the present case, the deviation from this model is due to the pore geometry, the electrode composition and roughness. According to the AFM measurement, a free space exists between particles and the pore geometry is not well defined.

5.1.4 Corrosion and Mott-Schottky analysis.

The corrosion potentials of ZnNi alloy nanoparticles were determined from polarization measurement in LiClO₄ solution. The polarization curves of three alloy films deposited respectively from aqueous solution into AAO, in the presence of Brij 78 or CTAB liquid crystal

are compared. The aim is to study the influence of the size of particles on the corrosion behavior and the reactivity of the film.

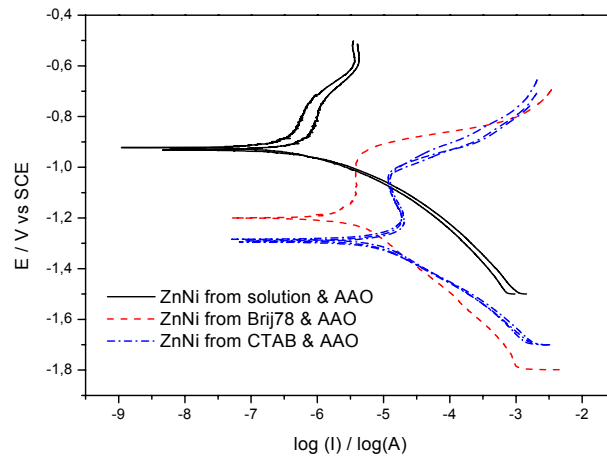


Fig. 5.1.5. Polarization curve of ZnNi alloy nanoparticles recorded at 3mV/s in LiClO₄, electrode area 0.2 cm².

Fig 5.1.5 shows the polarization curves of ZnNi film deposited by three methods. The cathodic part of each curve obeys the Tafel equation and corresponds to the reduction of water or diluted oxygen. On the contrary, the anodic branches are very far from the linear behavior expected from the Tafel equation. In general, the anodic part has a passive region where the current remains constant followed by an active zone where the current rise rapidly and tend to a maximum. The increase of the current is assigned to active dissolution follow by the formation of oxide layer on the surface of the particles. The films undergo homogeneous corrosion in lithium perchlorate solution. The corrosion potential depends on the methods used to prepare the surface. It is know from AFM / STM analysis that the size of particles decreases when the film is prepared in the presence of liquid crystal. Surface with smallest particles was obtained with CTAB mixture. In this last case, the corrosion potential of the electrode ($E_{\text{corr}} = -1.3\text{V}$ vs SCE) is the most negative followed by that of the film deposited in the presence of Brij 78 ($E_{\text{corr}} = -1.2\text{V}$ vs SCE) or directly from aqueous solution into AAO ($E_{\text{corr}} = -0.9\text{V}$ vs SCE). The cathodic shift of the corrosion potential is caused by the high reactivity associated with nanoparticles. That is, particles with very small size are easier to oxidize than larger particles. This also indicates that the passivation of smaller particles is more spontaneous compare to larger particles. The nature and the electronic behavior of the passive film on ZnNi alloy nanoparticles were investigated in term of Mott-Schottky plot.

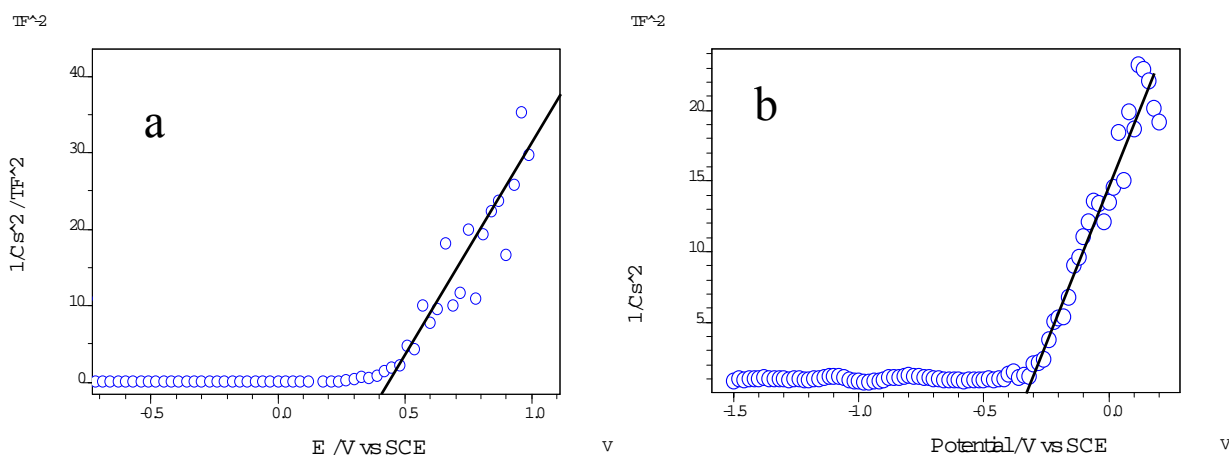


Fig. 5.1.6. Mott-Schottky plot of ZnNi alloy nanoparticles deposited from (a) aqueous solution into AAO, (b) Brij 78 into AAO. The curves were recorded in 0.4 M LiClO₄ with 1 kHz and 5 mV ac amplitude of sinusoidal voltage. The potentials were swept anodically. TF⁻² refers to Tetra (10¹²) Farad square.

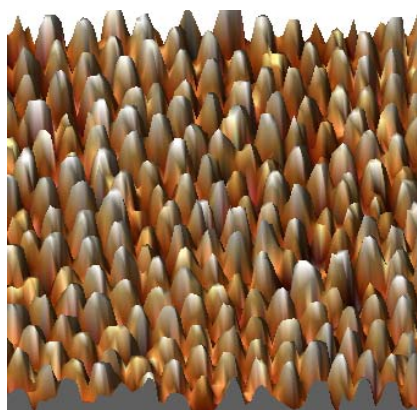
The capacitance measurements reveal the existence of a straight line with positive slope for potentials higher than 0.4 V in the sample prepared by electroreduction of ions from aqueous solution into AAO (a), and at potentials greater than -0.5 V in the sample deposited from Brij 78 (b). This means that the passive oxide film formed on ZnNi nanoparticles behaves as n-type semiconductor in these potential regions. The flatband potentials of the semiconductors are 0.38 V and -0.34 V vs SCE for Fig.5.1.6a and b respectively. The flatband potential was -0.65 V vs SCE in the film deposited from CTAB, therefore the flatband potential of ZnNi alloy nanoparticles shifted cathodically when the size of the particles is smaller. Similar tendency was observed on the corrosion potential.

From the polarization curves, it can be observed that the flatband potentials of ZnNi particles correspond in all cases to the potential regions in which oxide film covers the particles. After oxidation and passivation of particles, the electrode behaves like an n-type semiconductor. From the slope of the straight line of C^{-2} vs E plot, the donor density of state of the oxide layer can be calculated. But in the present case, the exact chemical formula of this film is unknown; it is difficult to find its dielectric constant; as consequence the donor density of state was not determined.

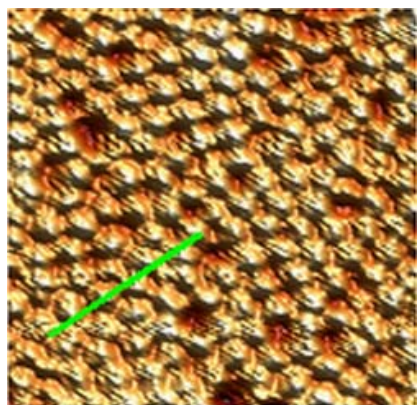
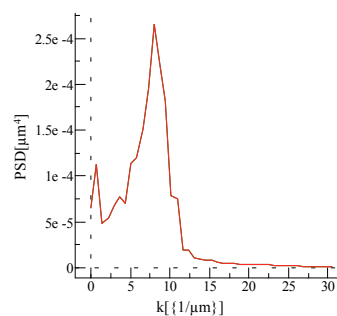
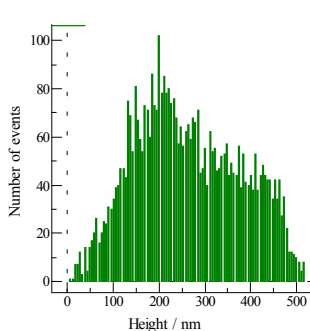
5.2 Preparation and characterization of NiCu alloy nanoparticles

5.2.1 Electrodeposition of NiCu alloy

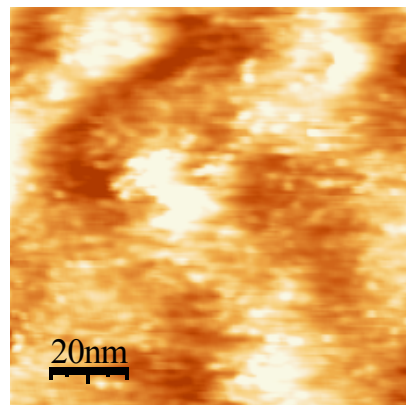
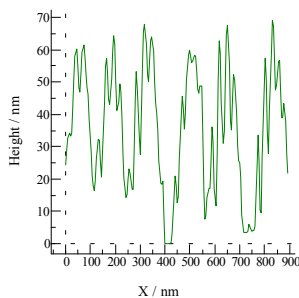
NiCu alloy nanoparticles were electrodeposited by single and double template techniques. The aqueous solution used for deposition and preparation of liquid crystal contains 0.025M CuSO_4 , 0.22 M NiSO_4 and 0.2 M H_3BO_3 (solution B). The redox potential of Cu^{2+}/Cu , 0.34 V vs SHE is more positive compared to Ni^{2+}/Ni , -0.23V vs SHE, copper ions would be reduced faster than nickel ions, the concentration of copper was smaller so that the rate of reduction should be limited by diffusion. For two metals to be co-deposited and produce an alloy, their individual deposition potential should be the same or nearly the same. When their redox potential differs by great amount, the only way to achieve deposition is by controlling the value of the activity. That is changing the respective concentrations can bring the potential into harmony [94]. The first liquid crystal mixture used for double template deposition contains 60 wt% Brij 78 and 40 wt% of the aqueous solution B. The second plating mixture is made of 50 wt % CTAB ionic surfactant and 50 wt% of the aqueous solution B. The CTAB plating mixture has a good electrical conductivity and the electrodeposition was also possible when the distance between the WE and the CE was several millimeter larger than in the case of Brij 78; that is without the micropositionner system.



a



b



c

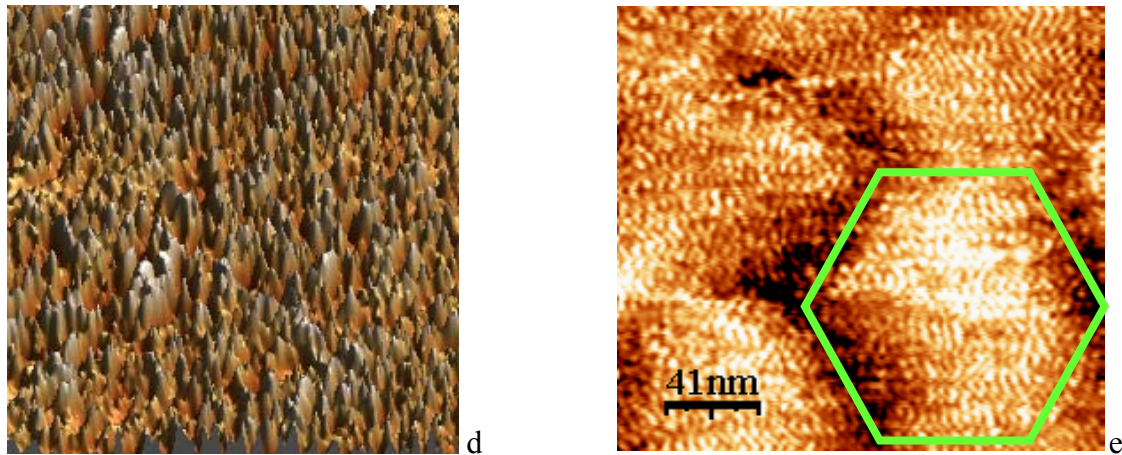


Fig. 5.2.1. Structure of NiCu alloy nanomaterials deposited (a) from aqueous solution into AAO, (b-c) in the presence of Brij 78 and (d-e) in the presence of CTAB. The current density was 2.5 mA/cm^2 and the quantities of electricity are 0.7C for (a), 0.4C for (b), (c) and (d). The STM images (c-d) were recorded with 40 mV bias voltage and filtered with 4 matrix point Gaussian filter. Samples (a-b) are $1.6 \times 1.6 \text{ }\mu\text{m}$ while (c) is $100 \times 100 \text{ nm}$. The number of particles and their length are displayed on the histogram of (a). The profile in (b) shows the subdivisions of the particles and the power spectra density gives the wavelength that corresponds to the repeat distances.

Fig. 5.2.1 compares the topography of NiCu alloy nanomaterials deposited with three plating mixtures. In (a) particles are well organized with constant periodicity between the fibers. The average thickness of this sample is 300 nm while the repeat distance deduced by Fourier transform (power spectra density) is about 125 nm . The histogram of particles distribution gives the number of particles and their specific length.

In (b), particles that grow from the bottom of the pore of AAO show many subdivisions caused by the columns of Brij 78. The profile carried out along the line confirms the subdivisions of the particles. The high resolution STM image (c) shows that the surface contains many small particles.

In the presence of CTAB liquid crystal with small diameter (d-e), the size of the particles is very small compared to the film deposited with Brij 78. The double periodicity appears clearly on (e) where the hexagon shows the pore of AAO; the material deposited in one pore consists of many small particles as expected from the principle of double template. Therefore, the double template process increases the specific area and may also improve the physical properties of the nanomaterial.

5.2.2 Polarization and corrosion of NiCu alloy nanoparticles

The polarization behavior of the alloy was investigated by anodic linear sweep voltammetry (ALSV) in 0.4 M LiClO₄ aqueous solution. In the case of alloy, ALSV will give various current peaks characteristic of chemical elements for single phase system, or phases of the alloy in the case of multi-phase system.

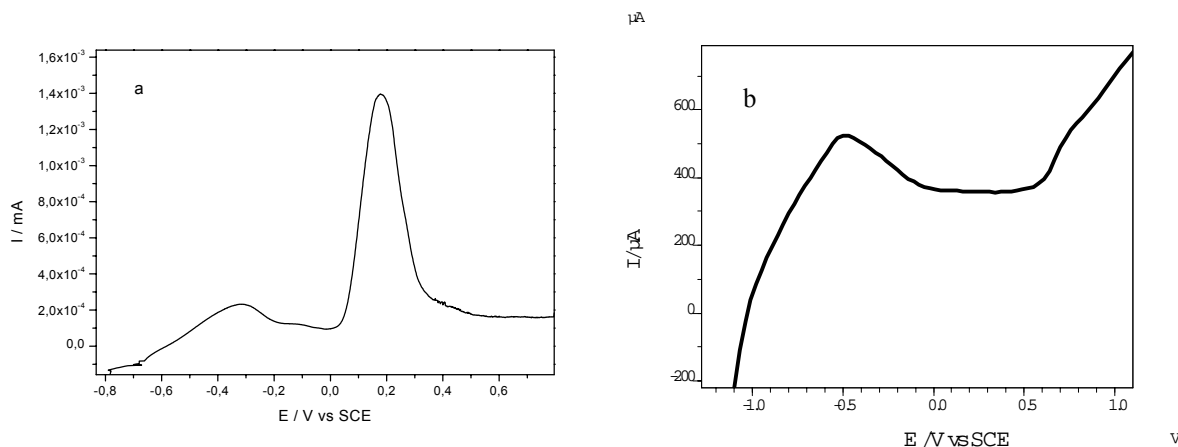


Fig. 5.2.2. Polarization behavior of (a) NiCu and (b) Ni nanoparticles in LiClO₄. Scan rate 3 mV/s.

The anodic linear voltammetry of NiCu and Ni nanoparticles in AAO (Fig. 5.2.2) under quasi-equilibrium conditions exhibits distinct active and passive regions. The departure of the active dissolution of the film is the point where the current begin to raise; in this region, an oxide film grows on the electrode surface. Passivation is reached when the oxide covers completely the electrode surface and the electrical conduction will be both electronically and ionically. The nickel film deposited under the same conditions as NiCu alloy shows only one oxidation peak (Fig. 5.2.2b) follow by passivation and a transpassive region. The active dissolution occurs in the potential range from -1 to -0.5 V followed by a passive region between -0.15 and 0.6 V and a transpassivation above 0.7V vs SCE. The polarization curve of copper film shows a similar behavior as the nickel film, only one oxidation peak was observed. The comparison between the voltammetry curves of nickel, copper and nickel-copper alloy leads to the following conclusion: the two anodic peaks observed on the polarization curve of Fig. 5.2.2a account for the existence of two metallic species on the surface. Furthermore, both Ni and Cu have the same structure (FCC), very close lattice constant (0.35 and 0.36nm, respectively) and similar atomic radii 0.25nm. These elements are continuously miscible and form a typical single-phase alloy for all composition and temperature [141a]. Therefore, the anodic peaks of the polarization curve of NiCu alloy cannot be assigned to phase transition. The passivation of the film occurs at potential

greater than 0.5 V vs SCE.

The behavior and performance of metals or alloy films is linked to their chemical composition, phase and surface morphology. Measurements such as polarization curves in form of Tafel plots have been particularly useful and elucidative in corrosion studies [142]. Application of Tafel equation can give important information such as the corrosion potential, E_{corr} , the corrosion current, I_{corr} , the anodic and cathodic Tafel slopes β_a , β_c respectively [119], which are function of the charge transfer coefficient R_p as shown by the Stern-Geary equation [143, 143a].

$$I_{\text{corr}} = \frac{\beta_a \beta_c}{2.203 R_p (\beta_a + \beta_c)} \quad (29)$$

The polarization curves of NiCu alloy nanoparticles recorded directly after immersion in 0.4 M LiClO_4 are shown in Fig. 5.2.3. In each case, two curves were recorded under the same experimental conditions to ensure that the observed corrosion potential is not due to experimental error. The aim is to see if the electrodeposition processes (used of aqueous solution or liquid crystal) will have influence on the corrosion parameters of the film. This was achieved by comparison of the corrosion curves of the same alloy prepared with different methods.

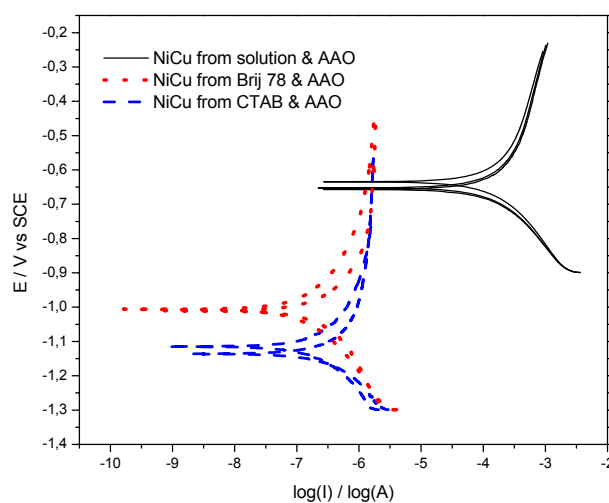


Fig. 5.2.3. Polarization curves of NiCu alloy nanomaterials in the pore of alumina membrane. The curves were recorded in 0.4 M LiClO_4 with a scan rate 3mV/s.

The anodic and cathodic branches of the polarization curves of NiCu have linear part and can be analyzed by the Tafel equation. The corrosion parameters were deduced from the experimental data using the “SoftCorr” Princeton electrochemical software.

Table 5. Corrosion parameters of NiCu alloy nanoparticles deposited from aqueous solution into AAO or from Brij 78 and CTAB into AAO.

	$E_{\text{corr}}/ \text{mV}$	$I_{\text{corr}}/ \mu\text{A}$	$\beta_a \times 10^{-3} \text{ V. dec}^{-1}$	$B_c \times 10^{-3} \text{ V. dec}^{-1}$
NiCu (solution)	-634.5	1.1	1096.0	340.0
NiCu (Brij 78)	-1000	379.4	798.6	895.1
NiCu (CTAB)	-1102	374.3	814.2	809.2

In general the corrosion potentials shift cathodically when the film is deposited from liquid crystal. As in zinc-nickel alloy films, the most negative corrosion potential is obtained with surfaces modified in the presence of CTAB liquid crystal. In order to check if this negative values are due to the presence of bromide ions or to the presence of surfactant in the pores of the metal film, the corrosion curves of the NiCu alloy deposited from aqueous solution into the pore of AAO were first recorded in 0.4 M LiClO_4 and secondly in a mixture of 0.4 M LiClO_4 and 0.05 M CTAB. It was observed that the E_{corr} shifted anodically to about 0.1 V vs SCE in the second mixture. The value of E_{corr} changed from about -604 to -520 mV vs SCE. Therefore the negative E_{corr} of the film deposited from CTAB is not due the presence of surfactant or bromide ions. It could be explained by the high reactivity associated to the small particles.

5.2.3 Impedance and Mott-schottky analysis of NiCu nanoparticles.

The electrical properties of NiCu nanoparticles such as interface capacitance and diffusion coefficient of lithium in the pore of the film were obtained by ac impedance measurement in the frequency range from 100 kHz to 5 Hz with 10 pt/decade and 5 mV ac amplitude of sinusoidal voltage. The resistance contributions from the material or from the interface polarization can be derived from EIS spectra analysis.

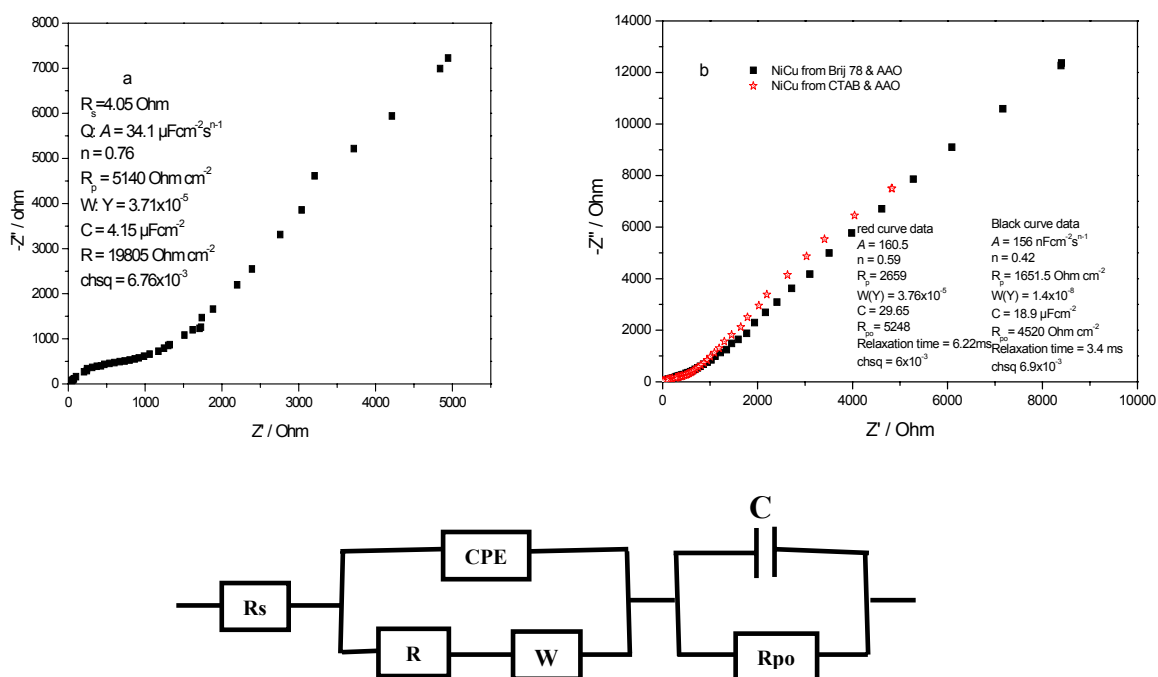


Fig. 5.2.4. Nyquist representation of the impedance data of NiCu (a) deposited from solution into AAO and (b) from liquid crystal into AAO. The electric parameters deduced by fitting with the equivalent circuit are represented in each graph. The curves were recorded in LiClO_4 from 100 kHz to 5 Hz, 10 pt/decade, 5 mV amplitude of ac voltage and -0.7 V vs SCE dc potential.

A depressed semicircle is observed in the high frequency region while a straight line appears at low frequency. This straight line is assigned to the diffusion in the pore present on the film. Recent study shows that the diffusion process is controlled by the diffusion of diluted oxygen from the solution to the electrode [125]. A solid state diffusion (or intercalation) of lithium ions into the pore of the material can also take place. The Nyquist-like diagrams of NiCu alloy nanoparticles are characteristic of porous electrode. The impedance spectra are in good agreement with AFM/ STM results.

The impedance data were fitted with the equivalent circuit of Fig. 5.2.4 using the ZsimDemo 3.2 simulation software operating with non linear least square algorithm. The high frequency loop accounts for two physical processes with very close time constant. The first time constant (R, C) could be assigned to the relaxation process in the NiCu / Al_2O_3 composite, or to the eventual oxide film and its dielectric properties. It can also be assigned to the space charge capacitance. Rehim [144] and Nigam [145] reported that a surface film could be considered to be a parallel circuit of resistor due to the ionic conduction in the oxide film, and a capacitor due

to its dielectric properties. The medium frequency time constant (Q , R_p) is attributed to the charge transfer resistance (R_p) and the double layer capacitance (Q) at the film electrolyte interface. The constant phase element was introduced to account for the non ideal behavior of the double layer capacitance and to minimize the fitting error.

The space charge capacitance is a very interesting parameter since it can give information about the behavior of a semiconductor electrode if the potential is changed. Electrochemical determination of this parameter is simple when the ac response of the space charge layer capacitance can be separated in frequency range from the other interfacial processes. Common impedance spectroscopy is a stationary technique [146] and this makes problem in such separation at different potentials. But potentiodynamic EIS decomposes ac responses of different interfacial processes during the electrode potential scan and this enables the acquisition of the space charge capacitance as function of potential in single experiment [147]. The Mott-Schottky plots of NiCu alloy nanomaterials recorded in LiClO_4 are shown on the following graph.

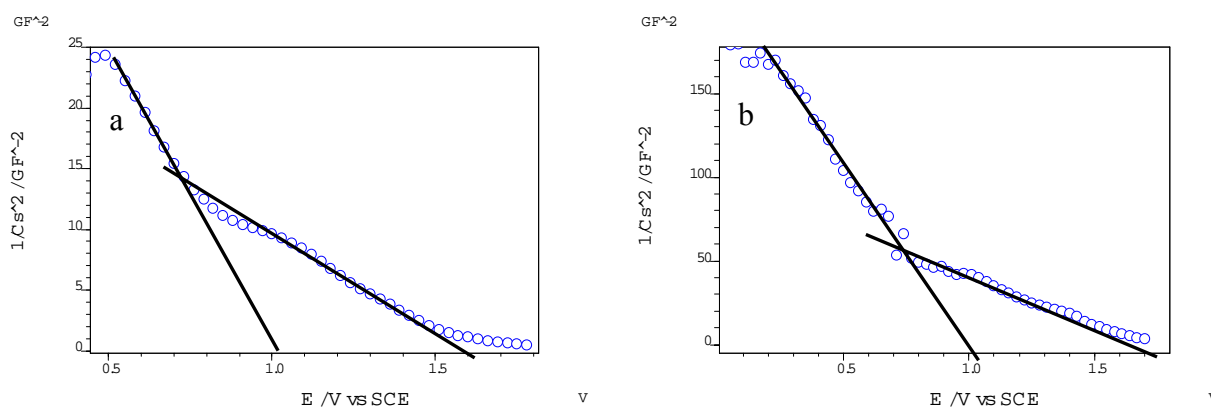


Fig. 5.2.5. Mott-Schottky plot of NiCu alloy nanomaterials deposited (a) from aqueous solution into AAO and (b) in the presence of CTAB liquid crystal. All spectra were recorded with potentiodynamic EIS mode at 1 kHz and 5 mV amplitude of sinusoidal voltage. GF^{-2} refer to Giga (10^9) Farad square.

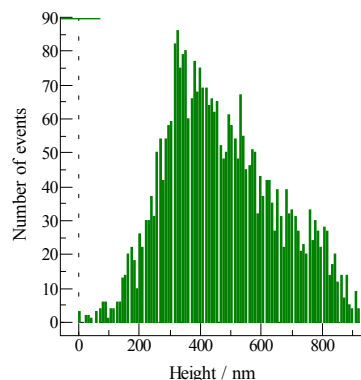
The Mott-Schottky plots of NiCu alloy nanofilm deposited from aqueous solution (a) and in the presence of CTAB (b) are shown in Fig. 5.2.5. In both cases, the plot has two different straight lines with negative slope; this account for p-type semiconductor behavior and the presence of a hetero junction. The slope of the lines decreases when the potentials tend to more positive values. This is due to the existence of large number of acceptor density at more positive

potential. From equation 19, the slope of the Schottky plot is proportional to the inverse of the acceptor or donor density. The variation of the slope can be explained by the increase in cation vacancies (acceptor) caused by the formation of passive film, when the potential is stepped anodically. The flat band potential ($E_{fb} = E - kT/q$ when $1/C_s^2 \sim 0$) deduced from the measurements are approximately 1 V and 1.67 V vs SCE for the lines. The existence of two flatband potentials may be due to the chemical composition of the nanofilm or to that of the passive film present on the particles. It shows the presence of p-p heterojunction and accounts for the change in the chemical status of the interface. The acceptor density of state could be deduced from the slope of each line if the dielectric constant of the material was known. Since the exact chemical formula of the passive oxide film formed on NiCu nanoparticles is not determined, it is difficult to find its dielectric constant. Therefore the value of the acceptor density of state cannot be calculated.

5.3 Electrodeposition and characterization of NiCo alloy nanoparticles.

5.3.1 Electrochemical deposition

The aqueous solution used to prepare NiCo alloy contains 0.11M nickel sulfate, 0.11M cobalt sulfate, 0.2M boric acid and 0.1 M ascorbic acid (solution C). Two other plating mixtures were used in order to compare the topography of the surface and control the size of the alloy nanoparticles. The first liquid crystal mixture contains 60 wt% Brij 78 and 40 wt% of the aqueous solution C. The second plating mixture contains 50 wt% CTAB and 50 wt% of the aqueous solution C. The following results were obtained after AFM / STM analysis.



a

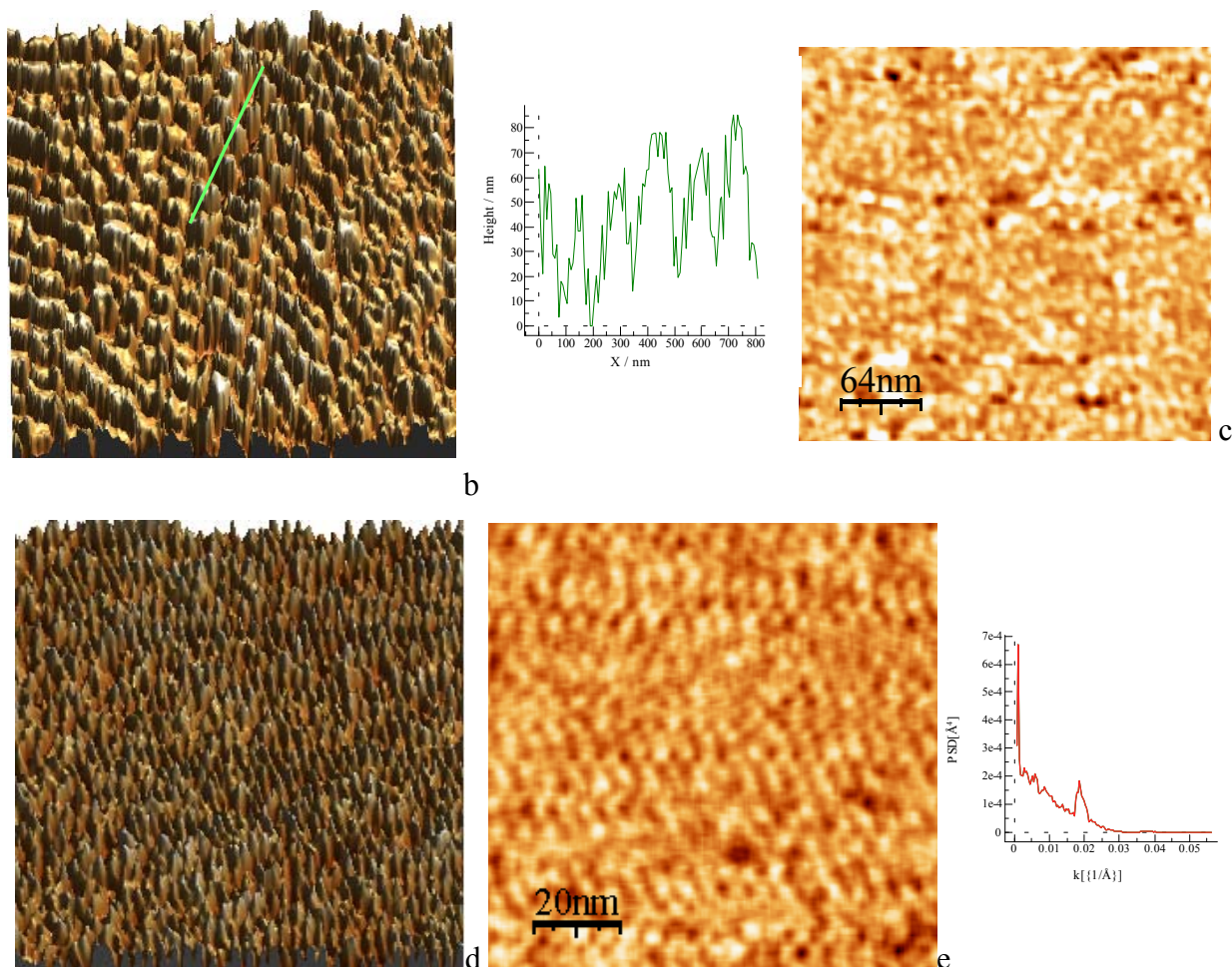


Fig. 5.3.1. AFM / STM micrograph of NiCo alloy nanomaterials deposited in the pore of alumina (a) with aqueous solution, (b-c) with Brij 78 and (d-e) with CTAB. The quantity of electricity is: 0.7 C for (a), 0.5C for (b-c). The scale is $1.6 \times 1.6 \mu\text{m}^2$ for a-b, and $200 \times 200 \text{ nm}^2$ for d. The STM images (c-e) were recorded with 50 mV bias voltage and Noises were removed with a 4-matrix point Gaussian filter.

As in the case of NiCu alloy, the size of the particles becomes smaller when the aqueous solution is replaced by the hexagonal phase of liquid crystal. Figure 5.3.1e depicts the 2D structure of the particles in the pores of AAO and show the expected nanostructure caused by the columns of CTAB. This STM micrograph reveals the hexagonal array of cylindrical pore and uniform particle size. 2D Fourier transform was used to determine the periodicity in the structure; the power spectra density of (e) shows a peak at the spatial wave number characteristic of the repeat distance. The pore-to-pore separation obtained by this method is 4.35 nm, value close to the repeat distance (3.5 nm) of the hexagonal phase of lyotropic CTAB mixture. This confirms the templating effect of the surfactant.

5.3.2 Polarization and Corrosion measurements

The constituents of NiCo mesoporous alloy were investigated by potentiodynamic stripping. This analysis was necessary to confirm the presence of the two elements in the film. It is interesting to recall that the composition of an electrodeposited alloy film may be different from that of the solution used for preparation. In some cases, the film contains only the metal that is easier to reduce. This behavior was observed during the preparation of nickel copper alloy nanomaterial where only copper was present in the film when its concentration in solution was high. Anodic linear voltammetry can be used to distinguish between the presences of one or more metallic species on the surface.

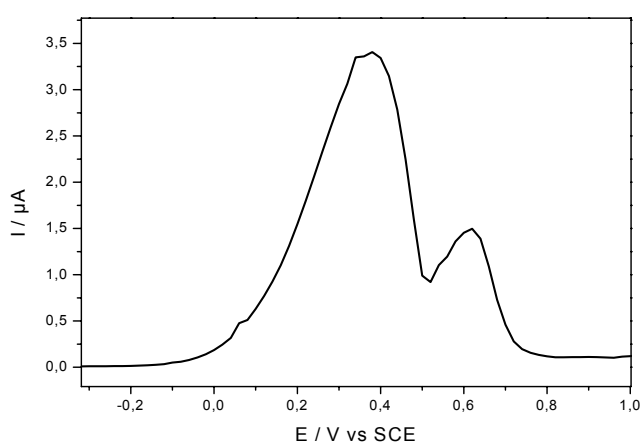


Fig. 5.3.2. Polarization curve of NiCo mesoporous alloy in LiClO_4 . The electrode area and the scan rate were 0.2 cm^2 and 3 mV/s , respectively.

The presence of two peaks potential in the polarization curve of NiCo film may account for the existence of two metallic species on the surface. The oxidation peaks are close since the difference in the redox potential of Ni^{2+}/Ni (-0.23 V vs SHE) and Co^{2+}/Co (-0.28 V vs SHE) is very small. The peaks may also account for the existence of two phases in the alloy. It is known that in the binary Ni-Co phase diagram, the mixture forms solid solutions with fcc structures in the range $\text{Co}/(\text{Ni} + \text{Co}) = 0-0.75$ at room temperature; and that the system transforms to an hcp structure in the range $\text{Co}/(\text{Ni} + \text{Co}) = 0.75-1$ [64]. Nickel and cobalt have a very close atomic radius (0.15 and 0.16 \AA respectively) and cobalt exist in both fcc and hcp structure; cobalt atom can easily take the position of nickel in the crystal structure and vice-versa. It has been reported that various phase separations (e.g. Co-rich Co-Ni hcp and Ni-rich Ni-Co fcc) tend to occur even in the composition range where fcc structures are normally formed [64]. Therefore, the presence

of two peaks in the polarization curve of this alloy may account for the selective dissolution of its elements or for the existence of two phases.

The corrosion of nickel cobalt alloy nanomaterials was also investigated in 0.4 M LiClO₄. The following graph shows the comparison between the corrosion curves of films deposited with different plating mixtures.

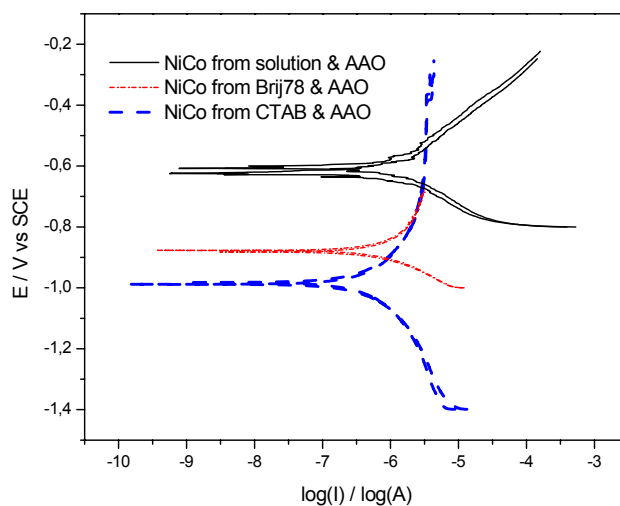


Fig. 5.3.3. Corrosion curves of NiCo alloy nanomaterials in LiClO₄. Scan rate 3 mV/s.

Both anodic and cathodic branch have linear portion but these regions didn't extend over one decade on log I axis; therefore the kinetic parameters deduced by fitting with corrosion software are approximate values.

Table 6: kinetic parameters of NiCo alloy mesoporous film in LiClO₄

	$E_{\text{corr}} / \text{mV}$	$I_{\text{corr}} / \mu\text{A}$	$\beta_a \times 10^{-3} \text{ V.dec}^{-1}$	$\beta_c \times 10^{-3} \text{ V.dec}^{-1}$
NiCo (Solution)	-604.4	18.7	151.6	105.4
NiCo (Brij 78)	-876.1	0.34	564.6	85.1
NiCo (CTAB)	-993.2	0.19	557.4	395.3

The corrosion potential is more negative when the film is prepared from CTAB liquid crystal mixture. The film deposited from CTAB mixture consists of very small particles; its specific area should be larger than that of the surface prepared by aqueous solution or from Brij 78. Yamauchi et al. [64] observed anomalous behavior during the electroless synthesis of NiCo alloy

from lyotropic liquid crystalline (Brij56) media. That is the suppressed deposition of nickel leading to higher cobalt content irrespective of the nature of the plating media such as aqueous solution or solution containing highly concentrated surfactants additive. In any case the composition of the product can be varied by the compositions of the plating bath even under the presence of highly concentrated surfactants [64]. This suggests that the observed displacement of the corrosion potential to negative values when the material is prepared in the presence of surfactant cannot be assigned to an eventual change of alloy composition associated to the plating mixture.

In summary the cathodic shift of the corrosion potential accounts for the high reactivity associated to the size of particles.

5.3.3 Impedance and Mott-Schottky analysis of NiCo nanoparticles.

The electrical behavior and interfacial process that occur on the NiCo alloy nanoparticles in aqueous solution were investigated by impedance spectroscopy. The diffusion coefficient, resistances and capacitances contribution from different phases were deduced from the ac response by fitting the result with an appropriated equivalent circuit. The impedance curves were recorded in LiClO_4 in the frequency range from 100 kHz to 5 Hz with 5 mV ac amplitudes of sinusoidal voltage. The electrode dc potential was fixed at -0.5 V vs SCE to avoid any oxidation of the film during measurement. It can be observed from the potentiodynamic curve that a

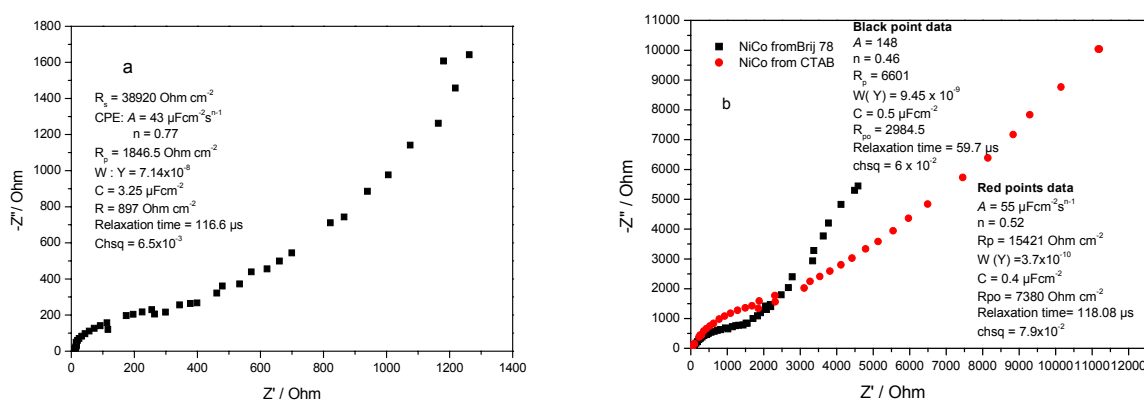


Fig. 5.3.4. Nyquist representation of the impedance data of NiCo (a) deposited from solution into AAO and (b) from liquid crystal into AAO. The electric parameters deduced by fitting with the equivalent circuit (similar to that of Fig. 5.1.4) are represented in each graph. The curves were recorded in LiClO_4 from 100 kHz to 5 Hz, 10 pt/decade, 5 mV ac amplitudes and -0.5 V vs SCE dc potential.

potential greater than -0.2 V may oxidize the particles. During impedance measurement, a dc potential is necessary to maintain the electrode in steady state and ensure the linear response of the ac signal.

The complex-plane representation of the impedance data of NiCo alloy nanomaterials shows a semicircle at high frequency and a straight line at low frequency. The high frequency data account for the double layer capacitance and the space charge layer charging; or for the charging of double layer capacitance and the relaxation process that may occur in NiCo / Al_2O_3 composite. The diffusion of dilute oxygen or lithium ions in the pore of the material appears as a straight line in the low frequency region. The impedance data were fitted with the same model as in Fig. 5.1.4. The inserted values in each graph show the numerical data that correspond to each element of the model. In all cases the relaxation time constant is in microsecond, this indicated that the charging of the space charge region or the relaxation of the NiCo / Al_2O_3 composite is a very fast process. This could explain why the two semicircles of the high and medium frequency cannot be clearly separate in the Nyquist representation.

The electronic properties of NiCo alloy nanoparticles in LiClO_4 were studied by capacitance measurement in the form of Mott-Schottky plot. The space charge capacitance of the NiCo film was obtained by potentiodynamic impedance spectroscopy. The Schottky plots were recorded directly after the preparation of the film, without any other treatment that can oxidize the particles. The aim is to study the electronic properties of particles cover by a natural oxide layer. The MS plots of NiCo alloy nanoparticles deposited from aqueous solution into AAO, and with the CTAB liquid crystal are shown on Fig. 5.3.5.

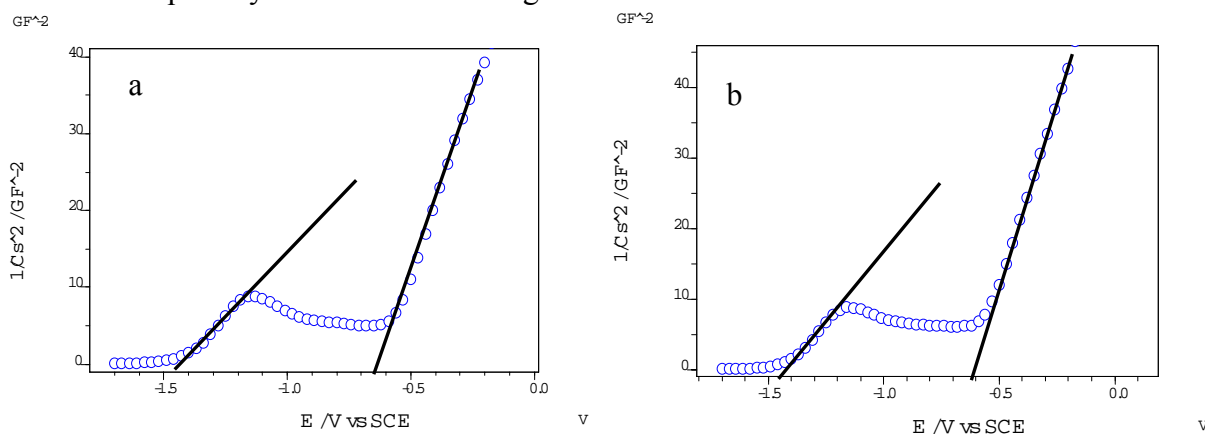


Fig. 5.3.5. Mott-Schottky plot of NiCo alloy nanofilm recorded in 0.4 M LiClO_4 : (a) film deposited from aqueous solution, (b) film prepared in the presence of CTAB. The spectra were recorded in Potentiodynamic EIS mode with 1 kHz and 5 mV amplitude of sinusoidal voltage. GF^{-2} refer to Giga (10^9) Farad square.

The data of each graph in Fig. 5.3.5 fit two straight lines with positive slope; the films behave as an n-type semiconductor. Mott-Schottky plot of NiCo deposited from solution is in total agreement with that of sample prepared in the presence of CTAB. In both cases, the intercept of the line with the x-axis at the lower potential region indicates a flatband potential of -1.5 V vs SCE. At more positive potential, another straight line appears with a flatband potential of -0.65 V vs SCE. The slope of the Schottky plot at more positive potential is greater than that at lower potential. This suggests that the donor density of states decreases gradually. Moreover, the passive film on NiCo particles could contain two oxides with different donor density of state; both components form an n-n heterojunction.

It is interesting to understand the origin of the semiconductivity and the presence of dopants with different density of state when NiCo, NiCu, ZnNi alloy nanofilms are analyzed. In general, a thin oxide film may exist on the surface of the particles and could account for the observed semi-conductivity. Furthermore, the nanoparticles prepared in the described experimental conditions could be made of oxide or hydroxide of the corresponding metal; or may undergo rapid passivation in air or in LiClO_4 . In these cases, the dopants in the semiconductor passive film could be assigned to oxygen vacancies and cation interstitials that are donors. Mott-Schottky analysis of the passive film on metals surface reveals that the barrier layer is best described as a non-uniformly doped, degenerate defect semiconductor. The dopants (oxygen vacancies and cation interstitials [donors] and/or cation vacancies [acceptors]) are present in high concentration $> 10^{21}/\text{cm}^3$ [133].

5.4 Discussion

The present chapter describes a method of surface modification with alloy nanomaterials. Two different techniques were used:

- the so called one template deposition where the alloy nanorods are deposited from aqueous solution within the pore of alumina membrane on aluminum. The aluminum surface modified in this condition consists of many alloy nanorods with regular periodicity of about 125 nm. The length of this self-organized alloy nanomaterials can reach $1\mu\text{m}$ or more if the electric parameters are controlled accurately.
- the second technique termed double template deposition is the combination of the hexagonal phase of lyotropic liquid crystal together with the porous alumina membrane for deposition. A non-ionic liquid crystal (Brij 78) having larger columns diameters and an ionic liquid crystal

(CTAB) with smaller columns diameters were used. This choice was very useful to understand the influence of the diameter of liquid crystal columns on the size of the resulting nanoparticles, and the impact of the electronic behavior (ionic or non-ionic) of the surfactant on the electrodeposition processes. The Ohmic resistance of the non-ionic liquid crystal is higher than that of ionic surfactant. As results, the electrochemical process is difficult with the non-ionic surfactant mixture. Consequently, a micropositionner machine should be used to reduce the distance between the working and the counter electrodes; doing this will lower the Ohmic drop and facilitate the electrical conduction. On the contrary, the ionic surfactant mixture has a good conductivity and the use of a micropositionner during deposition is not absolutely necessary. On the other hand, the size of the particles deposited with surfactant depends on the diameter of the columns of liquid crystal. That is, surfactant with smaller columns gives particles with very small size.

The influence of the size of particle on the electrochemical behavior of the film was investigated by polarization measurement. In general, the corrosion potential of the alloys nanomaterials shifted to more negative values when the size of the particles becomes very small. A comparison with the electrochemical standard potential series shows that an element is a strongly reducing agent when its standard potential is very negative. Therefore, the aptitude of the material to supply electrons increases when the film is highly porous. The observation accounts for the higher reactivity associated to the increase of the specific area of the film. It is known that in nanostructured materials, the large surface-to-volume ratio and the variation in geometry and electronic structure have a dramatic effect on transport and catalytic properties. The reactivity of small clusters has been found to change by orders of magnitude when the cluster size was varied by only a few atoms [148].

It may also come from the deposition processes such as the introduction of surfactant in one case and the aqueous solution in the other case. The dynamic and kinetic (viscosity of the plating mixture and the diffusion coefficient of ions) processes that govern the nucleation of particles are not the same in each mixture; this change may induce the formation of amorphous and/or crystalline material and could influence the corrosion potential.

The impedance spectra are also affected by similar size effect. The shape of the impedance curve is the same, but the values of the real and imaginary part of the impedance data are higher for samples deposited from liquid crystal. That is, the impedance magnitude is higher in samples deposited from the hexagonal phase of liquid crystal compared to that deposited from aqueous solution.

A close look to the anodic linear voltammetry results and the polarization curves shows that the active dissolution of alloys particles takes place, in most cases, at a potential greater (more anodic) than the corrosion potential. This is in good agreement with theory; the relation between the pitting potential (potential at which active dissolution or oxidation begins) and the corrosion potential of a metal is as follow [120].

$$E_p = E_{\text{corr}} + \Phi + \eta \quad (30)$$

Where Φ is the potential induced by the migration of ions and η the polarization needed to reach the critical pit initiation current density.

The electronic property of the alloy nanoparticles was also studied. All alloy particles prepared in the described experimental conditions behave like a semiconductor in LiClO_4 aqueous solution. NiCu alloy nanomaterials have p-type semiconductor behavior while ZnNi and NiCo are n-type. In some cases (NiCu and NiCo materials), two straight lines appear on the Mott-Schottky plots. This suggests the existence of two different types of semiconductor that form a hetero-junction. Similar behavior was not observed on the ZnNi alloy; therefore, the two lines and two flatband potential could be associated to the chemical composition of the films. The semiconductor behavior of the alloy is attributed to the formation of a passive film on the particles. Also, the alloy nanomaterials prepared in the given experimental conditions may consist of oxide of the corresponding metals or may undergo rapid passivation in air or in LiClO_4 . According to Davenport et al. [149] the barrier layer on metal surface is a defective structure containing high concentrations of point defects. Because the dopants (oxygen vacancies and metal interstitials [donor] and cation vacancies [acceptors]) are present at high concentration, the barrier layer is best described as a non-uniformly doped, degenerate defect semiconductor [133,150,151]. Moreover, the passive films on metal surfaces generally comprise two layers: a defective barrier layer that grows directly into the metal and a precipitated outer layer that incorporates species from the solution [133]. The existence of these two layers and the chemical composition of the surfaces may also account for the presence of two flatband potentials and two donors (NiCo film) or acceptors (NiCu film) density of state observed on the Mott-Schottky plots.

6 Summary

The present work describes the electrochemical deposition and characterization of metallic and alloy nanomaterial by single and double template self-organization.

Thin aluminum oxide was prepared on aluminum by double anodization of the aluminum foil in 0.3 M oxalic acid. The influence of the electrolyte (oxalic acid) temperature on the structure of alumina membrane was studied. Samples were anodized at 0, 10, 20, 30 and 40°C; in each case, atomic force microscope and impedance spectroscopy were used respectively to analyze the topography and study the electron transfer across the thin membrane.

Self-organized hexagonal nanopores were obtained on aluminum surface at each temperature. The pore homogeneity decreases when the anodization temperature increases. From impedance measurement, it was observed that the polarization resistance of the membrane increases with the anodization temperature. The membrane anodized at 10 °C had a long-range organization of hexagonal pores with uniform diameter. The average thickness and the diameter at half-height of the alumina anodized at this temperature were about 50 nm and 70 nm, respectively. The polarization resistance of the electrode material covered by this membrane was lower compared to that anodized at higher temperature. This allows electron to tunnel across the barrier layer of the alumina membrane during deposition.

The optimal electrochemical conditions to achieve homogeneous deposition of metallic particles in the pore of this membrane with intact barrier layer were investigated. The current density and the quantity of electricity were changed during deposition, and the topography of the films analyzed in each case by AFM. As a result, high current density and short deposition time were necessary for electrons to tunnel across the barrier layer between the porous alumina layer and the aluminum substrate. Under these conditions, highly ordered cobalt and alloy nanomaterials were deposited from aqueous solution into the pore of alumina membrane with intact barrier layer. Cobalt, zinc-nickel, nickel-cobalt and nickel-copper alloy nanorods of about 1.2 μm in length with a periodicity (center-to center spacing between two close particles) of about 125 nm were grown in the pores of aluminum oxide with a quantity of electricity close to 0.9 C. Recently, it was reported that uniform filling of the pores of alumina membranes with the barrier layer cannot be achieved using direct current electrodeposition. In the present work, it was observed that the porous alumina membrane with intact barrier layer could be polarized when it is thin enough and uniform deposition of material in the pore can be achieved with direct current.

Electrochemical deposition using a thin AAO membrane with the barrier layer offers many advantages:

- It is possible to obtain homogenous nucleation of particles in the pores of AAO using direct current. With a thick membrane, an alternative or pulse current should be used for deposition.
- There is an important gain in time and reagent. The preparation of thin AAO membrane takes place in very short time (30 min x 2). There is no need of extra chemicals to separate the AAO from the aluminum foil or to remove the under barrier layer. In the preparation of nanomaterial using thick alumina, the removal of the membrane after deposition leads to the partial oxidation of the material.
- The nanorods are rigid, perpendicular to the surface and have constant periodicity: the elimination of the alumina after deposition induces the lost of the periodicity (center-to-center spacing) between the nanorods.
- Fibers of 1.4 μ m in height can be prepared within a thin AAO membrane by accurate control of the electric charge during deposition. The material is also easy to handle and can be extend to larger scale.

In order to control the size of the particles and increase the specific area of the electrodeposited films, the principle of the so-called double template deposition was used. The metallic ions were dissolved in aqueous solution and this mixture was used to prepare the hexagonal phase of lyotropic liquid crystal. The liquid crystal mixture was melted on the alumina membrane and the metallic ions dissolve in the phase were reduced galvanostatically. The diameter of the columns of liquid crystal was less than 10 nm, very small compared to that of the pore of alumina close to 70 nm. Therefore, many columns of liquid crystal went into one pore of alumina; after deposition and removal of the surfactant, the nanorods showed many subdivisions. Surfaces modified by double template process displayed two periodicities. The first due to the pores of alumina that direct the nanorods from the bottom to the top of the pore, and the second caused by the columns of surfactant that divide the nanorods into many particles. Two surfactants with different molecular size were investigated; the hexagonal phase of a non ionic surfactant (Brij 78) with a diameter of columns close to 8 nm and that of an ionic surfactant (CTAB) with smaller ($\Phi \sim 4$ nm) columns. Analysis revealed that the size of metal or alloy nanoparticles was significantly reduced when the liquid crystal with small columns was introduced. The film deposited from CTAB consisted of very small nanoparticles. The topography of ZnNi, NiCo, NiCu alloys nanomaterial deposited from different plating mixture

(aqueous solution, Brij 78 or CTAB liquid crystal) was compared and it was deduced that the size of nanoparticles can be controlled by appropriated chose of surfactant molecules.

Different electrochemical techniques such as impedance spectroscopy, anodic linear voltammetry, corrosion and semiconductivity were used to characterize the films.

The Nyquist representation of the impedance data of the mesoporous film showed in all cases, a semi-circle at high frequency and a straight line of about 45° with respect to the real axis at low frequency. Such curve shape was characteristic of porous electrode and of electrode processes under diffusion and charge transfer control. The diffusion observed in this case was assigned to the solid-state intercalation of lithium ions into the pores of the material or to the diffusion of open-air oxygen into the pore of the material. The capacitance, the resistance and the diffusion coefficients of open-air oxygen or lithium ions in the pore of the film were deduced from impedance spectra. The impedance magnitude was higher in materials deposited in the presence of surfactant compared to those prepared from aqueous solution. This observation was also assigned to size effect. In general, the Nyquist representation of the impedance data was in agreement with the AFM / STM results and confirmed the porosity of the films.

The presence of thin film of single elements such as cobalt or alloy (ZnNi, NiCo, NiCu) on the aluminum surface was confirmed by anodic linear sweep voltammetry. The polarization curves gave various peaks characteristic of metal oxidation in the case of single element (Cobalt) or phase transition during alloy oxidation in the case of multiphase alloy such as ZnNi. Moreover, the corrosion potential of cobalt and alloy nanomaterial shifted two negative values when the materials were prepared in the presence of surfactant. AFM / STM showed that the samples deposited in the presence of surfactant contained particles with very small size. Therefore, the displacement of the corrosion potential toward negative value was assigned to the high reactivity associated to particles with small size, or to the film formation process.

The space charge capacitance of the cobalt and alloy nanomaterials was measured in lithium perchlorate by potentiodynamic electrochemical impedance spectroscopy. The Mott-Schottky analysis of the space charge capacitance data revealed that the films of metal or alloy nanomaterials have semiconductor behavior. The type of semiconductor depended on the chemical composition of the nanofilms. This property was interpreted as the consequence of a rapid passivation of the materials in air or in the solution; since it is well known that the passive films of metal and alloy have semiconductor properties with high dopants concentration.

7. References

- [1] M. P. Holsapple, W. H. Farland, T. D. Landry, N. A. Monteiro-Riviere, J. M. Carter, N. J. Walker, K. V. Thomas, *Toxicol. Sci.* 88(1) (2005) 12.
- [2] K. Kulinowski, *Bull. Sci. Tech. Soc* 24(1) (2004) 13.
- [3] E. F. Einsiedel, *Bull. Sci. Tech. Soc.* 24(1) (2004) 28.
- [4] C. N. R. Rao, A. Müller, A. K. Cheetham “ The Chemistry of Nanomaterials: synthesis, properties and applications” Vol. 1, WILEY-VCH verlag, GmbH & Co, (2004) p285.
- [5] C. R. Martin, *Science* 266 (1994) 1961.
- [6] E. Chen, S. Tehrani, T. Zhu, M. Durlam, H. Goronkin, *J. Appl. Phys.* 81 (1997) 3992.
- [7] W. J. Gallagher, S. S. P. Parkin, X. Bian, A. Marley, K. Roche, R. Rishton, C. Jahnes, T. Shaw, G. Xiao, *J. Appl. Phys.* 81 (1997) 3741.
- [8] W. Liang, M. Zhou, *Nano. Lett.* 5(10) (2005) 2039.
- [9] P. A. Kossyrev, A. Yin, S. G. Cloutier, D. A. Cardimona, D. Huang, P. M. Alising, J. M. Xu, *Nano. Lett.* 5 (10) (2005) 1978.
- [10] E. Ozbay, *Science* 311 (2006) 189.
- [11] M. M. J. Treacy, T. W. Ebbesen, J. M. Gibson, *Nature* 38 (1996) 678.
- [12] B. C. Satishkumar, E. M. Vogl, A. Govindaraj, C. N. R. Rao, *J. Phys.* D29 (1996) 3173.
- [13] P.G. Collins, M. S. Arnold, P. Avouris, *Science* 292 (2001) 706.
- [14] A. Bachtold, P. Hadley, T. Nakanishi, C. Dekker, *Science* 294 (2001) 1317.
- [15] a) J. Hanes, J. L. Cleland, R. Langer, *Adv. Drug. Delivery Rev.* 28 (1997) 97.
b) I. F. Cheng, C. R. Martin, *Anal. Chem.* 60 (1988) 2163.
c) V. P. Menon, C. R. Martin, *Anal. Chem.* 67 (1995) 1920.
d) L. Wang, K. Yu-Zhang, A. Metrot, P. Bonhomme, M. Troyon, *Thin Solid films* 288 (1996) 86.
e) K. Uosaki, K. Okazaki, H. Kita, *Anal. Chem.* 62 (1990) 652.
- [16] S. Egger, A. Ilie, Y. Fu, J. Chongsathien, D-J. Kang, M. E. Welland, *Nano. Lett.* 5(1) (2005) 15.
- [17] G. B. Ji, S. L. Tang, S. K. Ren, F. M. Zhang, B. X. Gu, Y. W. Du, *J. Cryst. Growth* 270 (2004) 156.
- [18] P. S. Khiew, S. Radiman, N. M. Huang, M. S. Ahamd, *J. Cryst. Growth* 268 (2004) 227.
- [19] I. Manners, *science* 294 (2001) 1664.
- [20] D. A. Doshi, A. Gibaud, V. Goletto, M. Lu, H. Gerung, B. Ocko, S. M. Han, C. J. Brinker, *J. Am. Chem. Soc.* 125 (2003) 11646.

-
- [21] I. Arslan, T. J. V. Yates, N. D. Browning, P. A. Midgley, *Science* 309 (2005) 2195.
- [22] J. Choi, G. Sauer, P. Göring, K. Nielsch, R. B. Wehrspohn, U. Gösele, *J. Mater. Chem.* 13 (2003) 1100.
- [23] Ö. Dag, O. Samarskaya, N. Coombs, G. A. Ozin, *J. Mater. Chem.* 13 (2003) 328.
- [24] J. C. Hulthen, C. R. Martin, *J. Mater. Chem.* 7(7) (1997) 1075.
- [25] Y. Pia, H. Lim, J. Y. Chang, W. Y. Lee, H. Kim, *Electrochim. Acta* 50 (2005) 2997.
- [26] H. Masuda, K. Fukuda, *Science* 268 (1995) 1466.
- [27] H. Asoh, K. Nishio, M. Nakao, T. Tamamura, H. Masuda, *J. Electrochem. Soc.* 148(4) (2001) B152.
- [28] P. Bocchetta, C. Sunseri, R. Masi, S. Piazza, F. D. Quarto, *Mater. Sci. Eng. C23* (2003) 1021.
- [29] Z. Wang, Y. K. Su, H. L. Li, *Appl. Phys.* A74 (2002) 563.
- [30] J. Qin, J. Nogués, M. Mikhaylova, A. Roig, J. S. Muñoz, M. Muhammed, *Chem. Mater.* 17 (2005) 1829.
- [31] Y. Z. Jin, Y. Q. Zhu, K. Brigatti, H. W. Kroto, D. R. M. Walton, *Appl. Phys.* A77 (2003) 113.
- [32] F. D. Bouchiat, C. Champeaux, H. S. Nagaraja, F. Rossignol, N. Lory, A. Catherinot, P. Blondy, D. Cros, *Thin Solid Films* 453-454 (2004) 296.
- [33] C. Yoon, J. S. Suh, *Bull. Korean Chem. Soc.* 23(11) (2002) 1519.
- [34] C. J. Brumlik, V. P. Menon, C. R. Martin, *J. Mater. Res.* 9 (1994) 1174.
- [35] X. Jinxia, X. Huang, G. Xie, Y. Fang, D. Liu, *Mater. Res. Bull.* 39 (2004) 811.
- [36] S. Ram, S. Rana, *Curr. Sci.* 77(1) (1999) 1530.
- [37] Z. A. Hu, H. Wu, X. Shang, R.-J. Lü, H.-L. Li, *Mater. Res. Bull.* 41 (2006) 1045.
- [37a] M. Aslam, R. Bhojbe, N. Alem, S. Donthu, V. P. Dravid, *J. Appl. Phys.* 98 (2005) 074311.
- [38] Nicholas Richard Boldero Coleman, Phd Thesis, University of Southampton, U K (1999) pp 12-33.
- [39] Gregor Cevc, *Phospholipids Handbook*, Marcel Dekker Inc; New York.-Basel-Hong Kong (1993) P 403.
- [40] G. J. Halder, C. J. Kepert, B. Moubaraki, K. S. Murray, J. D. Cashion, *Science* 298 (2002) 1762.
- [41] J. M. Elliott, G. S. Attard, P. N. Bartlett, J. R. Owen, N. Ryan, G. Singh, *J. New Mater. Electrochem. Sys.* 2 (1999) 239.
- [42] P. Alexandridis, U. Olsson, B. Lindman, *Langmuir* 14(1998) 2627.
- [43] J. R. Owen "Architecture of mesoporous electrode materials" University of Southampton
-

SO 17 1 BJ. UK.

- [44] L. Wang, X. Chen, Y. Chai, J. Hao, Z. Sui, W. Zhang, Z. Sun, *Chem. Commun.* (2004) 2840.
- [45] G. S. Attard, P. N. Bartlett, N. R. B. Coleman, J. M. Elliott, J. R. Owen, *Langmuir* 14 (1998) 7340.
- [46] S. S. Funari, G. Rapp, *J. Phys. Chem. B* 101 (1997) 732.
- [47] I. Nandhakumar, J. M. Elliott, G. S. Attard, *Chem. Mater.* 13 (2001) 3840.
- [48] P. N. Bartlett, B. Gollas, S. Guerin, J. Marwan, *Phys. Chem. Chem. Phys.* 4 (2002) 3845.
- [49] P. N. Bartlett, J. Marwan, *Microporous Mesoporous Mater.* 62 (2003) 73.
- [50] D. J. Mitchell, G. J. T. Tiddy, L. Waring, T. Bostock, M. P. McDonald, *J. Chem. Soc. Faraday Trans.* 179 (1983) 975.
- [51] P. Sakya, J. M. Seddon, R. H. Templer, R. J. Mirkin, G. J. T. Tiddy, *Langmuir* 13 (1997) 3706.
- [52] Ö. Dag, S. Alayoglu, C. Tura, Ö. Celik, *Chem. Mater.* 15 (2003) 2711.
- [53] Marcellin Fotsing Kamte, Phd Thesis, Martin-Luther Universität Halle-Wittenberg, (2004)
- [54] J. M. Elliott, G. S. Attard, P. N. Bartlett, N. R. B. Coleman, D. A. S. Merckel, J. R. Owen, *Chem. Mater.* 11 (1999) 3602.
- [55] J. S. Attard, S. A. A. Leclerc, S. Maniguet, A. E. Russel, I Nandhakumar, B. R. Gollas, P. N. Bartlett, *Microporous Mesoporous Mater.* 44-45 (2001) 159.
- [56] P. N. Bartlett, J. Marwan, *Chem. Mater* 15 (2003) 2962.
- [57] P. A. Nelson, J. M. Elliott, G. S. Attard, J. R. Owen, *Chem. Mater.* 14 (2002) 524.
- [58] J. K. Zhao, X. Chen, L. Y. Jiao, Y. C. Chai, G. D. Zhang, J. Liu, *Chem. Lett.* 33(7) (2004) 842.
- [59] A. H. Whitehead, J. M. Elliott, J. R. Owen, G. S. Attard, *Chem. Commun.* (1999) 331.
- [60] P. N. Bartlett, P. N. Birkin, M. A. Ghanem, P. de Groot, M. Sawicki, *J. Electrochem. Soc.* 148 (2) (2001) C119.
- [61] S. J. Im, W. S. Chae, S. W. Lee, Y. R. Kim, *Mater. Res. Bull.* 41 (2006) 899.
- [62] H. Luo, J. Zhang, Y. Yan, *Chem. Mater.* 15 (2003) 3769.
- [63] P. S. Khiew, S. Radiman, N. M. Huang, M. S. Ahamd, *J. Cryst. Growth* 268 (2004) 227.
- [64] Y. Yamauchi, T. Yokoshima, T. Momma, T. Osaka, K. Kuroda, *J. Mater. Chem.* 14 (2004) 2935.
- [65] Rebeca Howland and Lisa Benater, "A practical guide to scanning probe Microscopy". (1997) pp1-12.
- [66] Bharat Bhushan, Harold Fuchs, Sumio Hosaka, "Applied scanning probe methods"

-
- Springer, Berlin-Heidelberg-New York (2004) pp 292-295.
- [67] F. Mansfield, L. T. Han, C. C. Lee, C. Chen, G. Zhang, H. Xiao, *Corros. Sci.* 39 (1997) 255.
- [68] John R. Scully, David C. Silverman, Martin W. Kendig, "Electrochemical Impedance; Analysis and Interpretation", ASTM, Philadelphia (1993) pp 10-43.
- [69] Daria Vladikova, "The technique of differential impedance analysis part I: basic of the impedance spectroscopy", Proceeding of the international workshop, Sofia, 4-9 Sept (2004).
- [70] R. Kern, R. Sastrawan, J. Ferber, R. Stangl, J. Luther, *Electrochim. Acta* 47 (2002) 4213.
- [71] Bryant W. Rossiter, John F. Hamilton, "Physical methods of chemistry", 2nd Ed, Vol II, Wiley & Sons, New York-Chichester-Brisbane-Toronto-Singapore, (1986) pp 345-374.
- [72] Electrochemical Impedance spectroscopy, Primer, Copyright (2005), Gamry Instrument, www.gamry.com
- [73] Basic of electrochemical impedance spectroscopy; Princeton Applied Research application note AC-1 . www.princetonappliedresearch.com/products/appnotes.cfm
- [74] A. Thursfield, S. Brosda, C. Pliangos, T. Schober, C. G. Vayenas, *Electrochim. Acta* 48 (2003) 3779.
- [75] S. Vorrey, D. Teeters, *Electrochim. Acta* 48 (2003) 2137.
- [76] A. Jukic, M. M- Hukovic, *Electrochim. Acta* 48 (2003) 3929.
- [77] P. R. Roberge, R. Baudoin, *J. Appl. Electrochem.* 18 (1988)38.
- [78] M. Sluyters-Rehmbach, *Pure Appl. Chem.* 66 (1994)1831.
- [79] T. Pajkossy, *J. Electroanal. Chem.* 346 (1994) 111.
- [80] A. Tlili, M. A. Jarboui, A. Abdelghani, D. M. Fathallah, M. A. Maaref, *Mater. Sci. Eng. C25* (2005) 490.
- [81] C. A. Schiller, W. Strung, *Electrochim. Acta* 46 (2001) 3619.
- [82] F. Rosalbino, G. Borzone, E. Angelini, R. Raggio, *Electrochim. Acta* 48 (2003) 3939.
- [83] F. Köleli, T. Röpke, C. H. Hamann, *Electrochim. Acta* 48 (2003) 1596.
- [84] Allen J. Bard, Larry R. Faulkner, "Electrochemical Methods: Fundamental and application", Wiley & Sons, New York-Chichester- Brisbane-Toronto-Singapore, (1991) pp 5-13, 218.
- [85] Joseph Wang, "Analytical Electrochemistry" 2nd Ed, Wiley & Sons, United Stat (2004) pp 18-21.
- [86] A. E. Bohe, J. R. Vilche, K. Jüttner, W. j. Lorenz, W. Paatsch, *Electrochim. Acta* 30(10) (1989) 1443.
-

-
- [87] J. N. Chazalviel, *Electrochim Acta* 35 (10) (1990) 1545.
- [88] Gary Hodes, "Electrochemistry of nanomaterials" Wiley-VCH, Weinheim; New York Chichester- Brisbane-Singapore-Toronto (2001) pp 141-152.
- [89] TopoMetrix visualizing the micro world; TMX 2000 Discoverer Scanning Probe Microscope; User's Manual Version 3.05; 85-10086 Rev.C, pp 3.11 – 3.15
- [90] Chunli Bai, "Scanning Tunneling Microscopy and its application" Springer- verlag Berlin Heidelberg (1995) pp 50-75.
- [91] R. M. Metzger, V. V. Konovalov, S. Ming, X. Tao, Z. Giovanni, X. Bin, B. Mourad, W. D. Doyle, *IEEE Trans. Magn.* 36(1) (2000) 30.
- [92] K. Nielsch, F. Müller, A. P. Li, U. Gösele, *Adv. Mater.* 12 (2000) 582.
- [93] J. Liang, H. Chik, J. Xu, *IEEE J. Sel. Top. Quantum Electron.* 8(5) (2002) 998.
- [94] Mordechai Schlesinger, Milan Paunovic, "Modern electroplating" 4^{Ed}. Wiley & Sons, New York- Chichester- Weinheim- Brisbane- Singapore-Toronto, (2000) pp 13-17, 30.
- [95] C. A. Marozzi, A. C. Chialvo, *Electrochim. Acta* 45 (2001) 2111.
- [96] C. A. Marozzi, A. C. Chialvo, *Electrochim. Acta* 45 (2001) 861.
- [97] F. Huet, M. Musiani, R. P. Nogueira, *J. Solid State Electrochem.* 8 (2004) 786.
- [98] J. Xu, X. Huang, G. Xie, Y. Fang, D. Liu, *Mater. Res. Bull.* 39 (2004) 811.
- [99] L. Fedrizzi, F. J. Rodriguez, S. Rossi, F. Deflorian, R. Dimaggio, *Electrochim. Acta.* 46 (2001) 3715.
- [100] U. Casellato, S. Cattarin, M. Musiani, *Electrochim. Acta* 48 (2003) 3991.
- [101] J. M. Elliott, J. R. Owen, *Phys. Chem. Chem. Phys.* 2 (2000) 5653.
- [102] M. E. T. Molaes, V. Buschmann, D. Dobrev, R. Neuman, R. Scholz, I. U. Schuchert, J. Vetter, *Adv. Mater.* 13(1) (2001) 62.
- [103] G. B. Khomutov, V. V. Kislov, R. V. Gainutdinov, S. P. Gubin, A. Y. Obydenov, S. A. Pavlov, A. N. Cherenkov, E. S. Soldatov, A. L. Tolstikhina, A. S. Trifonov, *Surf. Sci.* 532-535 (2003) 287.
- [104] R. Kelsall, I. Hamley, M. Geoghegan, "Nanoscale science and technology" Wiley & Sons, England (2005) pp 150-158.
- [105] M.A. G. Soler, S. W. Dasilva, V. K. Garg, A. C. Oliveira, R. B. Azevedo, A. C. M. Pimenta, E. C. D. Lima, P. C. Morais, *Surf. Sci.* 575 (2005)12.
- [106] L. Guo, E. Leobandung, S. Y. Chou, *Science* 275 (1997) 649.
- [107] H. R. Khan, K. Petrikowski, *Mater. Sci. Eng. C19* (2002) 345.
- [108] David Van Der Beck, "Evidence of the hexagonal columnar liquid crystal phase of hard colloidal platelets by high resolution SAXS" Proefschrift universiteit Utrecht (2005) p22.
-

-
- [109] K. Saber, C. C. Koch, P. S. Fedkiw, *Mater Sci. Eng.* A341 (2003) 174.
- [110] A. N Zakhlevnykh, *J. Magn. Magn. Mater.* 269(2) (2004) 238.
- [111] C. Coutanceau, A. F. Rakotondrainibé, A. Lima, E. Garnier, S. pronier, J. M. Léger, C. Lamy, *J. Appl. Electrochem.* 34 (2004) 61.
- [112] G-Belmonte, J. Bisquert, *Electrochim. Acta* 47 (2002) 4263.
- [113] H. K. Song, Y. H. Lee, L. H. Dao, *Electrochim. Acta* 44 (1999) 3513.
- [114] S. Liu, *Solid State Ionics* 177 (2006) 53.
- [115] J. B. Bajat, M. D. Maksimovic, G. R. Radivic, *J. Serb. Chem. Soc.* 67 (8-9)(2002) 625.
- [116] S. K. Zečević, J. B. Zotović, S. L. GojkoVić, V. Radmilović, *J. Electroanal. Chem.* 448 (1998) 245.
- [117] E. Gileadi, E. Kirowa-Eisner, *Corros. Sci.* 47 (2005) 3068.
- [118] R. F. Sandenbergh, E. Van der Lingen, *Corros. Sci.* 47 (2005) 3300.
- [119] H. J. Flitt, P. Schweinsberg, *Corros. Sci.* 47 (2005) 3034.
- [120] J. R. Galvele, *Corros. Sci.* 47 (2005) 3053.
- [121] H. Hladky, J. L. Dawson “Corrosion monitoring using low frequency electrochemical noise”, Corrosion and protection center, University of Manchester, UK.
- [122] R. A. Cottis, M. A. A. Al-Awadhi, H. Al-Mazeedi, S. Turgoose, *Electrochim. Acta* 46 (2001) 3665.
- [123] J. M. Sanchez-Amaya, R. A. Cottis, F. J. Botana, *Corros. Sci.* 47 (2005) 3280.
- [124] U. Bertocci, C. Gabrielli, F. Huet, M. Keddam, P. Rousseau, *J. Electrochem. Soc.* 144(1) (1997) 37.
- [125] H. Y. Ma, C. Yang, S. H. Chen, Y. L. Jiao, S. X. Huang, D. G. Li, J. L. Luo, *Electrochim. Acta* 48 (2003) 4277.
- [126] A. W. Bott, *Curr. Sep.* 17:3 (1998) 87.
- [127] Z. Yun-Lian, L. Qi-ling, *J. Zhejiang Univ. Science A* 7(89) (2006) 1407.
- [128] M. G. S. Ferreira, M. D. C. Belo, N. E. Hakiki, G. Goodlet, M. F. Montenor, A. M. P. Simões, *J. Braz. Chem. Soc.* 13(4) (2002) 433.
- [129] K. Jüttner, *Electrochim. Acta* 35 (10) (1990) 1501.
- [130] A. S. Bondarenko, G. A. Ragoisha “Variable Mott-Schottky plots acquisition by potentiodynamic electrochemical impedance spectroscopy” presented at the 4th Baltic conference of electrochemistry, Greifswald 13-16 March 2005.
- [131] F. J. Martin, G. T. Cheek, W. E. O’Grady, P. M. Natishan, *Corros. Sci.* 47 (2005) 3187.
- [132] K. V. Rao, A. Smakula, *J. Appl. Phys.* 36(6) (1965) 2038.
- [133] M. Kamrunnahar, J. Bao, D. D. Macdonald, *Corros. Sci.* 47 (2005) 3111.
-

-
- [134] N. V. Myung, K. Nobe, *J. Electrochem. Soc.* 148(3) (2001) C136.
- [135] A. G. Prieto, M. L. Fdez-gubieda, *Physica B* 354 (2004) 92.
- [136] M. Bettge, J. Chatterjee, Y. Haik, *BioMagnetic Research and Technology* 2 (4) (2004) 1.
- [137] I. R. Torres, G. Valentin, F. Lapique, *J. Appl. Electrochem.* 29 (1999) 1035.
- [138] N. V. Myung, D. Y. Park, B. Y. Yoo, P. T. A. Sumodjo, *J. Magn. Mater.* 265 (2003) 189.
- [139] G. Barcelo, J. Garcia, M. Sarret, C. Müller, *J. Appl. Electrochem.* 24 (1994) 1249.
- [140] S. G. Song, Z. Ling, F. Placido, *Mater. Res. Bull.* 40 (2005) 1081.
- [141] H. S. Kim, J. H. Shin, S. I. Moon, S. P. Kim, *Electrochim. Acta* 48 (2003) 1573.
- [141a] Eugene A. Irene “Electronic materials science” Wiley Interscience (2005) p28.
- [142] V. A. Alves, A. M. C. Paquim, A. Cavaleiro, C. M. A. Brett, *Corros. Sci.* 47 (2005) 2871.
- [143] M. Stern, A.L. Geary, *J. Electrochem. Soc.* 104 (1) (1957) 56.
- [143a] M. Stern, *Corrosion* 14(9) (1958) 440t.
- [144] S. S. A. E. Rehim, H. H. Hassan, M. A. Amin, *Appl. Phys. Sci.* 187 (2002) 279.
- [145] A. K. Nigam, R. Balasubramaniam, S. Bhargava, R. G. Baligidad, *Corros. Sci.* 48 (2006) 1666.
- [146] D. J. Blackwood, *Electrochim. Acta* 46 (2000) 563.
- [147] G. A. Ragoisha, A. S. Bondarenko, *Surf. Sci.* 566-568 (2004) 315.
- [148] Zhong Shi and Meilin Liu in “Characterization of nanophase material” by Zhong Lin Wang, Wiley –VCH Verlag, Weinheim . New York . chichester . Brisbane . Singapore . Toronto (2000) p165.
- [149] A. J. Davenport, L. J. Oblonsky, M. P. Ryan, M. F. Toney, *J. Electrochem. Soc.* 147 (2000) 2162.
- [150] D. D. Macdonald, *Pure Appl. Chem.* 71 (1999) 951.
- [151] D. D. Macdonald, *J. Electrochem. Soc.* 139 (1992) 3434.

8 Appendix

8.1 X-ray diffraction of cobalt nanoparticles

Cobalt sample was examined by X-ray diffraction in reflexion mode with the cobalt k_{α} ($\lambda = 1.788 \text{ \AA}$) radiation. The result obtained at wide diffraction angles is showed on the following graph.

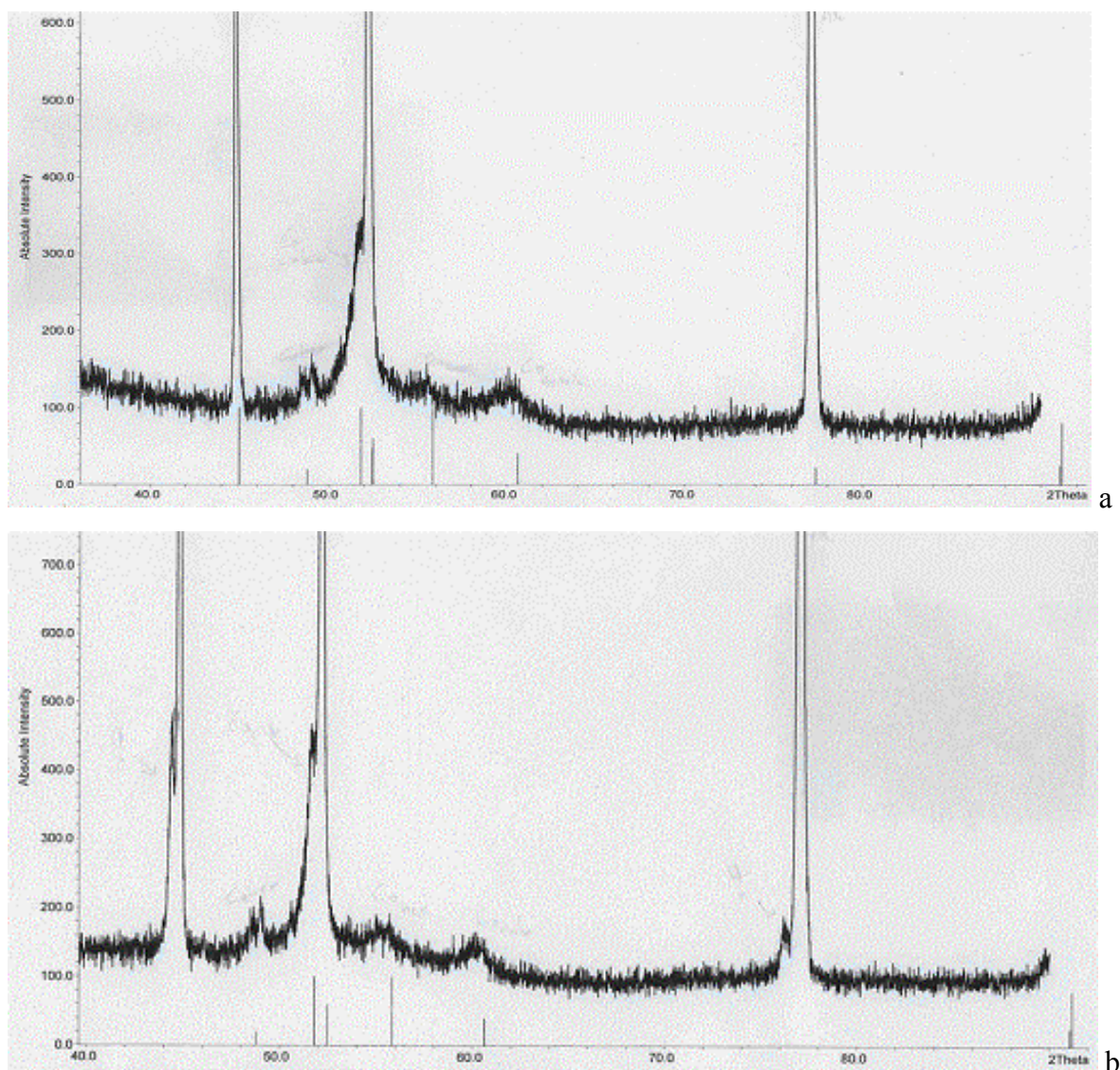


Fig. 8.1. XRD spectrum of cobalt nanoparticles deposited from aqueous solution (a) or in the presence of Brij 76 liquid crystal (b) within the pores of alumina membrane.

The spectrum exhibits interesting features, showing the main diffraction peaks at $2\theta \sim 44.9$, 52.4 and 77.4° characteristic of the aluminum substrate. Two other peaks appear at 48.8 and 55.85° characteristic of (100) and (101) diffraction plan of hexagonal centered (hcp) cobalt with

reticular distances 2.165 and 1.910Å respectively. Another signals centered around 52° and 61° are detected, thus including the presence of face- centered-cubic (fcc) cobalt particles with d_{111} and d_{200} of 2.047 and 1.77 Å respectively. Both hexagonal and cubic cobalt crystals are present in the pore of alumina membrane; the broadening of the XRD peaks is indicative of the nanoparticles.

8.2 Phase diagram of surfactant used in double template deposition.

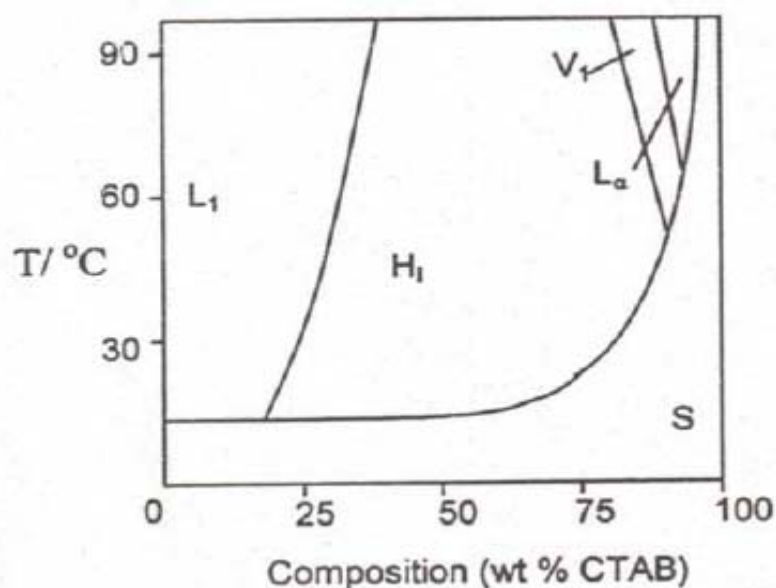


Fig. 8.2. Liquid crystal phase behavior of CTAB + water mixture. Copy from reference [38] page 19

The composition of the CTAB hexagonal mixture used in this investigation was chosen according to the giving phase diagram. A large hexagonal domain (H_1) dominates the phase diagram of CTAB mixture.

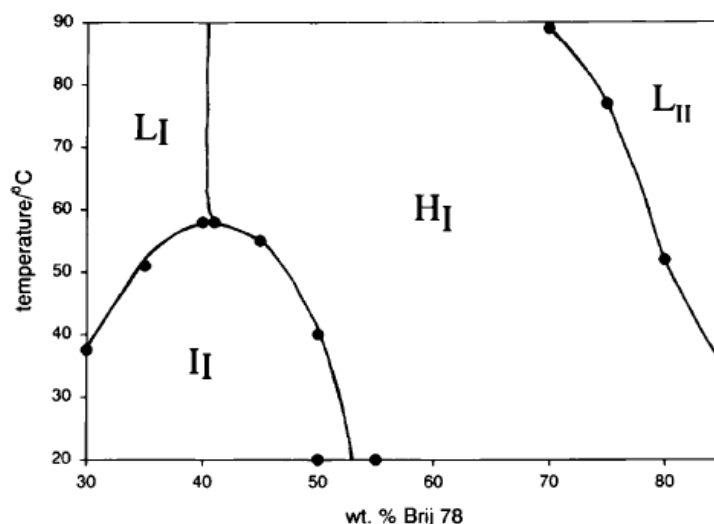


Fig. 8.3. Liquid crystalline phase diagram of Brij 78 / 0.2 M Nickel (II) acetate, 0.5M sodium acetate and 0.2 M boric acid templating system. Diagram copy from Ref [57].

The composition of the hexagonal phase of Brij 78 liquid crystal mixture used in this investigation was chosen according to the given phase diagram and checked with small angle x-ray scattering. The Brij 78 templating mixture is simpler in behavior and the hexagonal domain (H_I) is stable over a large temperature and composition range.

8.3 Working hypothesis for impedance measurement

The electrochemical impedance spectroscopy can provide useful information only when the investigation is performed correctly. For a successful experiment, some basic requirements are needed, among other we have:

- *The linearity*: the responses of the input sinusoidal voltage should be a sinusoidal current with the same frequency, different phase and amplitude. This is achieved experimentally if the amplitude of the sine wave perturbation signal is small enough to keep the selected state of the system unchanged.
- *Lack of convection and migration*: no changes in local concentration of electrolyte other than those caused by diffusion or charge transfer should occur.
- *Single input - single output*: this requirement could be achieved if the parameters such as temperature, concentration, and pH are kept constant.
- *Steady state*. The system being measured must be at a steady state throughout the time required to measure. In practice the cell can change through adsorption of solution impurities, growth of an oxide layer, coating degradation and temperature changes [69, 72].

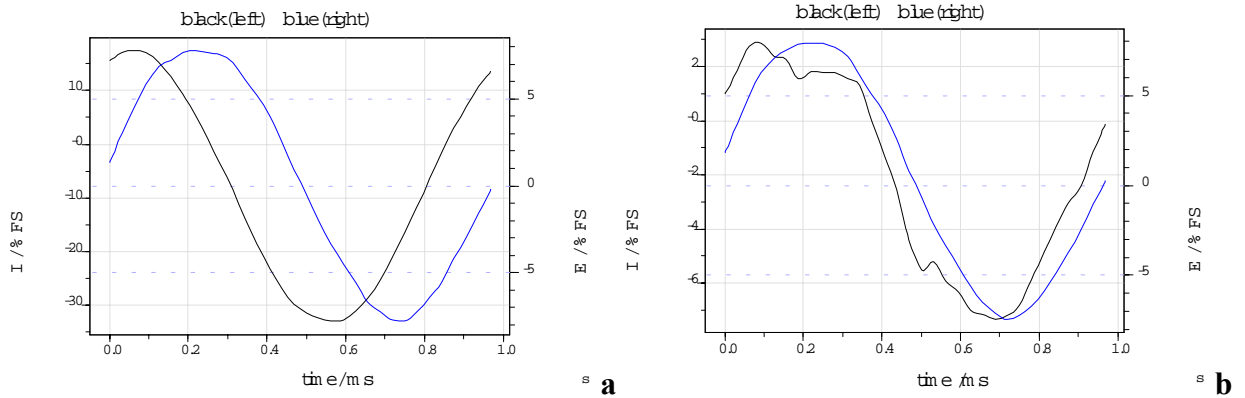


Fig. 8.4. Potential input and current output recorded during potentiodynamic EIS (for Mottschotky analysis). (a) good current response, (b) bad current response of the ac voltage.

The system (a) is linear because the current response of the voltage is also a sinusoidal function of the same frequency, different phase and amplitudes. On the contrary, the current response in (b) is not very good. The system (b) doesn't obey to all working hypothesis and the result obtained with such signal response should not be valid.

8.4 Fitting of impedance data and calculation of the $Z(j\omega)$ equations.

8.4.1 Impedance of alumina membrane.

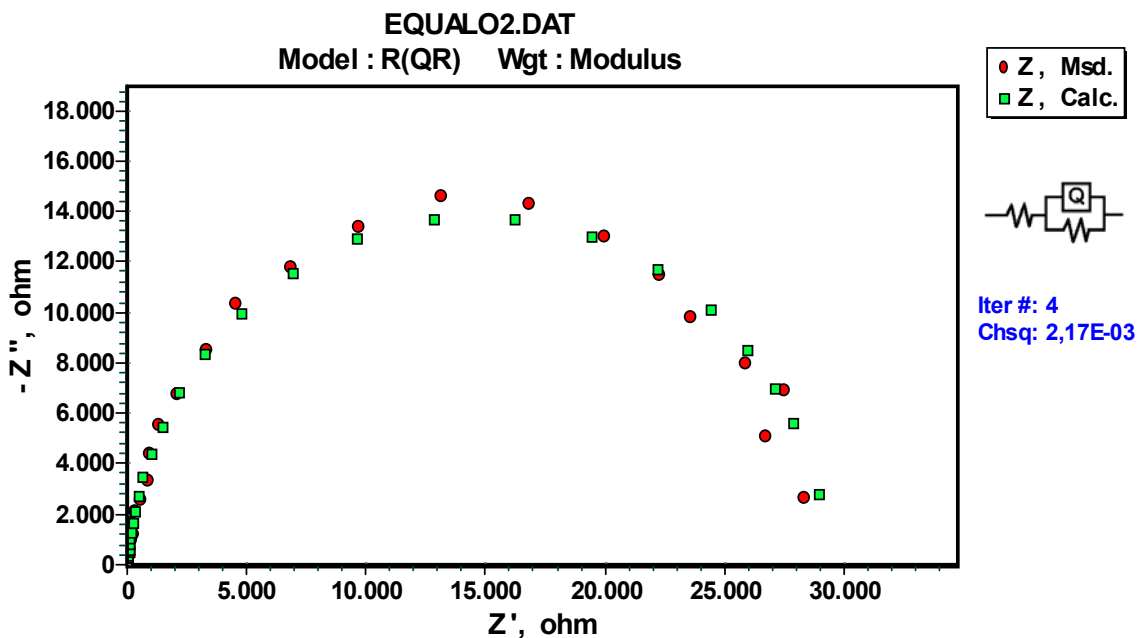


Fig. 8.5. Nyquist representation of impedance data of aluminum oxide anodized at 10°C fitted with the equivalent Circuit. “Msd” and “Calc” refer to measured and calculated data, respectively.

The real and imaginary part of impedance was calculated as function of the frequency of the sinusoidal voltage.

Recall (From Ref. [69], [71], [101] & [152])

[152]: Ş. Selçuk Bayin "Mathematical Methods in science and Engineering" John Wiley & Sons (2006) pp293-296.

DeMoivre theorem of complex number [152].

$$\left[r(\cos \theta + j \sin \theta) \right]^{\frac{p}{q}} = r^{\frac{p}{q}} \left[\cos \left(\frac{p}{q} \theta \right) + j \sin \left(\frac{p}{q} \theta \right) \right] \quad \text{That is the power of a complex number}$$

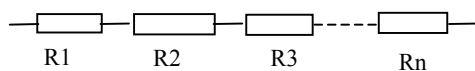
written in the trigonometric form; r is the module of the complex number and θ its argument.

$$\text{Therefore, } j^\alpha = \cos \alpha \frac{\pi}{2} + j \sin \alpha \frac{\pi}{2}, \quad j^{-\alpha} = \cos \alpha \frac{\pi}{2} - j \sin \alpha \frac{\pi}{2} \quad \text{and} \quad \sqrt{j} = j^{\frac{1}{2}} = \cos \frac{\pi}{4} + j \sin \frac{\pi}{4} = \frac{\sqrt{2}}{2} + j \frac{\sqrt{2}}{2}$$

Euler relations

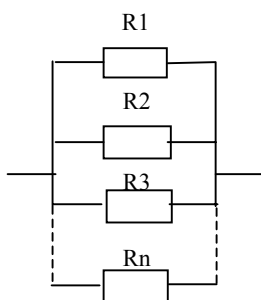
$$e^{j\theta} = \cos \theta + j \sin \theta \quad \text{and} \quad e^{-j\theta} = \cos \theta - j \sin \theta$$

-Association of resistors in series.



$$R_{eq} = R_1 + R_2 + \dots + R_n$$

-Association of resistor in parallel:



$$\frac{1}{R_{eq}} = \frac{1}{R_1} + \frac{1}{R_2} + \dots + \frac{1}{R_n}$$

Impedance of a capacitor:

$$Z_c = \frac{1}{j\omega C}$$

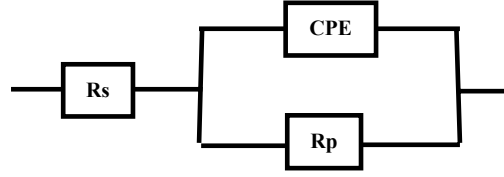
Impedance of a constant phase element (CPE or Q): $Z_Q = \frac{1}{A(j\omega)^\alpha}$

Warburg element (W):

$$Z_w = \frac{\sigma}{\sqrt{j\omega}}$$

For any angle θ , $\cos^2 \theta + \sin^2 \theta = 1$

These relations can be used to calculate the impedance expression of porous alumina



$$Z_Q = \frac{1}{A(j\omega)^\alpha} = \frac{1}{A\omega^\alpha} j^{-\alpha} = \frac{1}{A\omega^\alpha} \left(\cos \alpha \frac{\pi}{2} - j \sin \alpha \frac{\pi}{2} \right) \quad [101]$$

The calculation was done according to the following rule: when the elements are connected in series, their impedance are added to each other; while in the case of parallel connection, their admittances or the reciprocal of the impedances are added [69]. For clarity, the subscript Q was used in equations to refer for constant phase element instead of the symbol “CPE” shown in the model.

$Z(j\omega) = R_s + Z_1$ Where Z_1 is the equivalent impedance of the parallel part of the model.

$$\frac{1}{Z_1} = \frac{1}{R_p} + \frac{1}{Z_Q} = \frac{1}{R_p} + \frac{A\omega^\alpha}{\cos \alpha \frac{\pi}{2} - j \sin \alpha \frac{\pi}{2}} = \frac{\cos \alpha \frac{\pi}{2} - j \sin \alpha \frac{\pi}{2} + AR_p \omega^\alpha}{R_p (\cos \alpha \frac{\pi}{2} - j \sin \alpha \frac{\pi}{2})}$$

$$Z_1 = \frac{R_p (\cos \alpha \frac{\pi}{2} - j \sin \alpha \frac{\pi}{2})}{AR_p \omega^\alpha + \cos \alpha \frac{\pi}{2} - j \sin \alpha \frac{\pi}{2}}$$

It can be written in the form $Z_1 = a + jb$ by multiplying and dividing by the conjugated expression of the denominator.

$$Z_1 = \frac{R_p (\cos \alpha \frac{\pi}{2} - j \sin \alpha \frac{\pi}{2}) (AR_p \omega^\alpha + \cos \alpha \frac{\pi}{2} + j \sin \alpha \frac{\pi}{2})}{(AR_p \omega^\alpha + \cos \alpha \frac{\pi}{2} - j \sin \alpha \frac{\pi}{2}) (AR_p \omega^\alpha + \cos \alpha \frac{\pi}{2} + j \sin \alpha \frac{\pi}{2})}$$

After development and simplification using $\cos^2 \theta + \sin^2 \theta = 1$, we obtain

$$Z_1 = \frac{R_p + R_p^2 A \omega^\alpha (\cos \alpha \frac{\pi}{2} - j \sin \alpha \frac{\pi}{2})}{1 + R_p^2 A^2 \omega^{2\alpha} + 2R_p A \omega^\alpha \cos \alpha \frac{\pi}{2}} \quad \text{therefore} \quad Z(j\omega) = R_s + Z_1$$

$$Z(j\omega) = R_s + \frac{R_p + R_p^2 A \omega^\alpha (\cos\alpha \frac{\pi}{2} - j \sin\alpha \frac{\pi}{2})}{1 + R_p^2 A^2 \omega^{2\alpha} + 2R_p A \omega^\alpha \cos\alpha \frac{\pi}{2}} \quad (20)$$

The real and the imaginary parts of the impedance appear clearly on the mathematical expression.

8.4.2 Impedance of cobalt film deposited from aqueous solution into AAO.

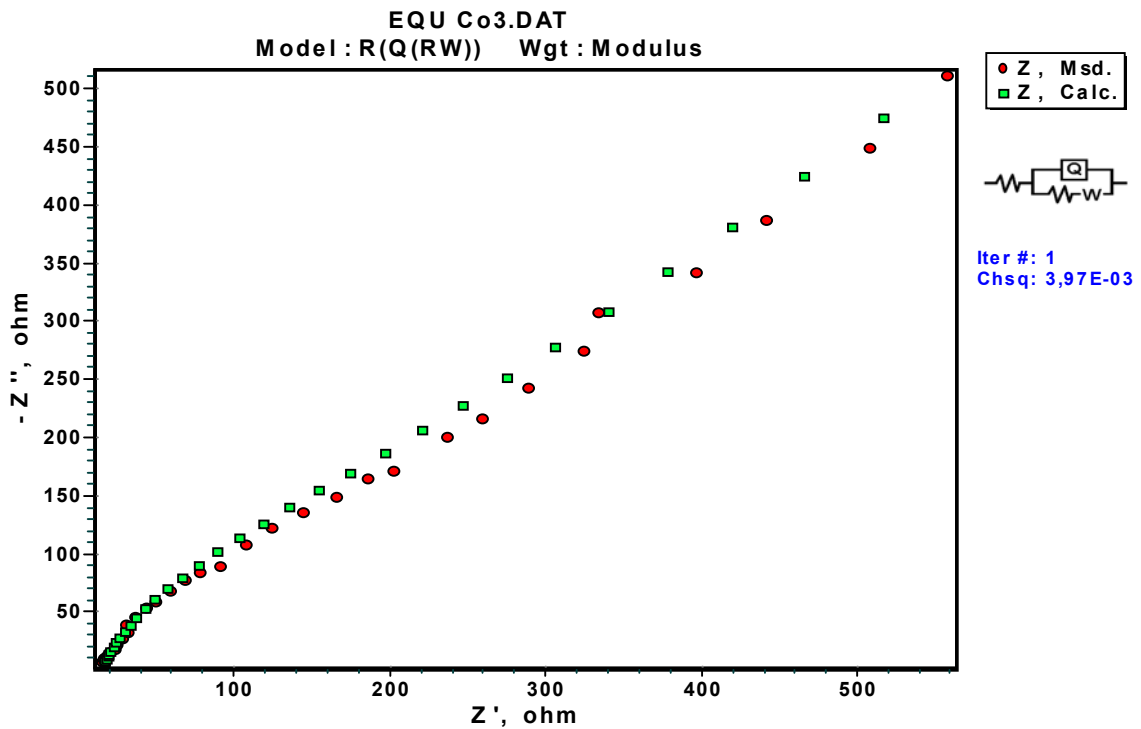
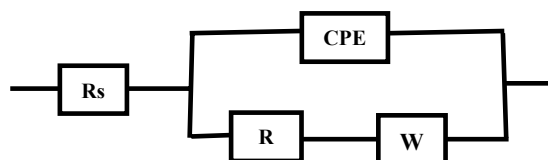


Fig. 8.6. Impedance data of Sample deposited from aqueous solution into AAO fitted with the equivalent electrical model. Msd and Calc refer to measured and calculated data respectively.

As shown by the figure, the equivalent model is in agreement with the experimental data. The same principle as in the cases of porous alumina was used to establish the mathematical expression of the impedance of this system as function of frequency.



R_s is in series with the second part of the model, therefore $Z(j\omega) = R_s + Z_1$ where

$$\frac{1}{Z_1} = \frac{1}{Z_Q} + \frac{1}{Z_2} \quad \text{and} \quad Z_2 = R_p + Z_w$$

- **Calculation of Z_2**

$$Z_2 = R_p + \frac{\sigma}{\sqrt{j\omega}} = R_p + \frac{\sigma}{\sqrt{\omega}} j^{-\frac{1}{2}} = R_p + \frac{\sigma}{\sqrt{\omega}} \left(\cos \frac{\pi}{4} - j \sin \frac{\pi}{4} \right) = R_p + \frac{\sigma}{\sqrt{\omega}} e^{-j\frac{\pi}{4}}$$

- **Calculation of Z_1**

$$\frac{1}{Z_1} = \frac{1}{\frac{1}{A(j\omega)^\alpha}} + \frac{1}{R_p + \frac{\sigma}{\sqrt{\omega}} e^{-j\frac{\pi}{4}}} = A\omega^\alpha (\cos \alpha \frac{\pi}{2} + j \sin \alpha \frac{\pi}{2}) + \frac{1}{R_p + \frac{\sigma}{\sqrt{\omega}} e^{-j\frac{\pi}{4}}} = A\omega^\alpha e^{j\alpha \frac{\pi}{2}} + \frac{1}{R_p + \frac{\sigma}{\sqrt{\omega}} e^{-j\frac{\pi}{4}}}$$

After reduction to the same denominator and rearrangement, we obtain

$$Z_1 = \frac{R_p \sqrt{\omega} + \sigma e^{-j\frac{\pi}{4}}}{A\omega^\alpha e^{j\alpha \frac{\pi}{2}} \left(R_p \sqrt{\omega} + \sigma e^{-j\frac{\pi}{4}} \right) + \sqrt{\omega}}$$

The total impedance expression can be written by replacing Z_1 in $Z(j\omega) = R_s + Z_1$

$$Z(j\omega) = R_s + \frac{R_p \sqrt{\omega} + \sigma e^{-j\frac{\pi}{4}}}{A\omega^\alpha e^{j\alpha \frac{\pi}{2}} \left(R_p \sqrt{\omega} + \sigma e^{-j\frac{\pi}{4}} \right) + \sqrt{\omega}} \quad (22)$$

Because of the complexity of the mathematical expression, $Z(j\omega)$ was not decomposed into real and imaginary part.

8.4.3 Impedance of cobalt film deposited from Brij 76 liquid crystal into AAO

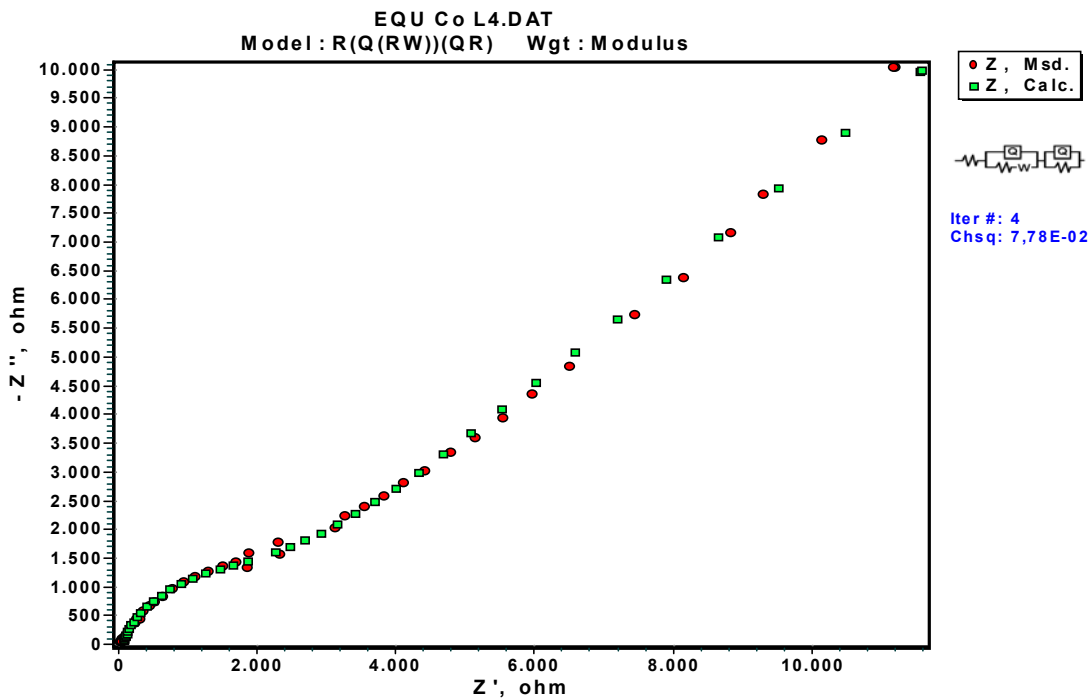
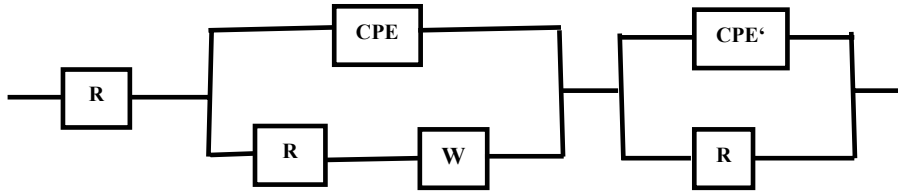


Fig. 8.7. Impedance of cobalt deposited from Brij 76 fitted with the equivalent model.

The experimental (measured Msd) and calculated (calc) data are in agreement. In this last case the electrical model is as follow.



We should remark that the first part of the model is similar to that of the sample deposited from aqueous solution.

$$Z(j\omega) = R_s + Z_1 + Z_3$$

Z_1 has the same expression as in the last case, only Z_3 will be calculated.

- Calculation of Z_3

$$\frac{1}{Z_3} = \frac{1}{R} + \frac{1}{Z_Q'} = \frac{1}{R} + A'(j\omega)^{\alpha'} = \frac{1}{R} + A'\omega^{\alpha'} e^{j\alpha'\frac{\pi}{2}} = \frac{1 + A'R\omega^{\alpha'} e^{j\alpha'\frac{\pi}{2}}}{R}$$

from there

$$Z_3 = \frac{R}{1 + A'R\omega^{\alpha'} e^{j\alpha'\frac{\pi}{2}}}$$

The total impedance expression can be written as follow:

$$Z(j\omega) = R_s + \frac{R_p \sqrt{\omega} + \sigma e^{-j\frac{\pi}{4}}}{A\omega^{\alpha} e^{j\alpha\frac{\pi}{2}} \left(R_p \sqrt{\omega} + \sigma e^{-j\frac{\pi}{4}} \right) + \sqrt{\omega}} + \frac{R}{1 + A'R\omega^{\alpha'} e^{j\alpha'\frac{\pi}{2}}} \quad (23)$$

8.4.4. Impedance model of alloys nanoparticles.

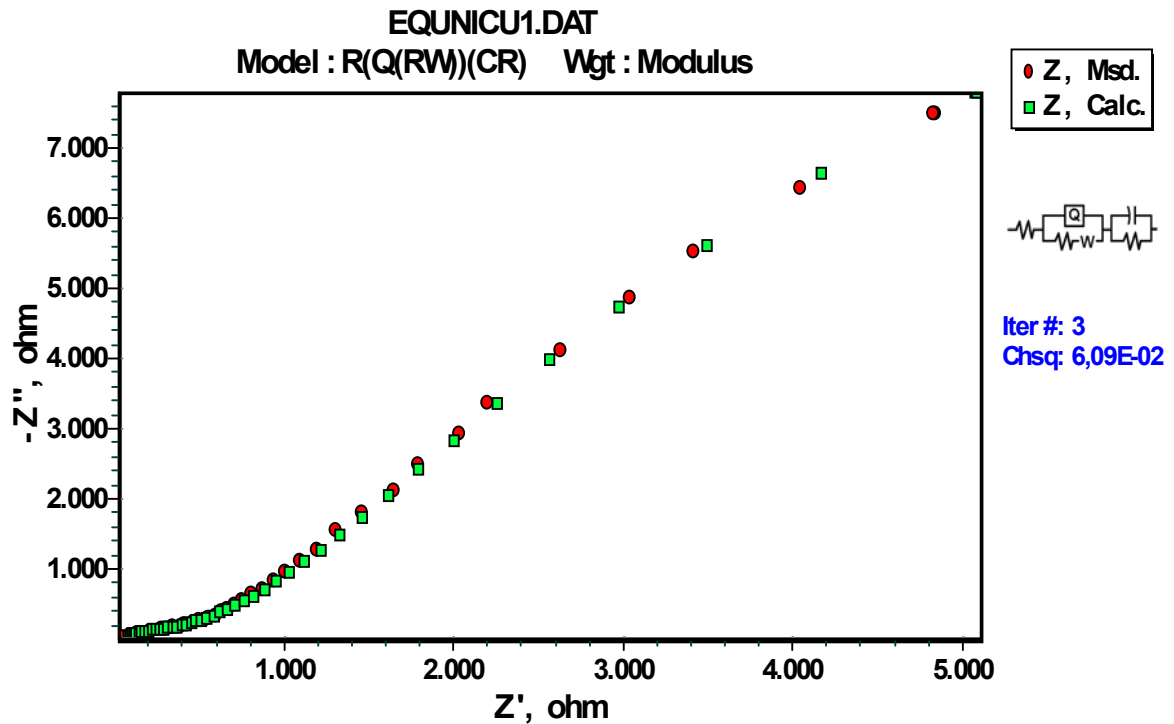
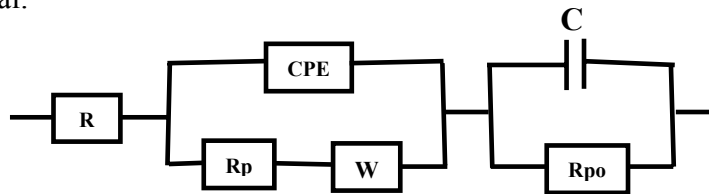


Fig. 8.8. Impedance of NiCu alloy nanofilm deposited from liquid crystal. Msd and Calc refer to experimental and calculated data respectively. The electrical model is in good agreement with the experimental.



The first part of the model is similar to that of sample deposited from aqueous solution into AAO. The total impedance of this model can be written as:

$$Z(j\omega) = R_s + Z_1 + Z_4$$

where Z_1 is the same as in the last case, only Z_4 will be calculated.

-Calculation of Z_4

$$\frac{1}{Z_4} = \frac{1}{\frac{1}{j\omega C}} + \frac{1}{R_{po}} = jC\omega + \frac{1}{R_{po}} = \frac{1 + jC\omega R_{po}}{R_{po}}$$

From this expression we obtain

$$Z_4 = \frac{R_{po}}{1 + jC\omega R_{po}}$$

The general impedance equation can be written as function of frequency as follow.

$$Z(j\omega) = R_s + \frac{R_p \sqrt{\omega} + \sigma e^{-j\frac{\pi}{4}}}{A\omega^\alpha e^{j\alpha\frac{\pi}{2}} \left(R_p \sqrt{\omega} + \sigma e^{-j\frac{\pi}{4}} \right) + \sqrt{\omega}} + \frac{R_{po}}{1 + jC\omega R_{po}} \quad (28)$$

More information's about the calculation of model impedance as well as examples of calculated models can be found in references [69] and [71].

8.5. Principle of the Atomic Force Microscopy (AFM)

In AFM, the force between the tip and the sample surface cause the cantilever to bend or deflect. Several forces contributed to the deflection of the AFM cantilevers, but the most common force associated with AFM is the inter-atomic force called the Van der Waals force.

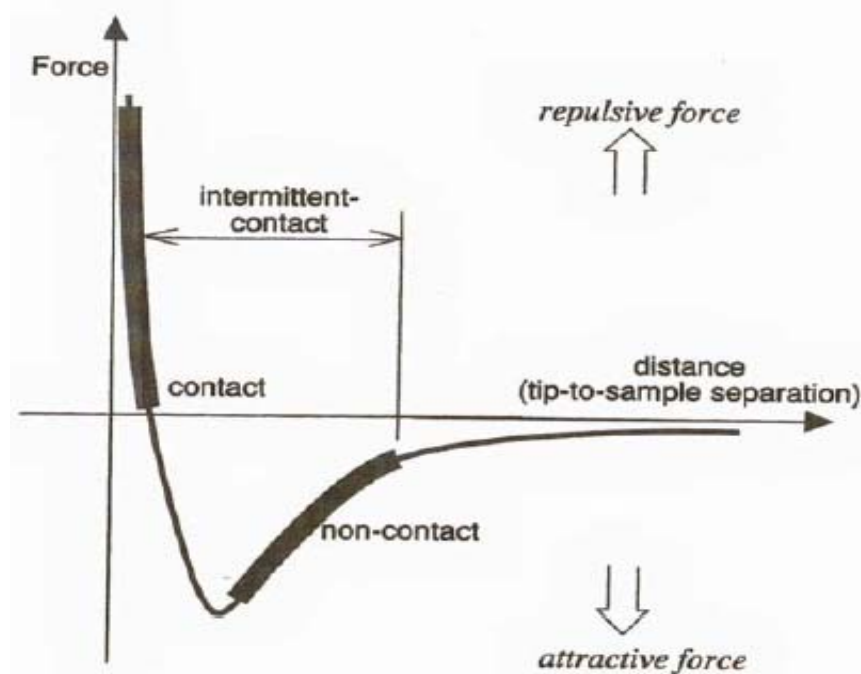


Fig. 8.9. Interatomic force vs distance curve, scanned from reference [65].

Fig. 8.9 shows the dependence of the Van der Waals force on the distance between tip and the sample. In the contact regime, the cantilever is held very close to the sample, and the inter-atomic force between the cantilever and the sample is repulsive. In the non-contact regime, the cantilever is held on the order of tens to hundreds of angstroms from the samples surface and the inter-atomic force between the cantilever and the sample is attractive.

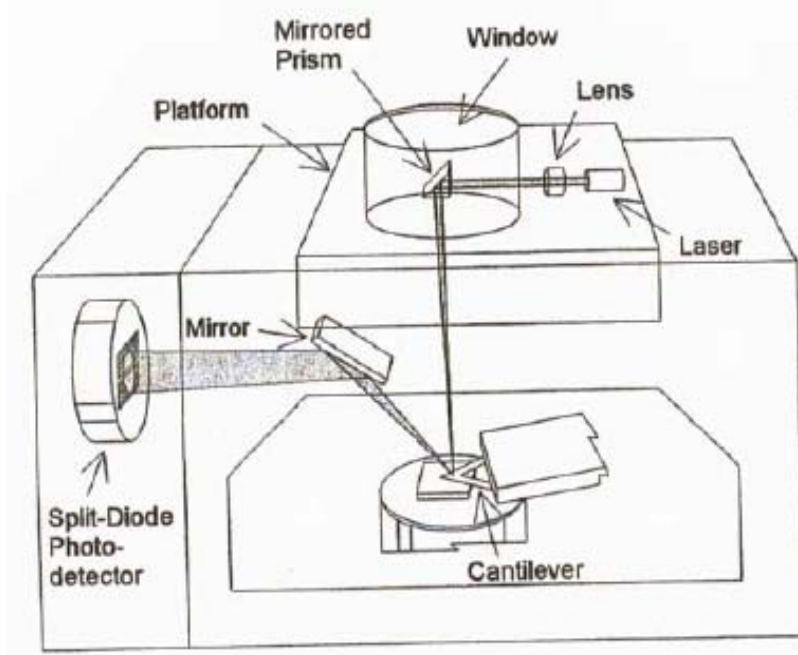


Fig. 8.10. AFM optical block incorporating the optical deflection system. Copy from the book: *Sergei N. Magonov, Myung-Hwan whangbo, "Surface analysis with STM and AFM" VCH verlagsgesellschaft mbH, Weinheim (1996) p32.*

In most common AFM instrument, a laser beam bounces off the back of the cantilever onto a position-sensitive photo detector (PSPD). As the cantilever bends, the position of the laser beam on the detector shifts. The PSPD can measure displacements of light as small as 10 \AA . The measured cantilever deflections allow the computer to generate the map of the surface topography.

Acknowledgements

This dissertation is the result of three years of work during which I was supported by many people. For this reason I want to take this opportunity to express my gratitude to all of them.

I would like to thank my supervisor Prof. Dr. Wieland Schäfer, for giving me the opportunity to work in his group; for support, encouragement, interesting suggestions and discussions. During these years I have known him as a sympathetic person.

I wish to express my gratitude to Dr. Anton Hauser for his continuous assistance, suggestions and advises during AFM and STM measurements. He is also the one who introduced me to these surface techniques.

Special thanks go to Dr Nicola Pinna for discussion about the images; particularly the used of Fast Fourier transformed and Power spectra density function to determine the repeat distance on the structure.

My sincere thank to Dr. K. Tittes for the calibration of the Lock-In Amplifer used for impedance measurements.

I'm thankful to Dr G. Foerster for the x-ray characterization of Brij 78 and Brij76 liquid crystal plating mixtures.

I would like to acknowledge Dr. M. Fotsing Kamte for introduction in the laboratory, his permanent suggestions and advises.

I like to express my gratitude to Dr. T. Schelenz and Ms. B. Martin for their collaborations and the friendship atmosphere in the group.

I want to extend my appreciation to other colleagues of the DFG program.

The Deutsche Forschungsgemeinschaft and the Land Sachsen-Anhalt are acknowledged for the financial support

Finally I take this opportunity to express my gratitude to my parents for their moral support during this time.

Publications and conferences

- 1- A. Foyet, A. Hauser, W. Schäfer, Electrochemical deposition of cobalt nanoparticles by double templates and pulse current methods. *Mater. Sci. Eng. C* 27 (2007) 100.
- 2- Adolphe Foyet, Anton Hauser, Wieland Schäfer, Template electrochemical deposition and characterization of Zn-Ni alloy nanomaterial *J. Electroanal. Chem.* 604(2007)137.
- 3- Adolphe Foyet, Anton Hauser, Wieland Schäfer, Double template electrochemical deposition of NiCo and NiCu alloys nanoparticles and nanofilms *J. Solid State Electrochem.* (2007) **In press.**
- 4- A. Foyet, A. Hauser, W. Schäfer, Graduate College of Chemistry annual workshop 15-18 February 2005, Korhen-Sahlis / Germany, “*Highly ordered Cobalt nanostructures obtained by electrodeposition*” **Oral presentation**
- 5- A. Foyet, A. Hauser, M. F. Kamte, W. Schäfer, Annual Meeting of the German Society of Chemistry (GDCh) 11-14 September 2005, Düsseldorf / Germany, “*Electrochemical deposition of cobalt nanoparticles*”, **Poster presentation**
 - **3th GDCh poster price award in 2005.**
- 6- A. Foyet, A. Hauser, W. Schäfer, Graduate College of Chemistry annual workshop, 21-24 February 2006, Freyburg / Germany, “*Nanoscale deposition of metal by double template electroreduction*” **Oral presentation**
- 7- A. Foyet, A. Hauser, W. Schäfer, Young Chemist Symposium 15-18 March 2006, Konstanz / Germany, “*From one template to double template electrochemical deposition of cobalt nanoparticles*” **Oral presentation**

- 8-** A. Foyet, A. Hauser, W. Schäfer, 57th annual meeting of the International Society of Electrochemistry, 27/08 - 01/09 /2006, Edinburgh / United kingdom, “*Template electrochemical deposition and characterization of Zn-Ni alloy nanoparticles*” **Poster presentation**
- 9-** A. Foyet, A. Hauser, W. Schäfer, Triple Graduate College Symposium 08-10 October 2006, Freyburg / Germany. “*Double template electrochemical deposition of Zn-Ni alloy nanoparticles*” **Poster presentation.**
- 10-** A. Foyet, A. Hauser, W. Schäfer , 35th Topical meeting on liquid crystals 21-23 March 2007, Bayreuth / Germany “*Lyotropic liquid crystal as template for electrochemical deposition of ZnNi, NiCo and NiCu alloys nanoparticles*” **Oral Presentation.**
- 11-** A. Foyet, A. Hauser, W. Schäfer, “*Double template electrochemical deposition and characterization of ordered metallic and alloy nanomaterials*“ 1 May 2007, Technical University of Eindhoven / Netherlands; **Invited speaker, Oral presentation**

Curriculum vitae

First name	Adolphe
Family name	Foyet
Date of birth	11 February 1977
Place of birth	Fotouni (Cameroon)

Education

04/09/2004 till now	- PhD student at the Martin-Luther-Universität Halle-Wittenberg. Institute of Physical Chemistry / Lab. of Applied Electrochemistry Supervisor: Prof. Dr. Wieland Schäfer
2002- 2003	-Master of science / Chemistry, University of Yaoundé I (Cameroon) Supervisor: Prof. Emmanuel Ngameni
2000-2002	-Postgraduate diploma in chemistry, University of Dschang
1997-2000	-Bachelor degree in chemistry, University of Dschang (Cameroon)
1990-1997	- Secondary school in Bandja, Scientific “General Certificate of Education” advanced level (GCE’AL) & ordinary level (GCE’ OL).
1983-1990	Primary school in Fotouni (Cameroun)

Professional skill

2001-2003	- Higher Teacher Training College of the University of Yaoundé I A two years training program followed together with the master study. “ <i>Secondary and high school teacher diploma in chemistry</i> ”.
2002- 08/2004	- <i>Electrocoagulation / flocculation</i> methods for waste water treatment.
09/2004- 2007	- <i>Surface science techniques</i> : Atomic force Microscope (AFM) and scanning tunneling microscope (STM) - <i>Electrochemical techniques</i> : Electrochemical impedance spectroscopy; simulation; experimental data analysis and determination of equivalent circuit. Mott-Schottky analysis of semiconductor electrode; Polarizations techniques; Surface preparation and electrodeposition of nanomaterial.

Erklärung

Die vorliegende Arbeit habe ich selbständig und ohne fremde Hilfe verfasst. Ich habe keine anderen als die von mir angegebene Quellen und Hilfsmittel benutzt. Die den benutzten Werken wörtlich oder inhaltlich entnommenen Stellen habe ich als solche kenntlich gemacht.

Halle, 26 Juni 2007

A. FOYET